UNIVERSITY OF SOUTHAMPTON

LARGE EDDY SIMULATION OF FORCES AND WAKE MODES OF AN OSCILLATING CYLINDER

by

Sunghan Kim

A thesis submitted in partial fulfilment for the
degree of Doctor of Philosophy

Fluid Structure Interactions Research Group
Faculty of Engineering and the Environment

October 2014

Declaration of Authorship

I, Sunghan Kim, declare that this thesis, titled 'LARGE EDDY SIMULATION OF FORCES AND WAKE MODES OF AN OSCILLATING CYLINDER', and the work presented in it are my own. I confirm that this thesis is the result of work done by the candidate whilst studying at the University of Southampton. All published work has been referenced and sources of help acknowledged. I understand that my thesis may be made electronically available to the public.

The following aspects of this work have been presented at an international conference and published by or submitted to peer review journals:

- **Large eddy simulation of flow past a stationary and controlled oscillating circular cylinder**, Sunghan Kim, Philip A. Wilson, Zhi-Min Chen, 32nd Conference on Ocean, Offshore and Arctic Engineering, *OMAE 2013*, Nantes, France.
- **Numerical simulation of force and wake mode of an oscillating cylinder**, Sunghan Kim, Philip A. Wilson, Zhi-Min Chen, *Journal of Fluids and Structures* 44 (2014), 216-225.
- **Controlled vibrations of a submerged cylinder**, Sunghan Kim, Philip A. Wilson, Zhi-Min Chen, *Journal of Fluids and Structures* (Submitted).
- **Large-eddy simulation of the turbulent near-wake behind a circular cylinder: Reynolds number effects**, Sunghan Kim, Philip A. Wilson, Zhi-Min Chen, *Applied Ocean Research* (Submitted).
- **Effect of turbulence modelling on 3-D LES of transitional flow behind a circular cylinder**, Sunghan Kim, Philip A. Wilson, Zhi-Min Chen, *Ocean Engineering* (Submitted).

Acknowledgements

Thesis Supervisors, Prof. Philip Alan Wilson and Dr. Zhi-Min Chen.....

Abstract

The aim of this research is to examine the transition process between two different wake states of an oscillating circular cylinder in the frame of three-dimensional large-eddy simulation (LES). The relationship between the hydrodynamic force and near-wake structure of the fully-submerged cylinder is considered in detail, and results will be used to understand the mechanisms of vortex-induced vibration at high Reynolds flows. The simulations are performed on parallel processing in the University's high performance computing facility. The spanwise- and phase-averaging tools are developed in open source code OpenFOAM environment for qualitative comparisons with the experimental visualisation studies.

Verification and validation of the simulations at subcritical Reynolds numbers of 5500-41300 are conducted. The grid resolution and subgrid model, which highly influence on LES solutions, are carefully and properly chosen at the considered Reynolds numbers, and the resulting hydrodynamic forces and pressure are successfully predicted compared to the available experimental or direct numerical simulation data. In these studies, the variations of the near-wake structure and shear-layer frequency are examined with increasing Reynolds number. The numerical results exhibit the characteristic broadband spectral peaks of shear-layer frequency due to small-scale shear-layer vortices inside the freely-separating thin-boundary layers behind the cylinder, and clearly show the dependence of $\mathrm{Re}^{0.67}$ for which the shear-layer instability is fully developing in subcritical flow regime.

Based on the careful validations, turbulent flow behind an oscillating cylinder is investigated with various excitation amplitudes and a series of excitation frequencies. In these studies, the well-known flow features of an oscillating cylinder are reproduced and compared to the experimental observations. Two types of transition processes near flow resonance, namely the self-excited and reverse self-excited transitions, are captured first in a set of numerical simulations. Whilst the self-excited transition was only observed in the recent experiment especially at a certain flow condition, high amplitude excitation and lower Reynolds number, the present research shows numerical evidence that the one-time transition is possible even at lower excitation amplitude and higher Reynolds number as well. The change of the ensemble averaged wake patterns during the transition process strongly supports this numerical observation.

Contents

List of Figures

List of Tables

Nomenclature

Roman Symbols

Symbol	Description	Units
A	Excitation amplitude of forced oscillation	m
$\bar{C}_D$	Averaged drag coefficient	-
C_k	The model coefficient for the one-equation SGS model	-
C'_L	Root mean square of lift coefficient	-
C_p	Pressure coefficient	-
C_s	The model coefficient for the Smagorinsky SGS model	-
C_ϵ	The model coefficient for the one-equation SGS model	-
D	Diameter of cylinder	m
f_e	Excitation frequency of forced oscillation	s^{-1}
f_K	Vortex shedding or natural Kármán frequency	s^{-1}
f_{SL}	Frequency of shear-layer vortices	s^{-1}
k_t	Turbulent kinetic energy	m^2/s^2
L_z	Length of cylinder in axis direction	m
p	Pressure	N/m^2
Re	Reynolds number	-
Re_{crit}	Critical Reynolds number for shear-layer instability	-
S_{ij}	Rate of strain tensor	s^{-1}
St	Strouhal number	-
U	Free stream velocity	m/s
u_i	Velocity component in the i direction	m/s
$\overline{u}_i$	Mean velocity component in the i direction	m/s
u'_i	Velocity fluctuation component in the i direction	m/s
V	Volume	m^3

y	Cylinder displacement	m
y^+	Non-dimensional wall distance	-

Greek Symbols

Symbol	Description	Units
Δ	Grid filter size	m
Δt	Time step size	s
ν	Kinematic viscosity	m^2/s
ρ	Fluid density	kg/m^3
τ_{ij}^s	Component of subgrid scale stress tensor	kg/ms^2
ω_i	Vorticity component in the i direction	s^{-1}

Abbreviations

Symbol	Description
BD	Backward Difference
CD	Central Difference
CFD	Computational Fluid Dynamics
CFL	Courant-Friedrichs-Lewy number
CV	Control Volume
DNS	Direct Numerical Simulation
FEM	Finite Element Method
FDM	Finite Difference Method
FVM	Finite Volume Method
KH	Kelvin-Helmholtz
LES	Large Eddy Simulation
PISO	Pressure Implicit with Splitting of Operator
PIV	Particle Image Velocimetry
RANS	Reynolds Averaged Navier-Stokes
SGS	Subgrid Scale
TVD	Total Variational Diminishing
VIV	Vortex-Induced Vibration

Chapter 1

LITERATURE REVIEW AND PRELIMINARY DISCUSSION

The flow-induced vibration of a body in a free stream or vortex-induced vibration (VIV) is an important factor in structural engineering and design. Fluctuating forcing caused by the periodic shedding of vortex structures can excite the natural structural frequency of the body, causing the body to oscillate, usually transversely to the flow. This type of flow has a number of important applications, including VIV of offshore platforms, as well as deep-sea risers and sub-sea pipelines on the seafloor in the oil and gas industries.

The bluff-body or non-streamlined wake behind a stationary circular cylinder has been extensively studied in recent decades, and the wake structures and their vorticity dynamics have been relatively well understood. The wake of a stationary cylinder in a free stream is naturally unstable, resulting in the formation of the well-known Kármán vortex street behind the cylinder.

The interaction between a vibrating circular cylinder and the wake structure, however, arises from more complex flow features and a comparatively small amount is known about the nature of the fluid structure interaction. Oscillating amplitudes of the cylinder at a range of frequencies close to the frequency of formation of Kármán vortices can cause significant changes in both the wake structure and the hydrodynamic forces on the cylinder. To the best of the author's knowledge, most of numerical simulations dealing with the physical phenomena of an oscillating cylinder flow are very rare in literatures (mainly in experiment), and a few of simulations have been conducted at laminar flow

regime or lower Reynolds numbers. Therefore, this class of fluid-structure interaction remains the subject of ongoing research.

1.1 Scope of Thesis

1.1.1 Aim

The aim of the thesis is to examine the transition process between two distinct different wake states of an oscillating circular cylinder at subcritical Reynolds numbers of 5500-41300 in the frame of three-dimensional large-eddy simulation. Based on careful validations, the flow features of an oscillating cylinder on either side of transition and the nature of transition between two wake modes are numerically investigated in detail.

1.1.2 Objectives

To achieve the aim of the present research, several objectives have to be fulfilled:

- The development and assessment of three-dimensional large-eddy simulation technique for the high Reynolds flows in order to obtain close numerical approximations compared to the experimental measurements.
- The development and assessment of post-processing methods for comparisons with the time-, spanwise- or phase-averaged experimental visualisation studies.
- The complete validations of three-dimensional numerical simulations of turbulent flows past a stationary and oscillating cylinder at the considered Reynolds numbers. To this end, a detailed comparison with the experimental data is performed.

1.1.3 Thesis outline

The present thesis has been organised into six Chapters. The rest of this Chapter will present the literature reviews and the contents of each of the following Chapters are briefly summarised below:

In Chapter 2 the numerical approaches such as LES governing equations and the turbulence or subgrid scale modelling techniques used for all simulations are presented. The moving grid test, of course, is conducted in this Chapter.

Chapter 3 is devoted to the description of the grid-independent or -refinement study with the considered Reynolds numbers for a complete validation of the LES simulation technique. Based on the grid-refinement study, the main wake parameters obtained with various subgrid models such as hydrodynamic forces and pressure are validated with both experimental data and numerical results obtained with RANS and DNS at corresponding Reynolds numbers.

Chapter 4 describes the effect of the Reynolds number on a stationary cylinder. The time- and spanwise-averaged flow statistics are graphically compared to experimental observation and the variation of shear-layer frequency with the Reynolds number is discussed in detail.

Chapter 5 presents the numerical results of an oscillating cylinder flow. Further validation especially on lift force in a moving frame is additionally conducted at Re=10000 and compared with experimental measurements. Then, the lift behaviours at a series of excitation frequencies are carefully addressed and the resulting wake modes are both spanwise- and phase-averaged to obtain close approximation with experimental visual study. The self-excited and reverse transition between two different wake modes are discussed in detail in terms of hydrodynamic lift properties.

Finally, Chapter 6 draw conclusions from the present numerical investigation and extends the discussion to possible future study to be conducted on the subject.

1.2 Stationary Cylinder

The practical simple geometry of a circular cylinder is one of the most commonly used structural members in offshore engineering such as flare-towers on the topside of offshore platforms and the symmetrical nature of the circular section is independent of the flow direction, meaning no angle of attack occurred in contrast to other sections such as airfoils. Therefore, the study of fluid flow around a circular cylinder is of obvious practical importance.

The flow behind the simple geometry, however, exhibits extremely complex flow behaviours which are dependent on the Reynolds number, e.g. 3-D instability of wake, freely separating shear layers, small-scale vortices in the thin boundary layers, shear-layer instability and large-scale vortex shedding motion in the wake. Even though this research is primarily focused on an oscillating circular cylinder, the mechanism or instability causing vortex shedding in a fixed cylinder is significantly relevant to the wake of an oscillating cylinder.

1.2.1 Wake regimes

The study of the flow around a stationary cylinder has been the centre of many investigations and it is now common knowledge that the flow around the circular cylinder can be characterised essentially by two parameters, namely the Reynolds number Re=UD/ν and the Strouhal number St=$f_K D/U$, where U is the upstream or free-stream velocity, D the cylinder diameter, ν the kinematic viscosity of the flow and f_K the frequency of the shedding of vortices or the Kármán frequency. The first definition of the flow regimes around a circular cylinder was given by Roshko [12] and reviewed by a number of authors including Zdravkovich [11]. Although the various flow regimes and in particular the transition between the regimes are also affected by the level of free-stream turbulence, surface roughness, cylinder aspect ratio, end conditions and blockage ratio, the regimes of the wakes are adequately described by their dependence on the Reynolds number in general.

As outlined in Table 1.1 Zdravkovich [11] used the general location of the transition to turbulent flow for describing the wake state of a cylinder. The flow states are split into each regime that describes the wake in more detail, wake transition (TrW), shear layer transition (TrSL) and boundary layer transition (TrBL).

Within the laminar flow state, the wake remains attached around the entire surface of the cylinder (L1) and then the flow separates from the upper and lower surfaces of the cylinder, forming a steady, symmetric and closed near wake (L2). The wake becomes progressively longer with increasing Reynolds number, and the downstream wake becomes unsteady (L3). The vortex shedding is initiated by growth of the two-dimensional (2-D) Kármán instability, in which the vortices are shed alternately from

TABLE 1.1: Classification of flow regimes, suggested by Zdravkovich [11].

State	Regime	Reynolds number
Laminar	L1: No Separation L2: Closed Wake L3: Periodic Wake	0 to 4-5 4-5 to 30-48 30-48 to 180-200
Transition in Wake	TrW1: Far Wake TrW2: Near Wake	180-200 to 220-260 220-260 to 350-400
Transition in Shear Layers	TrSL1: Lower TrSL2: Intermediate TrSL3: Upper	350-400 to 1K-2K 1K-2K to 20K-40K 20K-40K to 100K-200K
Transition in Boundary Layers	TrBL0: Pre-critical TrBL1: Single Bubble TrBL2: Two Bubble TrBL3: Super-critical TrBL4: Post-critical	100K-200K to 300K-340K 300K-340K to 380K-400K 380K-400K to 500K-1M 500k-1M to 3.5M-6M 3.5M-6M to a certain point
Fully Turbulent	T1: Invariable T2: Ultimate	upto ∞

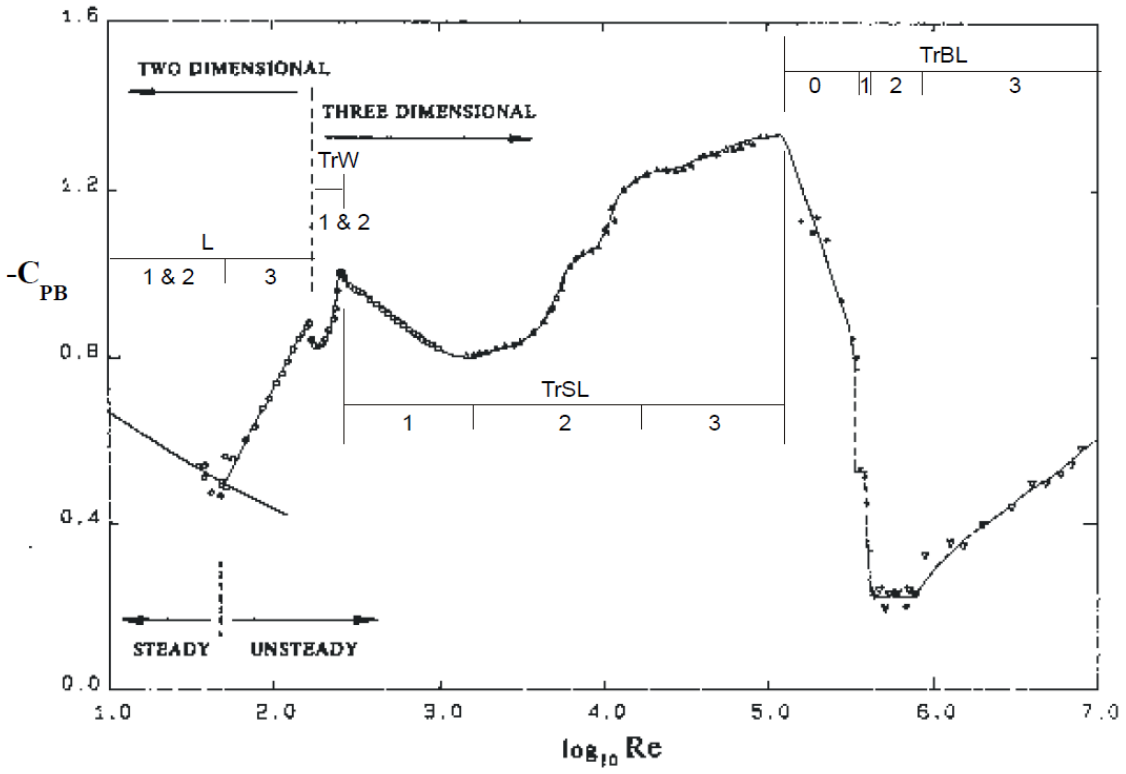

FIGURE 1.1: Variation of base suction coefficient with Re, reproduced by Carberry [1].

the upper and lower surfaces of the cylinder, resulting in a distinct pattern of oppositely signed vortices, which is well-known as the Kármán vortex street.

At the beginning of the TrW1 regime around Re=180-200, there is a sudden drop in the base suction coefficient $-C_{pb}$, which is the negative of the pressure coefficient C_p

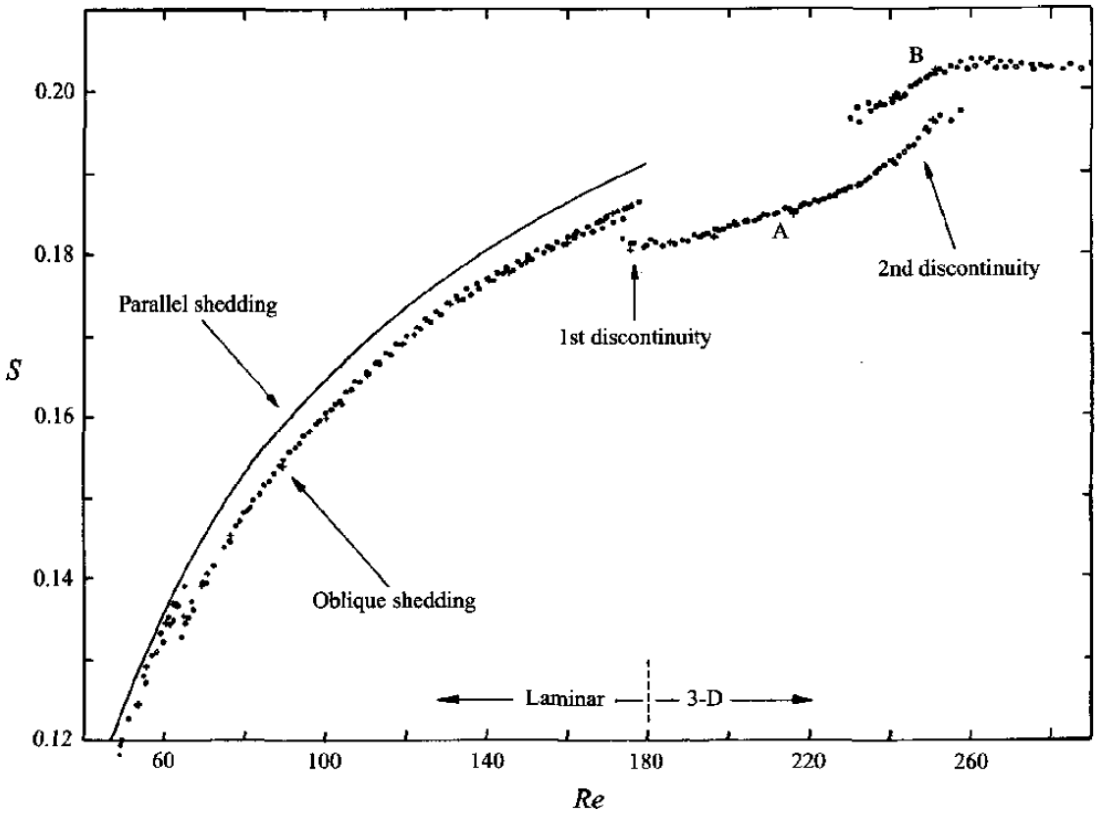

FIGURE 1.2: St-Re relationship showing two distinct discontinuities, indicating the onset of the mode-A and B instability, reproduced by Carberry [1].

near the cylinder base, and Strouhal number as shown in Figure 1.1 and Figure 1.2 respectively, which were reproduced by Carberry [1]. $-C_{pb}$ is quite sensitive to the vortex formation process in the near wake because this wake parameter strongly correlates with the large-scale vortex formation length, shedding frequency (i.e. Strouhal number) and spanwise vorticity of the Kármán vortices. The experimental study of Williamson [13] described that the changes in $-C_{pb}$ and St are primarily associated with the growth of spanwise (i.e. cylinder axis) instabilities resulting in a 3-D wake structure and the 3-D structures corresponding to TrW1 and TrW2 regimes are known as mode-A and mode-B respectively.

The streamwise structures of the mode-A and mode-B have distinctly different symmetries and scales as discussed in Williamson [14]. The transition between two modes is well explained by the discontinuity of the Strouhal number as shown in Figure 1.2. The first mode, named mode-A, is characterised by the inception of the existing streamwise vortices. The primary vortices roll up and deform in a wavy pattern along their spanwise direction during the process of shedding, which results in the local streamwise vortices along the cylinder axis as shown in Figure 1.3(a-left). The second mode, namely

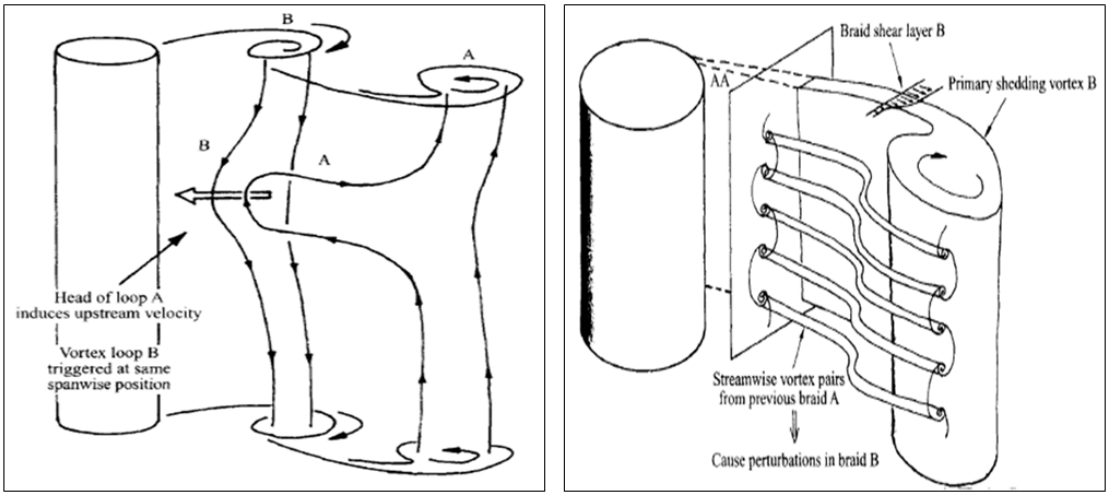

(a) Physical mechanism of mode-A (left) and B (right) instability, reproduced by Williamson [14].

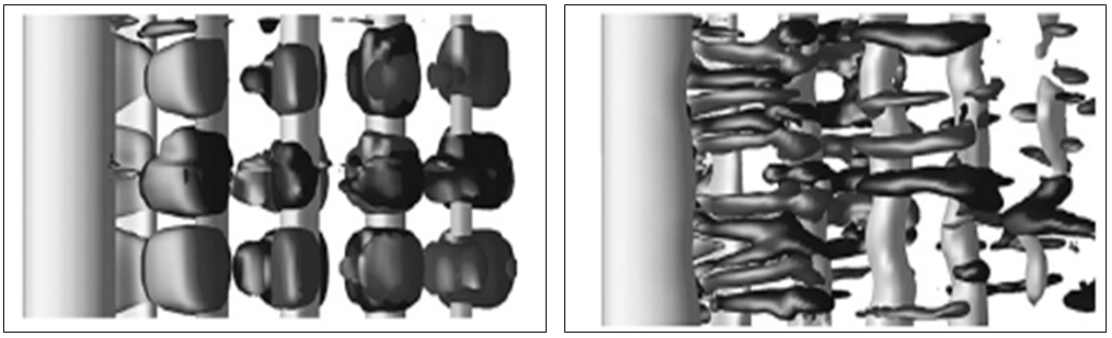

(b) Mode-A at Re=200 (left) and B at Re=300 (right), reproduced by Labbé and Wilson [15].

FIGURE 1.3: The mode-A and B instabilities: conceptual sketches (a) and 3-D simulation results (b).

mode-B associated with the second discontinuity, is characterised by the formation of finer-scale streamwise vortices in shear-layer region, where the instability is generated by the interaction between the forming shear layer and the existing streamwise vorticity in the opposite shear layer as shown in Figure 1.3(a-right). As shown in Figure 1.3(b), Labbé and Wilson [15] conducted 3-D large-eddy simulation at a range of Reynolds numbers and numerically captured the presence of mode-A and B at Re=200 and 300 respectively. Furthermore, their studies stressed the importance of the proper spanwise extension $L_Z{=}\pi D$ in order to predict the 3-D flow features along the cylinder axis direction accurately.

As the Reynolds number increases, next transition occurs in the freely separating shear layers behind a cylinder. In the range of transition in shear-layer or within subcritical Reynolds numbers, the flow behind a cylinder is experienced with a combination of a laminar boundary layer, separating shear layers, small-scale turbulent wake and

large-scale Strouhal vortices. Within the TrSL1 regime, the three-dimensionality of the streamwise vortex structures in the near wake becomes increasingly disordered and there is an accompanying increase in the length of the wake. The transition between TrSL1 and TrSL2 regime at Re≈1000 is characterised by a local minimum of $-C_{pb}$ as shown in Figure 1.1 and in root-mean-square (r.m.s.) of lift coefficient C'_L in Figure 1.4, measured from Norberg [2]. Additionally, the onset of small-scale spanwise vortices within the thin shear layers also occurs within this regime.

The shear layers separated from the thin boundary layer of a circular cylinder are experimentally observed to be unstable above a certain Reynolds number Re_{crit}. Due to the three-dimensional nature of the complex flow within the separated layers often termed the shear-layer instability or Kelvin-Helmholtz (KH) instability, the small-scale vortices in the shear layer are produced with substantial spanwise distortion which develop in the layers prior to the formation of large-scale Strouhal vortices.

The pioneering study of small-scale vortices on the onset of the shear-layer transition at a certain Reynolds number Re_{crit} with predominant shear-layer frequency f_{SL} was conducted by Bloor [16]. It was suggested that the instability starts at Re_{crit} ≈1300

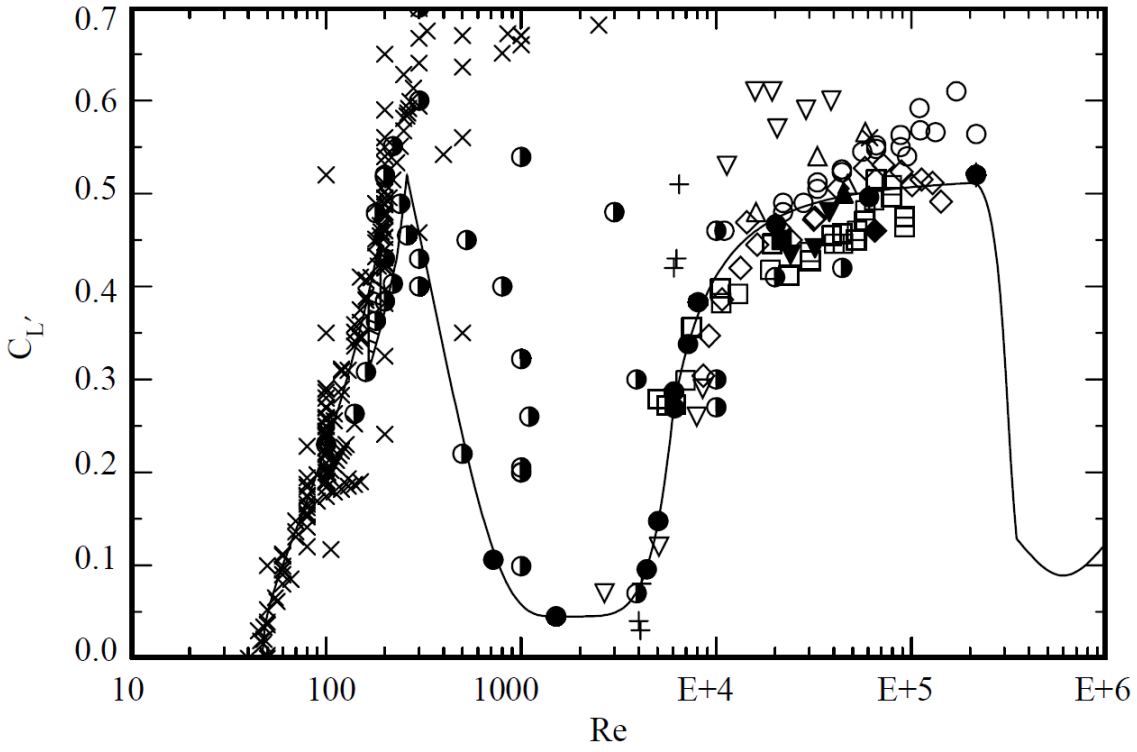

FIGURE 1.4: Variation of r.m.s. lift coefficient C'_L with Reynolds number, reproduced by Norberg [2].

and shear-layer frequency to the Kármán frequency ratio f_{SL}/f_K is scaled with $\mathrm{Re}^{0.5}$. Unal and Rockwell [17] measured $\mathrm{Re}_{crit} \approx$1,900 and Wu et al. [18] stated that there is a transitional region between Re=1000 and 3000, and the precise Re_{crit} for the onset of the small-scale vortices is found to be dependent on turbulence background condition.

The variation of the normalised shear-layer frequency has been intensively studied in previous experiments: see Wei and Smith [21], Norberg [22], Chyu et al. [23] and references therein. Prasad and Williamson [24] conducted an evaluation of previous experimental data and suggested the relationship $f_{SL}/f_K = 0.0235 \times \mathrm{Re}^{0.67}$ for the range of Re=1200-45000. Figure 1.5 shows the variation of shear-layer frequency with the Reynolds number suggested by Prasad and Williamson [24], including the recent numerical results obtained with direct numerical simulation by Dong et al. [3]. More recently, Rajagopalan and Antonia [25] observed $\mathrm{Re}_{crit} \approx$1480 when the instability first appears

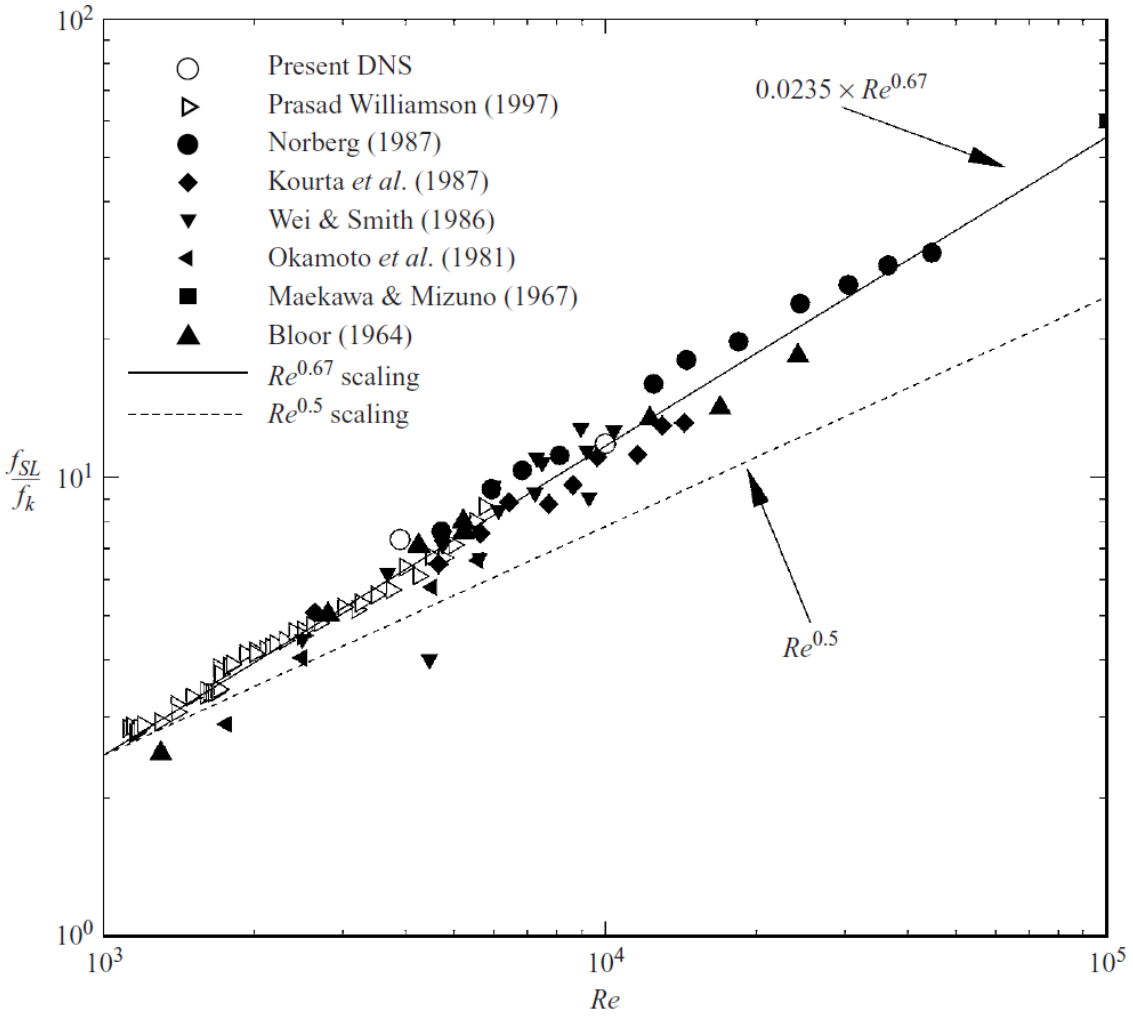

FIGURE 1.5: Variation of shear-layer frequency with Reynolds number, reproduced by Dong et al. [3].

and found the existence of vortex pairing in the separating shear layer and also provided a scale exponent of 0.65, which is in agreement with the $Re^{0.67}$ power law suggested by Prasad and Williamson [24]. Thompson and Hourigan [19] provided an excellent review and data concerning on this phenomenon. Their results showed a $Re^{0.57}$ dependence for Re<4000 and $Re^{0.52}$ for Re>10000.

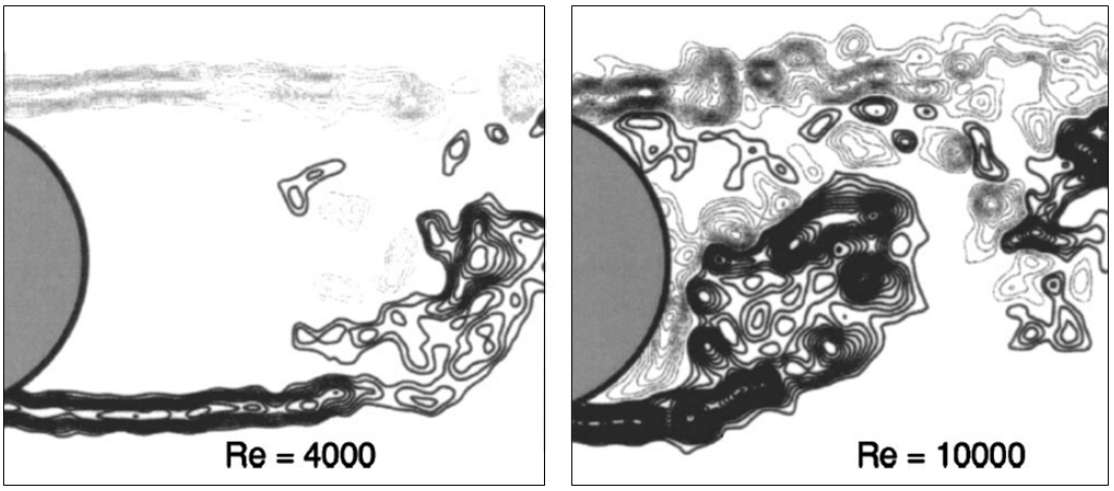

(a) Representative instantaneous vorticity fields showing the significant change in the near-wake structure as the Reynolds number is varied within the subcritical regime, reproduced by Thompson and Hourigan [19].

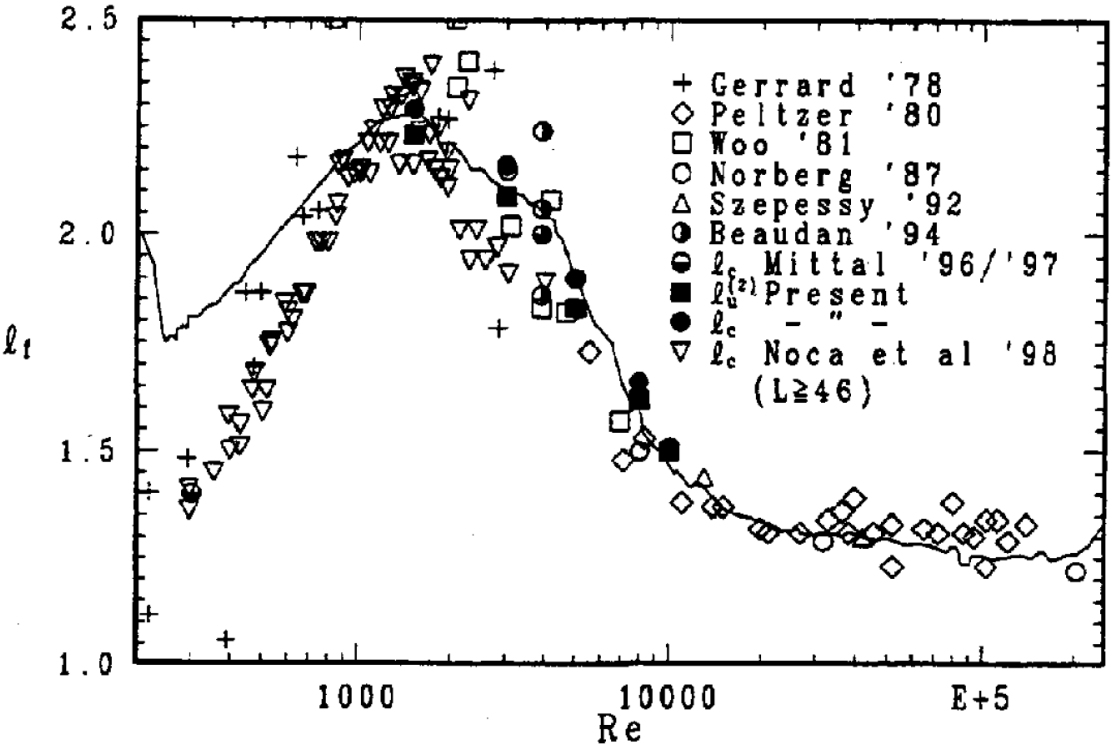

(b) Variation of vortex formation length with Reynolds number, reproduced by Norberg [20].

FIGURE 1.6: Variation of near-wake structure with Reynolds number.

As the Reynolds number increases up to TrSL2 and TrSL3, the transition to turbulence, or the length of the shear layers evolved from the thin boundary layer, continues to move upstream and finally reaches immediately after separation points close to cylinder surface as shown in Figure 1.6(a), produced by particle image velocimetry (PIV) experiment of Thompson and Hourigan [19]. The data measured by Norberg [20] in Figure 1.6(b) shows that the points at Re=4000 and 10000 also correspond to rapid change of the near-wake structure from a long formation length of the shear layers to an exceptionally short formation length.

The next transition region occurs in the boundary layer of a cylinder. It is the transition to turbulence within the boundary layers on the surface of the cylinder, which is characterised by sudden drop of drag coefficient as Reynolds number increases. When the Reynolds number reaches around Re=200000, it is termed the pre-critical range. In this regime, the attached boundary layer is laminar, the separated boundary layers are in the early stages of transition, and the wake is fully turbulent. At the transition between the subcritical and the single bubble regime, the sudden change of drag force corresponds to the formation of a separation-reattachment bubble on one side of the cylinder. As the Reynolds number increases up to the critical region, the boundary layer starts as laminar and gradually separates with turbulent reattachment, a separation bubble, and finally turbulent boundary layer separation. As the Reynolds number increases further, the separation bubbles begin to break down and the drag begins to recover in the supercritical regime.

1.3 Controlled-oscillating Cylinder

The periodic hydrodynamic force caused by the regular shedding of vortex structures behind a cylinder can excite the natural structural frequency of the body, resulting in VIV. The VIV of a body, for instance, offshore risers in the deep sea, pipe-line jumpers on the seabed and marine structures such as tension leg and spar platforms around the ocean free-surface, is of significant interests to upstream industries.

The force on a stationary cylinder is typically decomposed into transverse or crossflow lift force and in-line or streamwise drag force. Although drag force on a stationary cylinder has a large mean component, the amplitude of the fluctuating component of drag is

significantly smaller than the amplitude of fluctuating lift force on a stationary cylinder. Even though the fluctuating component of the drag force on an oscillating cylinder can be significant, VIV study of a cylinder in an experiment as well as simulation is often simplified by considering only the transverse motion of a cylinder due to the fluctuating lift force.

A common and robust approach to simplify the VIV problem is, therefore, to force the cylinder to oscillate transverse to the free stream with a predefined motion that approximates the vortex-induced motion. In general the vortex-induced motion of a cylinder is relatively sinusoidal and can be approximated by forcing a cylinder to oscillate with a pure sinusoidal motion:

$$y(t) = A\sin(2\pi f_e t), \tag{1.1}$$

The periodic motion of the cylinder is described in terms of normalised amplitude ratio A/D and normalised frequency ratio f_e/f_K, where A is the amplitude of oscillation and f_e is the excitation frequency of the cylinder oscillation.

In the present study, forced or controlled oscillation of a cylinder in steady flow is employed to achieve a deeper understanding of VIV phenomena and to enable effective comparison with very recent forced-oscillation experiments.

1.3.1 Characteristic features of an oscillating cylinder

Bishop and Hassan [26] experimentally investigated the forces exerted on an oscillating cylinder. Their experiments showed that there was an abrupt jump in lift phase angle ϕ_L between the lift force C_L and the cylinder motion y when f_e is varied around the natural shedding frequency f_K. They also observed an increase of both drag and lift forces near frequency ratio $f_e/f_K \approx 1.0$. This simultaneous and sharp change in the amplitude and phase of lift force has subsequently been observed by a number of investigators including Sarpkaya [27].

In Figure 1.7, the lift properties, lift phase and force, obtained by previous oscillating cylinder experiments are plotted as a function of f_e/f_K for a range of Re=5000 to 60000. Each set of data shows an abrupt jump in ϕ_L and a corresponding sharp change in C_L at the same frequency of oscillation. However, between the different data sets there is some

variation in the frequency at which the jump occurs. The simultaneous jump in both the phase and amplitude of lift force suggests that around $f_e/f_K \approx 1$ there is a significant change in near-wake structure of a cylinder.

Williamson and Roshko [28] performed the well-known flow visualisation experiment of forced oscillation in order to identify the wake patterns in the range of lock-in, covering a series of A/D and frequency ratios over $300 < \mathrm{Re} < 1000$. The term lock-in is used to describe the wake when the periodic shedding of vortex structures and the resulting fluctuating forces are synchronised with the motion of the body.

In the lock-in regions of the map, three principal vortex-shedding modes near $f_e/f_K \approx 1.0$ were identified as 2S, 2P, and P+S. The letter S represents a single vortex and the letter P represents a vortex pair. The 2S mode represents the shedding of a single vortex in each half-cycle of oscillation similar to the natural Kármán vortex shedding. The 2P mode represents two count-rotating pairs of vortices shed per oscillation cycle. The P+S mode is an asymmetric pattern with one pair and one single vortex per cycle. The classification of the wake modes is quite important when used to explain the variation of the hydrodynamic forces acting on the cylinder.

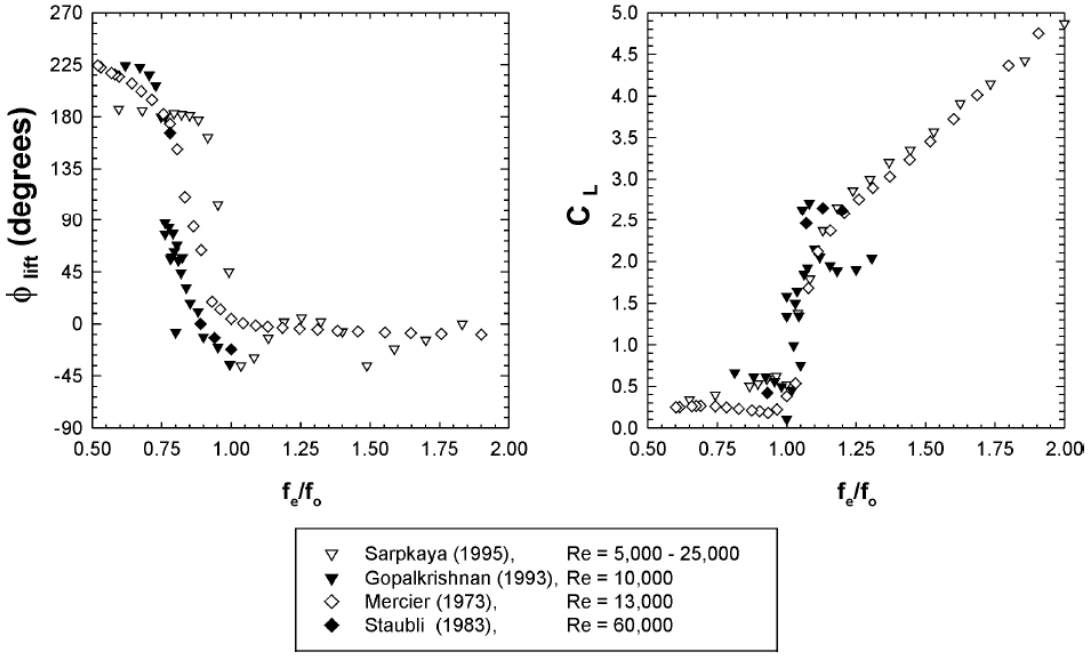

FIGURE 1.7: Compilation of previous data showing the variation of the phase of the lift force (left) and the amplitude of the lift force (right) as a function of the frequency ratio; In all cases A/D=0.5, reproduced by Carberry et al. [4].

More recently, Morse and Williamson [5] re-conducted the same forced-oscillation experiment to present further amplitude-response prediction and re-identify the relationship between forced oscillation and free-vibration at higher Reynolds numbers of 4000 and 12000 with much higher resolution than in the previous experiment they conducted, as shown in Figure 1.8. Note that y-axis on the map is A/D and x-axis is in terms of the normalised wave length ratio defined as:

$$\frac{UT_e}{D} = \frac{\lambda}{D} \approx \frac{T_e}{T_K} = \frac{f_K}{f_e}, \tag{1.2}$$

where T_e and T_K is the oscillating period and the natural shedding period respectively. The horizontal axis T_e/T_K was derived assuming that the Strouhal number is close to 0.2. In their experiments, a high-amplitude regime in which two vortex-formation modes overlap was observed. Associated with this overlap regime, a new mode of vortex formation comprised of two pairs of vortices formed per cycle, where the secondary vortex in each pair is much weaker than the primary one, was identified as the 2P overlap mode,

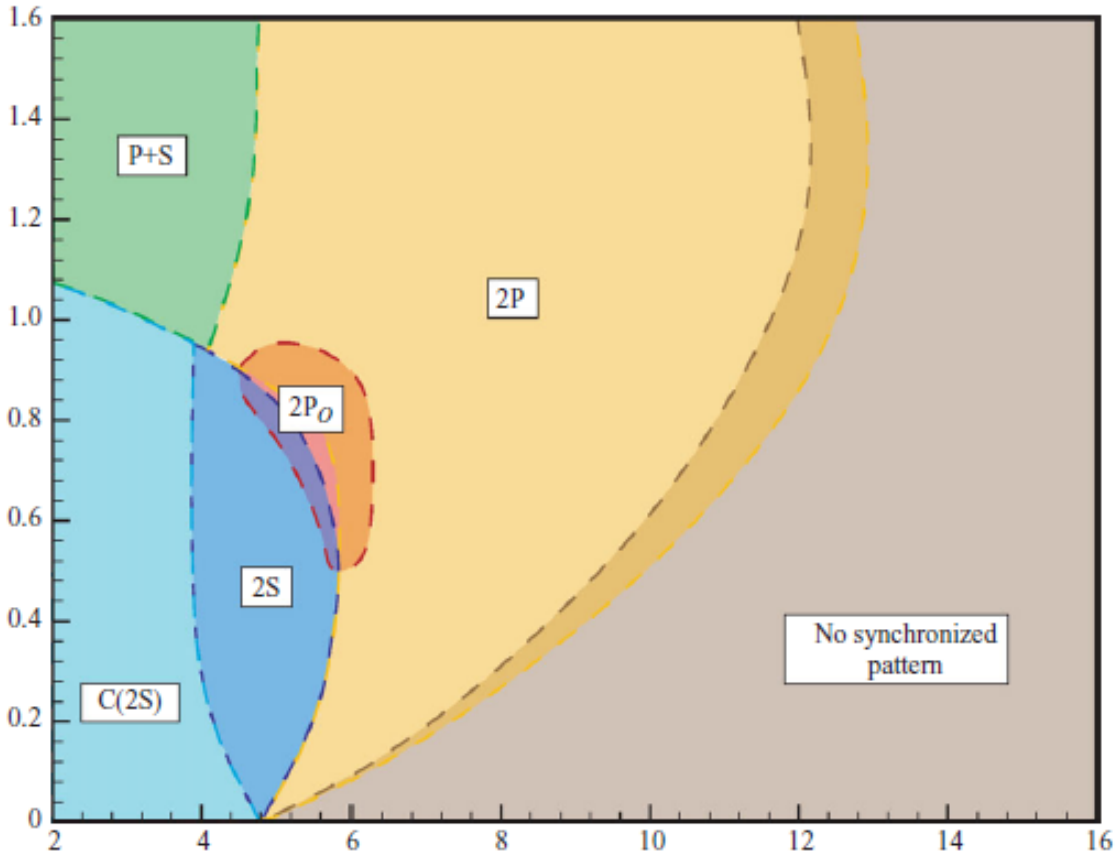

FIGURE 1.8: The map of vortex synchronisation patterns near the fundamental lock-in region, reproduced by Morse and Williamson [5].

$2P_o$. Figure 1.9 shows the four main wake modes of an oscillating cylinder obtained by Morse and Williamson [5].

Ongoren and Rockwell [29] and Gu et al. [6] also considered the variation of the wake as f_e/f_K increased unity, focusing on the changes in the near-wake structures behind an oscillating circular cylinder. They used small amplitude ratios of 0.2 and below. At this small amplitude ratio no evidence of the wake modes were found, but their experiments clearly showed that there is a switch in timing of the vortex formation across the lift phase jump found by Bishop and Hassan [26]. As f_e/f_K approaches unity with a relatively low amplitude, elongated vorticity in the wake moves closer to the cylinder and forms a tight vorticity concentration in one side of the cylinder. At $f_e/f_K \approx 1$ the initially formed vorticity concentration abruptly switches to the opposite side of the cylinder. This abrupt switch in the sign of the initial vortex was also observed at both laminar and subcritical Reynolds numbers of 185 and 5000. The change in the sign of the initial

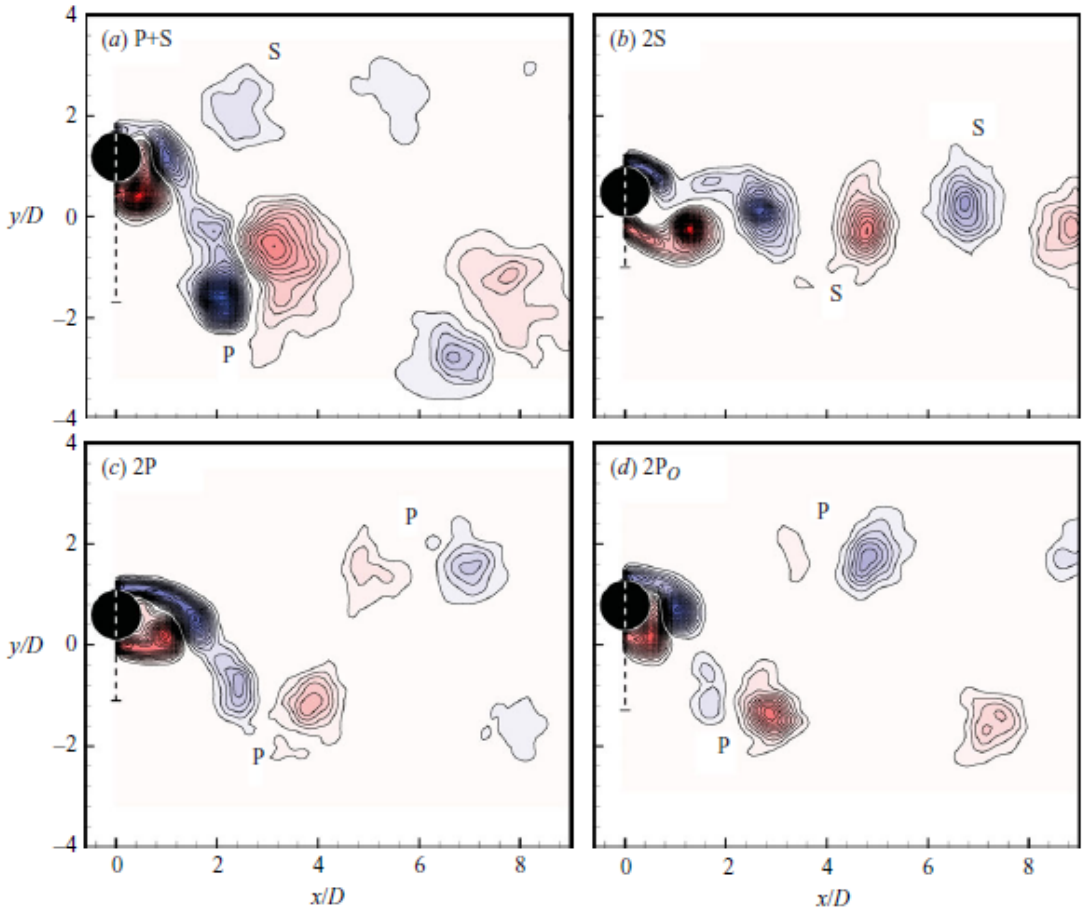

FIGURE 1.9: Phase-averaged vorticity fields for the main vortex-shedding modes obtained in force-oscillation experiments, reproduced by Morse and Williamson [5].

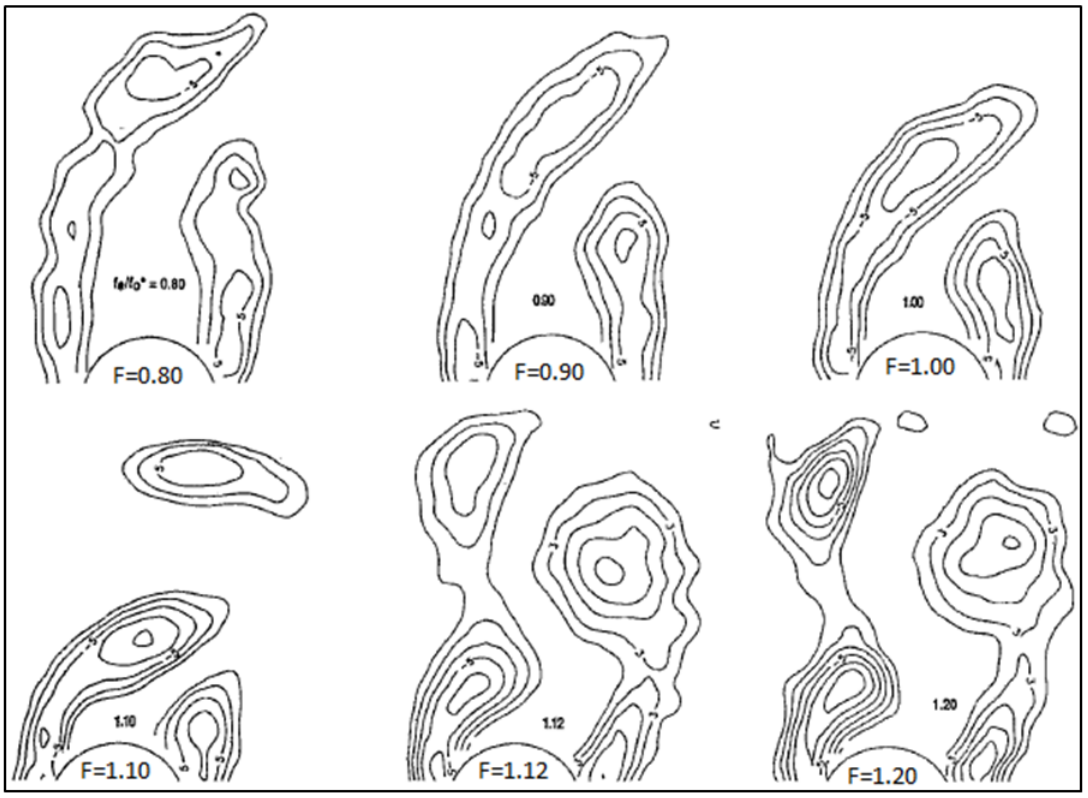

FIGURE 1.10: Instantaneous contours of vorticity of the wake from an oscillating cylinder as a function of frequency ratio at Re=185 and A/D=0.2 in PIV experiments. In all images, location of the cylinder is at its extreme leftward position, reproduced by Gu et al. [6].

vortex implies a significant change in the phase of vortex shedding. As shown in Figure 1.10 measured by Gu et al. [6], the switching process occurred at $1.10 \leq f_e/f_K \leq 1.12$ for the laminar flow regime.

Gopalkrishnan [30] carried out forced-oscillation experiments in a towing tank and produced extensive plots of the lift force and phase at Re=10000. He demonstrated that the lift coefficients experience a sharp increase close to the Strouhal frequency, $f_e/f_K \approx 0.9$, and compiled lift in phase with velocity and acceleration over a wide range of normalised amplitude and wavelength ratios together with previous data sets as shown in Figure 1.7.

Recently, Carberry et al. [4, 7, 31] performed careful and systematic controlled-oscillation experiments and the frequency dependence of the wake was considered over a series of amplitude ratios and higher Reynolds numbers, $0.25 \leq A/D \leq 0.6$ and $2300 \leq \mathrm{Re} \leq 9100$. Their experiments clearly demonstrated that the low- and high-frequency wake states, which are characterised by the changes in the lift properties as described in Table 1.2,

TABLE 1.2: Summary of the characteristic lift force phases for the forced wake states, originally by Carberry [1].

Wake states	Low-frequency	Intermediate	High-frequency
ϕ_L	High (around 180° 2nd or 3rd quadrant)	Low (near 0°)	Low (near 0°)
$\phi_{L\text{vortex}}$	High (≈180°)	High (≈180°)	Low (0° to -90° at higher f_e/f_K)

exhibited the 2P and 2S wake mode respectively. Furthermore, they clearly identified the intermediate wake state as a link between two different wake states. Within the intermediate state, they showed that two wake modes are intrinsically linked by one-time transition, even while the amplitude and frequency were held constant.

Their experiments also showed the self-excited transition, which is the behaviour of the lift coefficient from out-of-phase to in-phase with the cylinder displacement at a certain single frequency ratio as time increased. However, they reported that the self-excited transitions from one to another wake state were observed in a relatively high A/D=0.5 and 0.6 at Re=2300 only, indicating that the transition is either very narrow between excitation frequencies or dependent on either the Reynolds number or amplitude ratio.

In the self-excited transition at A/D=0.5 and Re=2300 from their experiment, a new wake mode distinctly different from the 2P and 2S wake modes was observed and the wake mode was characterised by phase angle of the vortex lift coefficient $\phi_{L\,vortex}$ defined as:

$$C_{L\,vortex}(t) = C_{L\,total}(t) - C_{L\,am}(t), \tag{1.3}$$

$$C_{L\,vortex}(t) \approx C_{L\,vortex}\sin(2\pi f_e t + \phi_{L\,vortex}), \tag{1.4}$$

where, $C_{L\,total}(t)$ is the instantaneous total lift force coefficient and $C_{L\,am}(t)$ is instantaneous lift coefficient caused by the apparent mass generated by the acceleration of fluid as the cylinder accelerates. The new wake mode in the intermediate wake state is equivalent to the $2P_o$ mode observed by Morse and Williamson [5] later. Figure 1.11 shows the distinct corresponding wake modes in each wake state obtained by Carberry et al. [7].

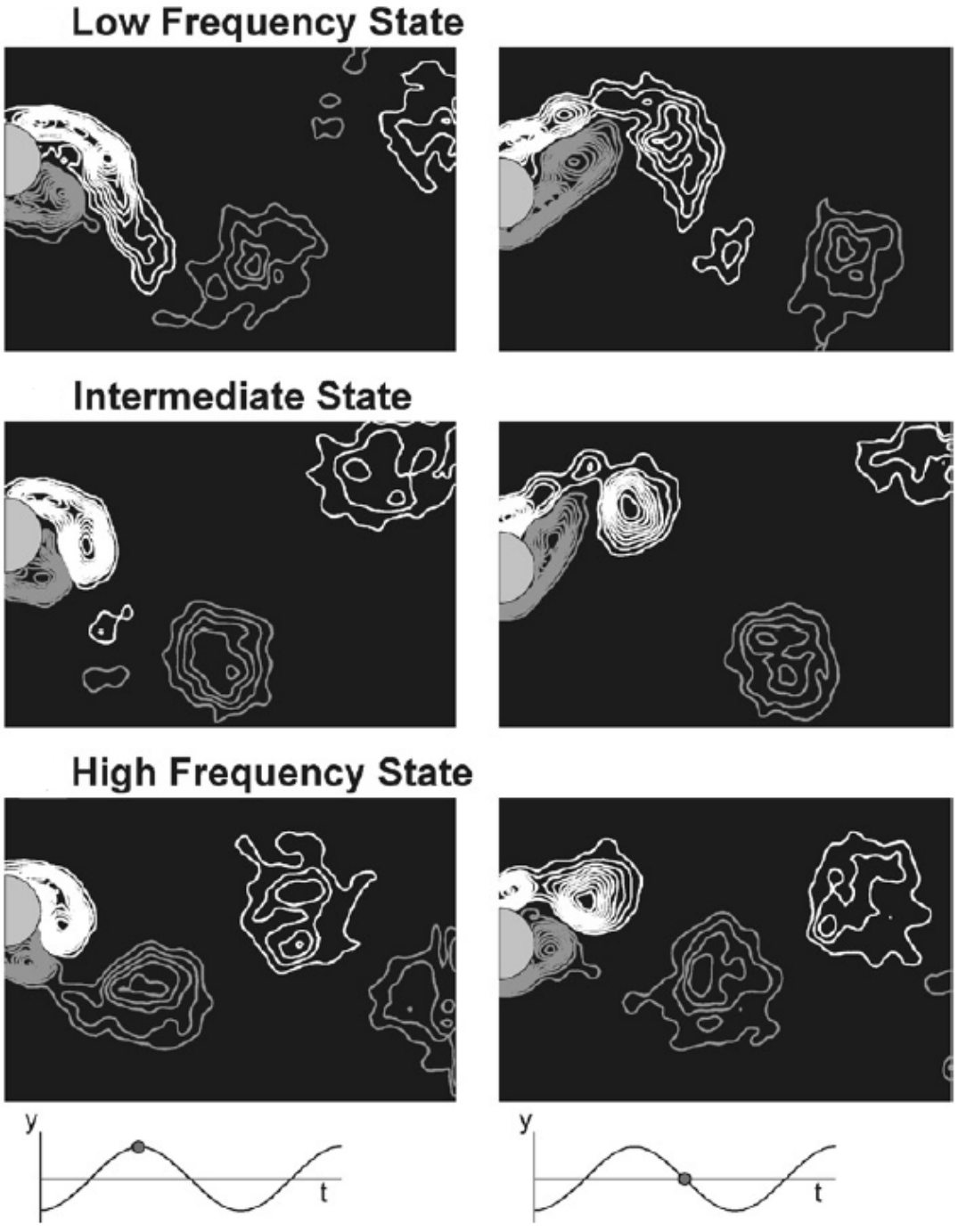

FIGURE 1.11: Phase averaged vorticity fields, showing the low-, intermediate and high-frequency wake states at A/D=0.5 and Re=2300; Location of the cylinder is the top (left column) and mid-point (right column) of the downward motion of the cylinder, reproduced by Carberry et al. [7].

1.4 Numerical Simulation of Cylinder Flow

The turbulent flow behind a cylinder provides additional challenges for computational modelling, because it involves extremely complex flow features such as freely separating

shear layers from the thin boundary layer, small-scale shear-layer vortices, transition and large-scale vortex shedding behind the simple geometry, as discussed in previous sections. As a result, numerous two- and three-dimensional computational studies of the cylinder flow have been conducted using various numerical approaches such as direct numerical simulation (DNS), large-eddy simulation (LES) and Unsteady Reynolds-Averaged Navier-Stokes (URANS) approaches.

1.4.1 Numerical approach

DNS is a simulation technique in which the Navier-Stokes equations are solved without any turbulence model and approximation. The entire range of spatial and temporal properties of the turbulence are directly resolved, from the smallest energy dissipative scales to the largest kinetic energy carrying scales. Unfortunately, DNS approach is often very time- and memory-consuming in the case of complex flows and therefore the applications for this method are limited to only lower Reynolds numbers. In contrast to DNS, turbulent fluctuations of flow quantities are not resolved in the URANS approach. Hence, it can help to save computing resources in complex flow situations at higher Reynolds numbers.

Recently, the LES technique by modeling turbulent fluctuations tends to be increasingly adopted for the oil and gas industries, for which URANS approach is incapable of accurately predicting unsteady hydrodynamic forces and pressure acting on the offshore structure in a harsh ocean environment, which is mostly attributed to the significant increase in the high performance computing capacity. Therefore, the LES approach is an attractive alternative. A paradigmatic example of such challenging flows is bluff-body flow. Figure 1.12 briefly shows the difference between the LES and URANS methods for cylinder flow performed by Catalano et al. [8] and they noted that the LES solutions are shown to be considerably more accurate than the URANS results.

In order to show the necessity for 3-D computations, a set of numerical simulations of a stationary cylinder flow was performed by Breuer [32] at Re=3900 in which 3-D spanwise vortices are well-developed. In their study, totally different streamline patterns between 2- and 3-D calculations were captured. Furthermore, the predicted drag and back pressure are much too high in the 2-D case compared with experimental measurement. The

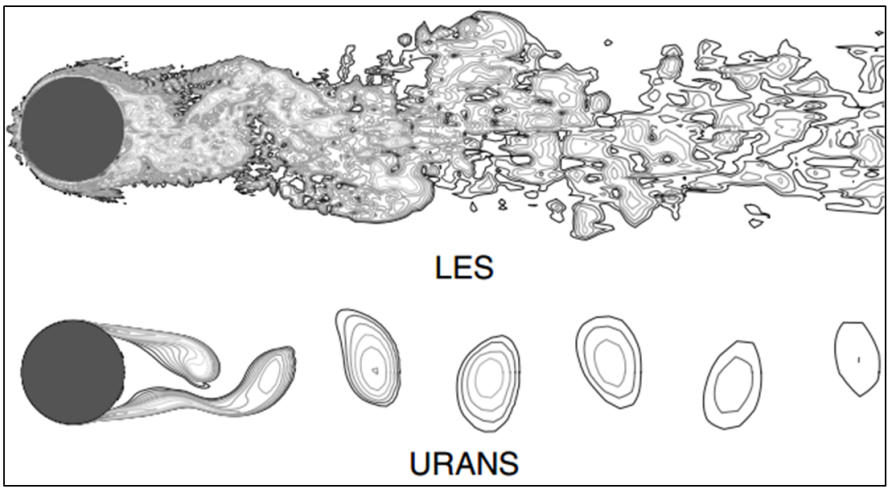

(a) Instantaneous vorticity magnitude at a given spanwise cut.

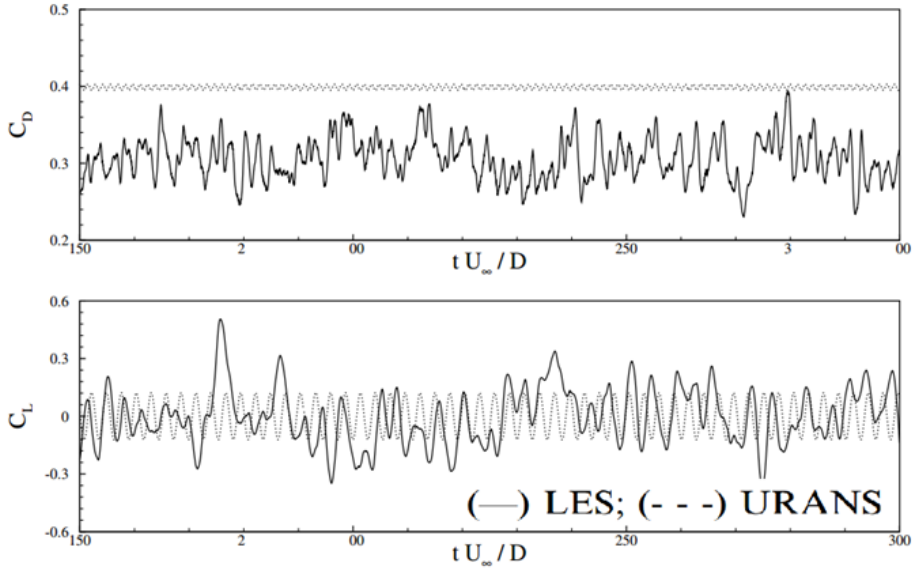

(b) Time histories of drag and lift coefficient.

FIGURE 1.12: Comparisons between the LES and URANS methods for cylinder flow, reproduced by Catalano et al. [8].

large deviations between the 2-D and 3-D results indicate that three-dimensional structures strongly influence the near wake of the flow. They noted that the result is an illustrative proof that 2-D simulation is useless owing to the impact of three-dimensionality of the flow even in the case of nearly two-dimensional flow problems. Moreover, Blackburn et al. [9] conducted 3-D DNS study of the flow past a freely vibrating cylinder at Re=556 in which the dimensionality is just developing. They stressed the significance of three-dimensionality in the wake and also suggested that 3-D simulation is required in order to reproduce wake response observed in experiments, even at low Reynolds numbers.

The present numerical study will consider the complex flow behind a stationary and oscillating cylinder especially in the frame of the 3-D LES technique based on the previous careful numerical studies. The following review, therefore, restricts the cylinder flow simulations especially using 3-D LES and 3-D DNS.

1.4.2 Numerical study of stationary cylinder flow

Several 3-D numerical studies of a fixed cylinder flow have been carried out at various Reynolds numbers. The cylinder flow at subcritical Reynolds numbers, especially at Re=3900/4000, has been widely investigated using the LES technique during recent decades, mainly due to available experimental results regarding the Reynolds number.

Beaudan and Moin [33] are among the first to conduct LES calculations at the Reynolds number of 3900. In several other numerical investigations including the work of Mittal and Moin [34], the effect of influencing factors on LES such as the grid resolution in the spanwise direction, subgrid scale (SGS) model and discretisation scheme especially for the convection terms in the Navier-Stokes equations have been widely examined. Most numerical studies adopted the cylinder length to diameter ratio equal to $L_z/D=\pi$ with 48 control volume $N_z=48$. Moreover, there is general consensus that low-order upwind schemes are not sufficient to predict the main wake parameter correctly.

In the study conducted by Breuer [32], various aspects of LES simulation such as the discretisation scheme and SGS model were carefully examined. Their results obtained with the Smagorinsky and dynamic model were close to each other at the low Reynolds number. Kravchenko and Moin [35] also indicated that LES of the cylinder flow does not strongly depend on a SGS model.

Dong et al. [3] studied the Reynolds number effect from Re=3900-10000 using the DNS approach and a number of flow statistics were calculated correctly compared with their PIV experimental measurements. They captured the broadband nature of the shear-layer frequency at Re=3900, but the frequency at a higher Reynolds number of 10000 exhibited the plateau feature in their power spectra. The DNS study clearly showed that the predominant frequencies of shear-layer vortices follow the $\mathrm{Re}^{0.67}$ power law as the Reynolds number increased from Re=3900-10000.

At a higher Reynolds number of 8000, Jordan [36] studied the shear-layer instability employing a dynamic SGS model with a high-order upwind scheme and a number of wake quantities were correctly predicted. They noted that the dynamic model has little influence on the predicted shear-layer features.

The pioneering LES simulation was conducted by Breuer [37] at Re=140000 and two different SGS models, the Smagorinsky and dynamic Smagorinsky, were evaluated on coarse and finer grid resolutions with a central difference scheme. Their study stressed that the importance of the SGS model significantly increases for higher Reynolds numbers. In order to model turbulent flow at the high Reynolds number, the dynamic turbulence model was applied to calculate model constants dynamically. However, the superiority of the dynamic model over the conventional algebraic Smagorinsky model was not proved in their numerical study. In a recent numerical investigation of Wornom et al. [38], they conducted 3-D LES with a wall-adapting local eddy-viscosity (WALE) SGS model at Re=3900, 10000 and 20000. The wake parameters were predicted reasonably well at the lower Reynolds number, while the results are over-predicted at the higher ends of the Reynolds numbers and the flow statistics were not reported.

1.4.3 Numerical study of oscillating cylinder flow

Even with the limitation of 2-D simulation, it is widely applied to an oscillating cylinder problem. Lu and Dalton [10] performed a 2-D numerical study for an oscillating cylinder at Reynolds numbers of 185-1000 with respect to various amplitude ratios. As the

FIGURE 1.13: Instantaneous iso-surfaces of pressure (predominant alignment spanwise) and streamwise vorticity (predominantly streamwise) at Re=556 from 3-D simulation, reproduced by Blackburn et al. [9].

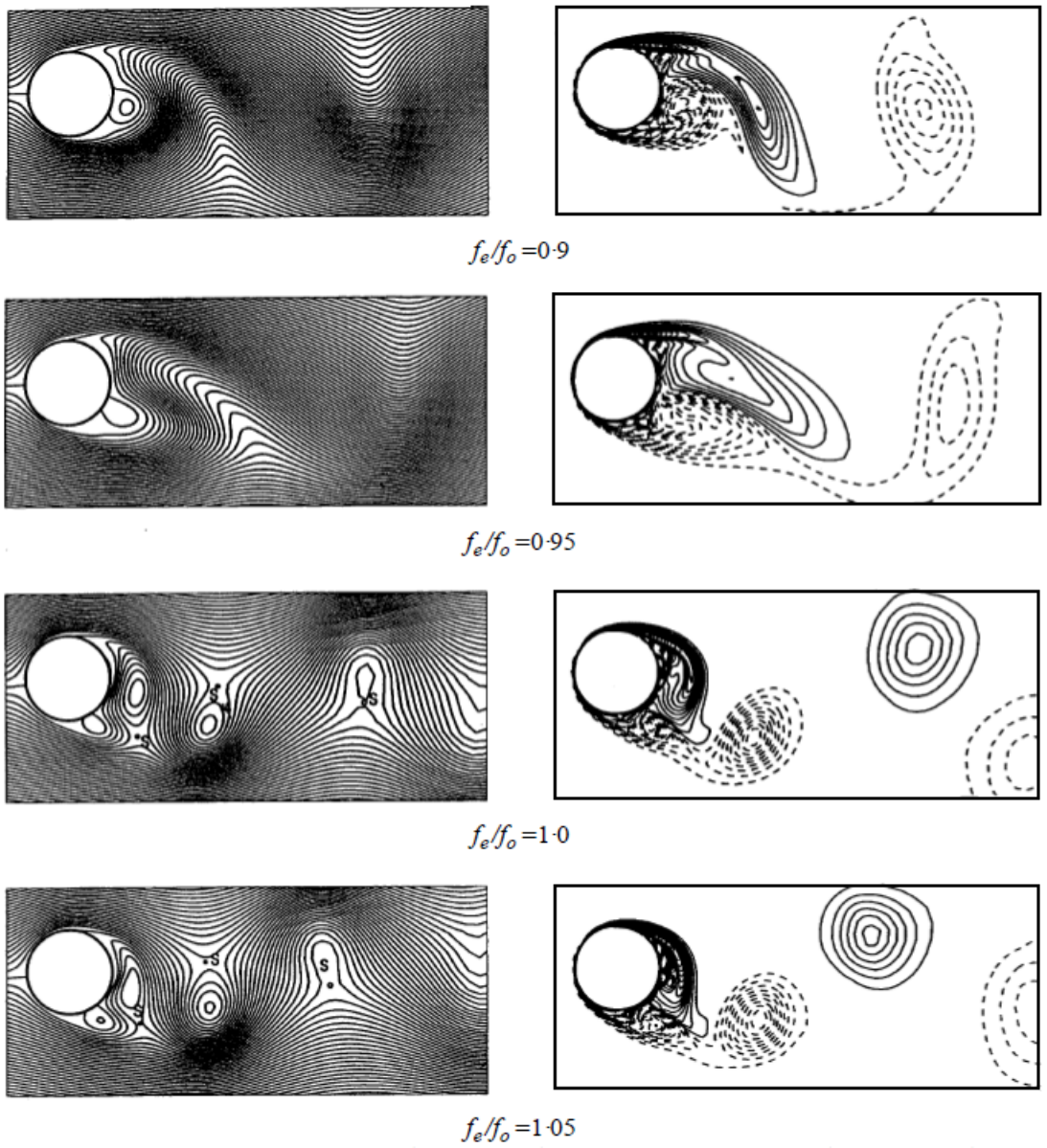

FIGURE 1.14: Instantaneous streamlines (left) and vorticity contours (right) of an oscillating cylinder flow at various f_e/f_K for A/D=0.4 and Re=1000 in 2-D simulation. In all frames, the location of the cylinder is at its extreme upper position, reproduced by Lu and Dalton [10].

frequency ratio increased to unity as shown in Figure 1.14, the wake vortex structure became closer to the cylinder base and a limiting position was reached. At the same time, the vorticity concentration abruptly switched to the opposite side of the cylinder. Their calculation clearly reproduced the phenomenon of vortex switching, observed in the experiment by Gu et al. [6]. Guilmineau and Queutey [39] also conducted 2-D simulations of in-line and cross-flow oscillating cylinders at Re=185, and their result was in good agreement with the previous numerical result conducted by Lu and Dalton [10]. Blackburn and Henderson [40] performed 2-D DNS of a controlled-oscillating cylinder

at Re=500 and validated that the abrupt change of the lift force around the shedding frequency of the cylinder was associated with the vortex switching phenomenon.

Tutar and Holdo [41] performed LES of a forced-oscillation problem at a higher Reynolds number of 24000 with a small amplitude ratio of 0.11. They provided instantaneous vorticity contours at four different excitation frequencies from 2-D and 3-D simulations, which showed a dependence of the vorticity contours on the excitation frequencies. Their results showed that 3-D LES gives more realistic flow field predictions compared to 2-D LES. Dong and Karniadakis [42] conducted 3-D DNS of an oscillating circular cylinder at Re=10000 with A/D=0.3. Their direct simulation showed that the drag and lift coefficient of the forced oscillation were predicted reasonably well compared with experimental data. Recently, Atluri et al. [43] performed extensive 2-D LES calculations of a forced-oscillation cylinder flow with a series of modulated excitation frequencies over a wide range of Re=500 to 6000 and found a qualitative agreement with experimental results.

Chapter 2

LES PRINCIPLES AND COMPUTATIONAL METHODOLOGY

Large eddy simulation is a numerical method used to predict turbulent flow based on the idea that the large scale turbulence motions of the flow are calculated explicitly, whereas the effect of the small scales is modelled using a subgrid scale model. This approach appears to be justified because the large-scale (or resolved scale) motions contain and transport most of the energy, whilst the contribution of the small scale (or subgrid scale) to the resolved scale is relatively small and universal.

Application of the LES technique to an incompressible turbulent flow in the present study consists of two main steps. First a filtering operation is performed on the incompressible Navier-Stokes equations to remove the small scales which are less than the filter size. The filtered equations then only contain the SGS stress tensor, which describes the effect of the unresolved small scales on the resolved scales. In the second step, the SGS stresses are expressed in terms of the resolved scales using a SGS model such as the algebraic Smagorinsky and the dynamic k-equation models.

This Chapter is divided into two parts with particular focus on the SGS modellings and their implementations for the cylinder flow. The filtered governing equations will be briefly introduced, followed by a detailed description of the SGS models used in the

present study. The solution approach using the finite volume method with discretisation schemes will be presented in the rest of this Chapter.

2.1 LES Governing Equations

The objective of the present study is to simulate turbulent flow behind a cylinder. Since the Mach number, free stream velocity-to-sound speed in water, is of the order 10^{-4}, the fluid is assumed to be incompressible, resulting in a constant and homogeneous density through the flow domain. The flow is subjected the Newtonian fluid properties and then the Navier-Stokes equations can be assumed as the governing equations describing the fluid dynamics. The external forces such as gravity and body forces are assumed negligible. Moreover, it is not expected that the temperature will have influence on the flow field throughout this thesis. Under these conditions, the Navier-Stokes equations can be written as follows:

$$\frac{\partial u_i}{\partial x_i} = 0, \tag{2.1}$$

$$\frac{\partial u_i}{\partial t} + \frac{\partial \left(u_i u_j\right)}{\partial x_j} = -\frac{1}{\rho}\frac{\partial p}{\partial x_i} + \frac{\partial}{\partial x_j}\left[\nu\left(\frac{\partial u_i}{\partial x_j} + \frac{\partial u_j}{\partial x_i}\right)\right], \tag{2.2}$$

where i, j=1, 2, 3, denoted as the streamwise, crossflow directions and stream normal direction respectively. p and ν are the pressure and kinematic viscosity of the fluid.

2.1.1 Filtering operation

The basic philosophy of LES is to explicitly simulate the large scale motion and only the effect of small scales needs to be modelled. A spatial filtering operation is used to decompose the flow variables into large and small scales.

The general flow variable f is composed of the large scale $\overline{f}$ (commonly referred to as mean, resolved or grid scale) and the small scale f' (fluctuation, modelled or subgrid scale):

$$f(\mathrm{x}) = \overline{f}(\mathrm{x}) + f'(\mathrm{x})\,, \tag{2.3}$$

In order to extract the large scale component $\overline{f}$, a filtering operation is applied. The filtering operation in the space is written as:

$$\overline{f}(\mathrm{x}) = \oint_D G\left(\mathrm{x}, \mathrm{x}'; \Delta\right) f\left(\mathrm{x}'\right)\, \mathrm{dx}', \tag{2.4}$$

$$\Delta = \sqrt[3]{\Delta_i \Delta_j \Delta_k}, \tag{2.5}$$

where D denotes the entire domain and G is the space-dependent three-dimensional filter function. An important feature of the filtering process is the filter width Δ. The characteristic length scale of the filter width Δ is often taken to be the cube root of the grid cell volume and $\Delta_{i,j,k}$ are the control volume spacings in each direction. The scale larger than Δ is retained in the filtered flow field, while the effects of scale smaller than Δ have to be modelled. The most common definition of the filter kernel is the volume filter:

$$G_i(\mathrm{x}_i - \mathrm{x}'_i) = \begin{cases} \frac{1}{\Delta_i} & \text{if } |\mathrm{x}_i - \mathrm{x}'_i| \leq \frac{\Delta_i}{2} \\ 0 & \text{otherwise} \end{cases}, \tag{2.6}$$

Therefore, the large scale component is given as:

$$\overline{f}(\mathrm{x}) = \frac{1}{\Delta^3} \int_{\mathrm{x}_i - \Delta_i/2}^{\mathrm{x}_i + \Delta_i/2} \int_{\mathrm{x}_j - \Delta_j/2}^{\mathrm{x}_j + \Delta_j/2} \int_{\mathrm{x}_k - \Delta_k/2}^{\mathrm{x}_k + \Delta_k/2} f\left(\mathrm{x}'_i, \mathrm{x}'_j, \mathrm{x}'_k\right)\, \mathrm{dx}'_i \mathrm{dx}'_j \mathrm{dx}'_k, \tag{2.7}$$

2.1.2 Filtered Navier-Stokes equations

Applying the filtering process to the incompressible Navier-Stokes equations gives:

$$\frac{\partial \overline{u}_i}{\partial x_i} = 0, \tag{2.8}$$

$$\frac{\partial \overline{u}_i}{\partial t} + \frac{\partial \overline{u_i u_j}}{\partial x_j} = -\frac{1}{\rho}\frac{\partial \overline{p}}{\partial x_i} + \frac{\partial}{\partial x_j}\left[\nu\left(\frac{\partial \overline{u}_i}{\partial x_j} + \frac{\partial \overline{u}_j}{\partial x_i}\right)\right], \tag{2.9}$$

where $\overline{u}$ and $\overline{p}$ are the filtered velocity and pressure. ν is the kinematic viscosity and ρ is the fluid density. The term $\overline{u_i u_j}$ can be written as follows:

$$\overline{u_i u_j} = -\overline{u}_i \overline{u}_j - \tau^s_{ij}, \tag{2.10}$$

where, τ_{ij}^s is the subgrid scale or Reynolds stress tensor. Therefore, the momentum equation is transformed to the LES governing equation for the large-scale momentum:

$$\frac{\partial \overline{u}_i}{\partial t} + \frac{\partial \overline{u}_i \overline{u}_j}{\partial x_j} = -\frac{1}{\rho}\frac{\partial \overline{p}}{\partial x_i} + \frac{\partial}{\partial x_j}\left[\nu\left(\frac{\partial \overline{u}_i}{\partial x_j} + \frac{\partial \overline{u}_j}{\partial x_i}\right) - \frac{1}{\rho}\tau_{ij}^s\right], \tag{2.11}$$

In order to approximate the SGS stress τ_{ij}^s in the equation, a SGS model can be introduced to close the equation. The main function of a SGS model is to dissipate or to dampen resolved turbulent fluctuations. Therefore, the turbulent dissipation is required to be properly represented by a SGS model.

2.2 Subgrid Scale Modelling

2.2.1 Energy spectrum

As discussed in the previous section, the basic philosophy of LES is to explicitly simulate the large scales (energy-carrying) and only the effect of small scales (energy-dissipative) is implicitly modelled by using a SGS model.

The turbulence is composed of a wide range of scales and one of the characteristic features of turbulent flow is that it is dissipative, which means that kinetic energy in the largest scale of eddies is extracted from the mean flow. The smaller eddies receive the energy from larger eddies. The energy transferred from larger to smaller eddies is eventually dissipated in the smallest eddy on the Kolmogorov scale, which is the smallest isotropic eddy in turbulent flow. Therefore, the generation of turbulent energy is essentially the result of the action of the large scales and the energy is then transferred in such a cascade manner to the smaller scales and is eventually dissipated by the smallest scale, as shown in Figure 2.1.

In the transportation region or inertial subrange, if the flow is fully turbulent flow at a higher Reynolds number, the energy spectra should exhibit a -5/3 decay in the inertial region according to the Kolmogorov spectrum law or -5/3 law:

$$E(k) = C_k \epsilon^{\frac{2}{3}} k^{-\frac{5}{3}}, \tag{2.12}$$

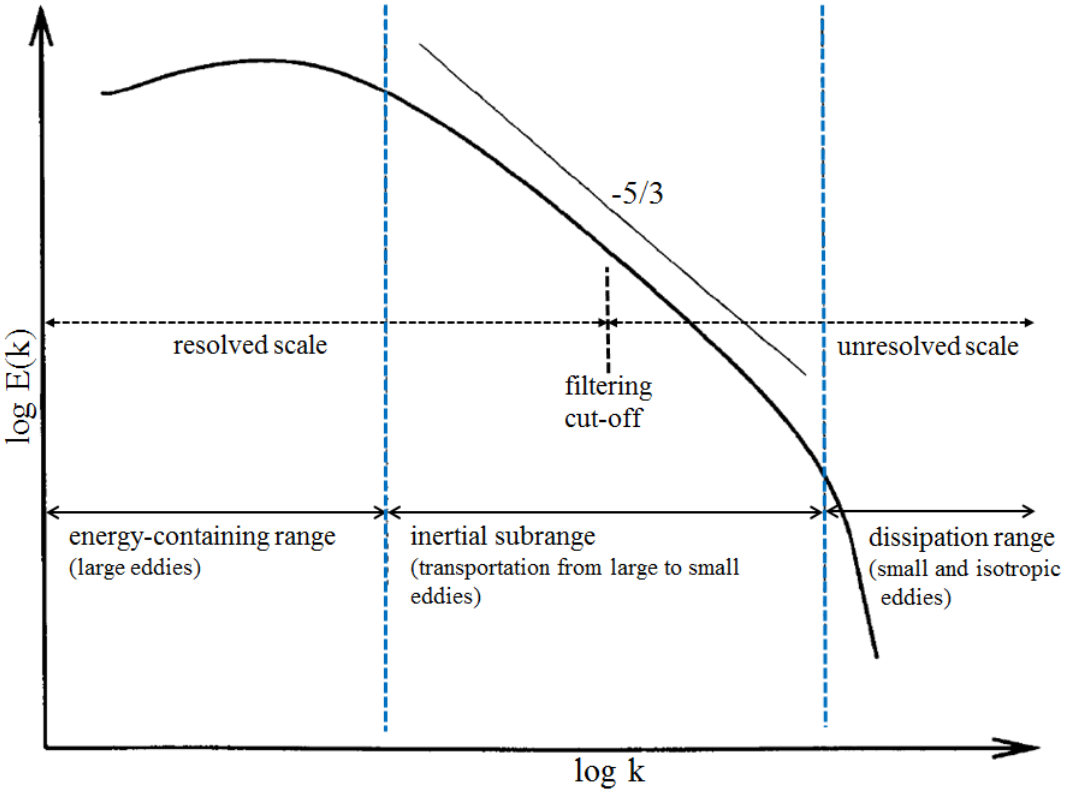

FIGURE 2.1: A sketch of the Kolmogorov turbulent kinetic energy k spectrum.

where, C_k is a universal constant and ϵ is the rate of energy dissipation. The filtering cut-off shall be operated at the inertial subrange of the energy spectra ideally. As a consequence, the grid resolution in LES is heavily dependent on the Reynolds number and is the main limitation for the simulation of flows in the presence of a wall.

2.2.2 Algebraic SGS models

In the spatially filtered Navier-Stokes equations, the unresolved scale is to be approximated using a SGS model to get a full solution for the filtered equations. The subgrid stress τ_{ij}^s in the filtered equations is expressed according to the Boussinesq's approximation by the adoption of a turbulent eddy viscosity ν_t:

$$\tau_{ij}^s - \frac{2}{3}k_t\delta_{ij} = -2\nu_t\left(\bar{S}_{ij} - \frac{1}{3}\bar{S}_{kk}\delta_{ij}\right), \tag{2.13}$$

where the resolved flow rate of the strain tensor and its deviatoric form are defined as:

$$\bar{S}_{ij} = \frac{1}{2}\left(\frac{\partial\bar{u}_i}{\partial x_j} + \frac{\partial\bar{u}_j}{\partial x_i}\right), \tag{2.14}$$

$$\bar{S}^*_{ij} = \bar{S}_{ij} - \frac{1}{3}\bar{S}_{kk}, \tag{2.15}$$

The SGS stress τ^s_{ij} represents the effect of SGS on the resolved scale and $\bar{S}_{ij}$ is the rate of the strain tensor computed from the resolved scales. The turbulent kinetic energy is defined as k_t=$0.5\tau_{kk}$. The Kronecker delta is expressed as δ_{ij}=1 if i=j and δ_{ij}=0 if $i \neq j$. It ensures that the normal stresses are taken as isotropic and the sum of the modelled normal SGS stresses is equal to the kinetic energy k_t.

Throughout the present study, two types of algebraic eddy-viscosity models and a dynamic model, namely the algebraic k-equation by Deardorff [44], algebraic Smagorinsky b Smagorinsky [45] and dynamic k-equation by Menon and Kim [46] models, are employed to evaluate the turbulent flow behind a cylinder. A comprehensive review of the SGS models is explained in great detail in Fureby [47].

In order to estimate k_t in Equation 2.13, the k-equation SGS model needs to solve an additional transportation or turbulent kinetic energy (TKE) equation followed by Yoshizawa [48]:

$$\frac{\partial k_t}{\partial t} + \frac{\partial}{\partial x_j}\left(\bar{u}_j k_t\right) = P + \frac{\partial}{\partial x_j}\left[\left(\nu + \nu_t\right)\frac{\partial k_t}{\partial x_j}\right] - \epsilon, \tag{2.16}$$

where P and ϵ terms are defined as:

$$P = -2\nu_t \bar{S}_{ij}\bar{S}_{ij}, \tag{2.17}$$

$$\epsilon = C_\epsilon k_t^{3/2}\Delta^{-1}, \tag{2.18}$$

where the turbulence viscosity is given by:

$$\nu_t = C_k \Delta k^{0.5}, \tag{2.19}$$

where $\bar{u}_j$ defines the fluctuating velocity component and Δ is the grid filter width estimated as the cubic root of the control volume as discussed in previous section. The first term on the right-hand side in Equation 2.16 represents shear production while the second and third terms represent transport processes or diffusion and dissipation respectively. The viscous dissipation ϵ is taken to be proportional to $k_t^{3/2}$. The dimensionless model constants are set equal to C_ϵ=1.00 and C_k=0.05 as suggested by Fureby et al. [49].

In contrast to the k-equation model, the conventional Smagorinsky model is based on the local equilibrium balance, P equals ϵ in Equation 2.16. Although the local equilibrium assumption does not normally hold true, the assumption is made to simplify the problem. In consequence, the turbulent kinetic energy k_t and viscosity ν_t are calculated explicitly as follows:

$$k_t = \frac{2C_k}{C_\epsilon}\Delta^2 \left|\bar{S}\right|^2, \tag{2.20}$$

$$\nu_t = (C_s\Delta)^2 \left(2\bar{S}_{ij}\bar{S}_{ij}\right)^{0.5} = \frac{C_k^{0.75}}{C_\epsilon^{0.25}}\Delta^2 \left|\bar{S}\right|, \tag{2.21}$$

Where, $\left|\bar{S}\right|$ is the magnitude of the strain rate tensor. The dimensionless model coefficients for cylinder flow are assigned to be the same as the values of C_ϵ=1.0 and C_k=0.05. Since the Smagorinsky model is based on the local equilibrium balance, the well-known Smagorinksy constant C_s can be re-covered in terms of C_k and C_ϵ according to Sullivan et al. [50]:

$$C_s = \left(C_k\sqrt{\frac{C_k}{C_\epsilon}}\right)^{1/2}, \tag{2.22}$$

This relationship of the model constants indicates that increasing C_k or decreasing C_ϵ corresponds to increasing C_s. The difference in C_s values is attributed to the effect of the mean flow strain or shear. In general, the Smagorinsky constant takes a value between 0.18 and 0.23, which is determined from isotropic turbulence decay. In the presence of shear, near solid boundaries or transitional flows, however, it has been found that it must be decreased to 0.065-0.1 since it is known that the Smagorinsky model tends to overestimate the eddy viscosity ν_t. In this study, substitution of the values of C_ϵ=1.0 and C_k=0.05 for the k-equation model results in C_s=0.1 in the Smagorinsky model, which is a typical value for practical applications of the Smagorinsky model indicated by Breuer [32].

Based on the successful computations of the cylinder flow conducted by Atluri et al. [43], a wall damping formulation suggested by Van Driest [51] is implemented together with the Smagorinsky model such that the turbulence is damped exponentially and the damping is derived by changing filter width Δ. As a result, Δ is locally adopted in time and space:

$$\Delta = \min\left(\frac{k_v}{C_\Delta}, \Delta\right) y \left(1 - \exp\left(\frac{-y^+}{25}\right)\right), \tag{2.23}$$

where the von Kármán constant k_v=0.4187 and model constant C_Δ=0.158. y^+ represents the non-dimensional distance to the wall calculated from the wall shear stress,

$y^+ = yu_\tau/\nu$ with $u_\tau = \sqrt{\tau_o/\rho}$, where τ_o is the wall shear stress.

2.2.3 Dynamic model

The introduction of dynamic modelling proposed by Germano et al. [52] has spurred significant progress in the SGS modelling. In the dynamic k-equation model the model coefficients C_ϵ and C_k are computed as part of the solution, based on the energy content of the smallest resolved scale, rather than input priori as in the algebraic k-equation model. This is accomplished by defining a test or second filter whose width $\widehat{\Delta}$ is larger than grid filter width Δ. Normally, the test filter width is taken as twice the grid filter width, $\widehat{\Delta}$=2Δ.

Dynamic adjustment of the model coefficient is based on the Germano identity:

$$\mathrm{L}_{ij} = \widehat{\overline{u_i}\overline{u_j}} - \widehat{\overline{u}_i}\widehat{\overline{u}_j} = \mathrm{T}_{ij} - \widehat{\tau^s_{ij}}, \tag{2.24}$$

where, the subtest stress T_{ij} is obtained by applying the test filter with the characteristic filter width $\widehat{\Delta}$ to the filtered Navier-Stokes equations:

$$\mathrm{T}_{ij} = \widehat{\overline{u_i u_j}} - \widehat{\overline{u}_i}\widehat{\overline{u}_j} = -2C_k\widehat{\Delta}K^{0.5}\widehat{\bar{S}^*_{ij}}, \tag{2.25}$$

Where, K is the test filter level energy. Similarly, the subgrid stress is given by:

$$\tau^s_{ij} = -2C_k\Delta k^{0.5}\bar{S}^*_{ij}, \tag{2.26}$$

Upon substituting the subtest and subgrid stresses into Equation 2.24, Piomelli [53] noted that the Germano identity can be satisfied only approximately, since the stresses are replaced by modelling assumptions, and the system is overdetermined. To minimise the error when solving the overdetermined system, a least-squares method proposed by Lilly [54] is applied and results in:

$$C_k = -\frac{1}{2}\frac{\mathrm{T}\cdot\mathrm{M}}{\mathrm{M}\cdot\mathrm{M}}, \tag{2.27}$$

Where, M=$\widehat{\Delta}K^{0.5}\widehat{S^*_{ij}}$. A similar treatment can be applied for the second model coefficient C_ϵ. In the present study, however, it is assumed that the dissipation coefficient C_ϵ=1.0 is employed for reasonable equilibrium, as suggested by Menon and Kim [46].

2.3 Numerical Solution Methods

As discussed in the previous section, the governing equations consist of partial differential equations (PDEs). Equation discretisation is the translation of the governing equations into a numerical analogue that can be solved by computer. In computational fluid dynamics (CFD), equation discretisation is usually performed by using the finite difference method (FDM), fhinite element method (FEM) or finite volume method (FVM).

The FDM employs the concept of Taylor expansion to solve the second-order partial differential equation in the governing equations of fluid flow. This method is straightforward, in which the derivatives of PDE are written in discrete quantities of variables, resulting in simultaneous algebraic equations with unknowns defined at the nodes of the mesh. FDM is famous for its simplicity and ease in obtaining higher order accuracy discretisation. However, FDM only applies to simple geometries because it employs a structured mesh.

Unlike FDM, an unstructured mesh is usually used in FEM. The computational domain is subdivided into a finite number of elements. Within each element, a certain number of nodes are defined where numerical values of the unknowns are determined. The discretisation is based on an integral formulation obtained using the method of weighted residuals, which approximates the solutions to a set of partial differential equations using interpolation functions. FEM is renowned for its application around complex geometries because of the application of an unstructured grid. But numerically, it requires higher computing power compared to FDM. So FVM, which is mathematically similar to FEM in certain applications, but requires less computer power, is the next consideration in CFD applications.

In FVM, the computational domain is separated into a finite number of elements known as control volumes. The governing equations of fluid flow are integrated and solved iteratively based on the conservation laws for each control volume. The discretisation process results in a set of algebraic equations that resolve the variables at a specified finite

number of points within the control volumes using an integration method. Through the integration on the control volumes, the flow around the domain can be fully modelled. FVM can be used for both the structured and unstructured meshes. Since this method involves direct integration, it is more efficient and easier to programme in terms of CFD code development. Hence, FVM is more common in recent CFD applications compared to both FEM and FDM.

In the present study, flow simulations are performed by using a solver built upon the open source code OpenFOAM (Weller et al. [55]), which is a collection of C++ libraries that are developed for the purpose of solving continuum mechanics problems with the finite volume discretisation procedure.

The purpose of this section is to describe the finite volume discretisation method used for solving the Navier-Stokes equations. Firstly, the discretisation approaches of the general transport equation are described for each term. This is followed by the discussion of the linear algebraic equations as well as the PISO algorithm. Finally, the boundary conditions and the moving grid method are briefly introduced.

2.3.1 Finite volume discretisation

From the previous section, the filtered Navier-Stokes equations for LES are given by:

$$\nabla\cdot\overline{\mathbf{u}} = 0, \tag{2.28}$$

$$\frac{\partial\overline{\mathbf{u}}}{\partial t} + \nabla\cdot(\overline{\mathbf{u}}\,\overline{\mathbf{u}}) = -\frac{1}{\rho}\nabla\overline{p} + \nabla\cdot\left[\nu\left(\nabla\overline{\mathbf{u}} + \nabla\overline{\mathbf{u}}^{T}\right)\right] + \nabla\cdot\tau, \tag{2.29}$$

where $\overline{\mathbf{u}}$ and $\overline{p}$ are the filtered velocity and pressure. ρ and ν are the fluid density and the kinematic viscosity. τ is the turbulence diffusion term which has to be modelled to close the system. In general, the effect of SGS turbulence on resolved scales is modelled as a turbulence viscosity ν_t and expressed within a single diffusion term together with molecular viscosity ν:

$$\begin{aligned}
&\nabla\cdot\left[\nu\left(\nabla\overline{\mathbf{u}} + \nabla\overline{\mathbf{u}}^{T}\right)\right] + \nabla\cdot\tau \\
&= \nabla\cdot\left[(\nu+\nu_t)\left(\nabla\overline{\mathbf{u}} + \nabla\overline{\mathbf{u}}^{T}\right)\right] \\
&= \nabla\cdot\left[\nu_{total}\left(\nabla\overline{\mathbf{u}} + \nabla\overline{\mathbf{u}}^{T}\right)\right],
\end{aligned} \tag{2.30}$$

In the FV approach, the Navier-Stokes equations are integrated over a control volume in time to transform the integral form of the governing equations:

$$\int_V \nabla\cdot\overline{\mathbf{u}}\,\mathrm{d}V = \int_s \mathrm{d}\mathbf{A}\cdot\overline{\mathbf{u}} = 0, \tag{2.31}$$

$$\int_{t-\Delta t}^{t}\left[\frac{\mathrm{d}}{\mathrm{d}t}\int_V \overline{\mathbf{u}}\,\mathrm{d}V + \int_V \nabla\cdot(\overline{\mathbf{u}}\,\overline{\mathbf{u}})\,\mathrm{d}V - \int_V \nabla\cdot\left[\nu_{total}\left(\nabla\overline{\mathbf{u}} + \nabla\overline{\mathbf{u}}^T\right)\right]\mathrm{d}V\right]\mathrm{d}t \tag{2.32}$$
$$= \int_{t-\Delta t}^{t}\left[\frac{1}{\rho}\int_V \nabla\overline{p}\,\mathrm{d}V\right]\mathrm{d}t,$$

where ν_{total} is the sum of the fluid kinematic viscosity ν and the SGS turbulent viscosity ν_t. s is the surface bounding the volume V and $\mathrm{d}\mathbf{A}$ is an infinitesimal surface with outward pointing normal on the surface f, as also shown in Figure 2.2. The momentum equation consists of temporal, convection, diffusion and source derivatives. Since the diffusion term includes a second derivative in the equation 2.32, the order of discretisation in each derivative term must be equal to or higher than the second-order level in order to obtain accuracy. Since each term should be discretised to yield second-order accuracy, the overall accuracy in the system should be second-order. All dependent variables are assumed to vary linearly around the calculated point and time.

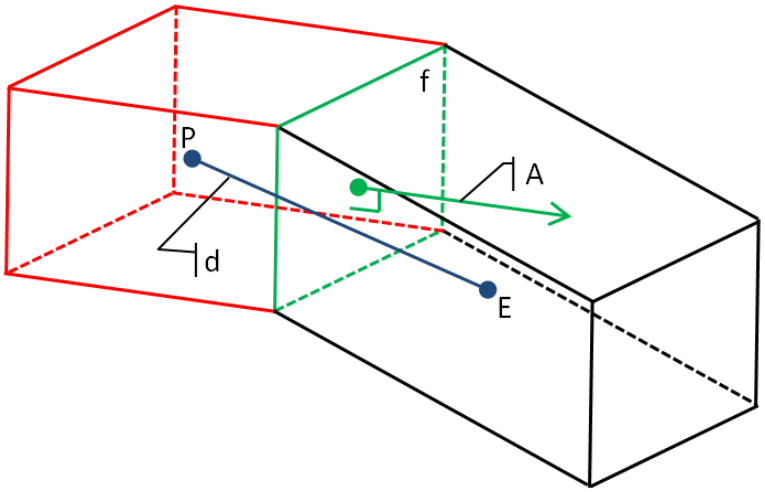

FIGURE 2.2: Two adjacent finite control volumes

2.3.2 Domain discretisation

In the staggered arrangement, the pressure and other scalar variables are stored at the centroids of the control volume (CV), while the velocities are stored at cell faces. On the other hand, when the collocated arrangement is used, all main variables such as velocity and pressure are stored in the centre, P or E, of the considered control volume, while some derived properties may be defined at the cell face f. Throughout this study, the collocated variable arrangement is adopted in structured mesh with a hexahedral cell. In an unsteady problem, the time domain is divided into a finite number of time steps Δt and a solution is obtained by marching Δt from an initial condition.

2.3.3 Discretisation of convection term

Taking into account the dependent variable ϕ in the general transportation equations, the convection term can be written according to the Gauss theorem as:

$$\int_V \nabla\cdot(\overline{\mathbf{u}}\phi)\ \mathrm{d}V = \int_f (n\cdot\overline{\mathbf{u}}\phi)\ \mathrm{d}f, \tag{2.33}$$

where V is the control volume and n is the unit vector normal to the surface (f) of the volume and directed outward from the volume. The surface integral can be split into a sum of integrals over each of the faces bounding the control volume:

$$\int_f (n\cdot\overline{\mathbf{u}}\phi)\ \mathrm{d}s \approx \sum_f (n\cdot\overline{\mathbf{u}}_f)\,\phi_f f = \sum_f (\mathbf{A}\cdot\overline{\mathbf{u}}_f)\,\phi_f = \sum_f F\phi_f, \tag{2.34}$$

where $\mathbf{A}$ is the surface area vector pointing outward and F is the convective flux at the face. The convective flux derived from the velocity field must satisfy the FV continuity equation.

A transported quantity at a face f is evaluated from a simple interpolation between values at P and the adjacent cell centre E with the interpolation factor α:

$$\phi_f = \alpha\phi_P + (1-\alpha)\,\phi_E, \tag{2.35}$$

$$\alpha = \overline{fE}/d, \tag{2.36}$$

In Navier-Stokes equations, the momentum convection term $\nabla\cdot(\overline{\mathbf{u}}\,\overline{\mathbf{u}})$ introduces quadratic non-linearity and must be linearised by replacing one of the filtered velocities with the filtered velocity from the previous iteration $(n-1)$:

$$\int_V \nabla\cdot(\overline{\mathbf{u}}\,\overline{\mathbf{u}})\,\mathrm{d}V = \sum_f (\mathbf{A}\cdot\overline{\mathbf{u}}_f)\,\overline{\mathbf{u}}_f$$

$$\approx \sum_f \left(\mathbf{A}\cdot\overline{\mathbf{u}}_f^{n-1}\right)\overline{\mathbf{u}}_f^{n} = \sum_f F^{n-1}\cdot\overline{\mathbf{u}}_f^{n}, \tag{2.37}$$

To evaluate $\overline{\mathbf{u}}_f$ at the CV face centre, linear variation of the dependent variable is assumed. Linear interpolation is the simplest second-order approximation and denoted as a central difference (CD) scheme. As discussed in the previous section, the main function of a SGS model is to estimate a proper amount of dissipation in turbulence. In the central difference scheme, it is noted that any numerical dissipation is not generated in contrast to other schemes such as the upwind scheme or γ scheme blended with the CD and upwind schemes. However, it is known that the second-order CD scheme in LES might cause numerical instability in the solution for convection-dominated problems, which violates the boundedness of the solution. In the present study, a 2nd order CD scheme is used in order to obtain a more accurate solution; however, it is required to employ a very small time step Δt to overcome the boundedness problem.

2.3.4 Discretisation of diffusion term

Using a similar approach to the one for the convection term, the diffusion term in the general transport equation can be discretised as:

$$\int_V \nabla\cdot(\Gamma\nabla\phi)\,\mathrm{d}V = \int_f n\cdot(\Gamma\nabla\phi)\,\mathrm{d}f$$

$$\approx \sum_f n\,f\cdot(\Gamma\nabla\phi_f) = \sum_f \Gamma\mathbf{A}\cdot(\nabla\phi_f)\,, \tag{2.38}$$

The face gradient of ϕ can be evaluated using a central difference approximation provided the grid is orthogonal, and the vectors $\mathbf{d}$ and $\mathbf{A}$ are parallel:

$$\mathbf{A}\cdot(\nabla\phi_f) \approx \mathbf{A}\,\frac{\phi_E-\phi_P}{|\mathbf{d}|}, \tag{2.39}$$

In case of a non-orthogonal grid, the deferred correction approach is used as follows:

$$\mathbf{A} \cdot (\nabla \phi_f) \approx \mathbf{A_d} \frac{\phi_E - \phi_P}{|\mathbf{d}|} + \mathbf{A}_\Delta \cdot (\nabla \phi_{old}), \tag{2.40}$$

Where, the vector component $\mathbf{A_d}$ is calculated from:

$$\mathbf{A_d} = \frac{\mathbf{d}}{\mathbf{d} \cdot \mathbf{A}} |\mathbf{A}|^2, \tag{2.41}$$

The second term in the right hand side of the equation is evaluated explicitly using values from the previous iteration and should satisfy the equality, $\mathbf{A} = \mathbf{A}_d + \mathbf{A}_\Delta$.

The diffusion term for the Navier-Stokes equations in the finite volume approach is given by:

$$\begin{aligned} &\int_V \nabla \cdot \left[\nu_{total} \left(\nabla \overline{\mathbf{u}} + \nabla \overline{\mathbf{u}}^T \right) \right] \mathrm{d}V \\ &\approx \sum_f \left(\nu_{total} \right)_f \mathbf{A} \cdot \left(\nabla \overline{\mathbf{u}} \right)_f + \nabla \cdot \left[\nu_{total} \left(\nabla \overline{\mathbf{u}}^{n-1} \right)^T \right] V \end{aligned} \tag{2.42}$$

The gradient and transposed gradient term are generally discretised separately and the transposed velocity gradient term is calculated at the cell centre by the velocity calculated in the previous time step.

2.3.5 Discretisation of transient term

Integrating all the terms over time results in:

$$\int_{t-\Delta t}^{t} \frac{\partial}{\partial t} \int_V \phi \, \mathrm{d}V = \int_{t-\Delta t}^{t} \left[- \int_V \nabla \cdot (\overline{\mathbf{u}} \, \phi) \, \mathrm{d}V + \int_V \nabla \cdot (\Gamma \nabla \phi) \, \mathrm{d}V + \int_V S_\phi \, \mathrm{d}V \right] \mathrm{d}t, \tag{2.43}$$

To simplify the equation, $H = \overline{\mathbf{u}} \, \phi - \Gamma \nabla \phi$ is defined:

$$\int_{t-\Delta t}^{t} \frac{\partial}{\partial t} \int_V \phi_i \, \mathrm{d}V \, \mathrm{d}t = - \int_{t-\Delta t}^{t} \int_V \nabla \cdot H_i \, \mathrm{d}V \, \mathrm{d}t + \int_{t-\Delta t}^{t} \int_V S_\phi \, \mathrm{d}V \, \mathrm{d}t, \tag{2.44}$$

or

$$\int_{t-\Delta t}^{t} \frac{\partial \phi_i}{\partial t} V \, \mathrm{d}t = - \int_{t-\Delta t}^{t} \sum_f \mathbf{A} \cdot H_i \, \mathrm{d}t + \int_{t-\Delta t}^{t} \left(S_u + S_p \phi_p \right) V \, \mathrm{d}t, \tag{2.45}$$

In the present study, the backward differencing (BD) scheme is employed. The temporal discretisation for BD scheme uses three time levels to achieve second-order accuracy. The

temporal derivative with a fully implicit second-order accuracy is given as:

$$\frac{\partial \phi}{\partial t} = \frac{\frac{3}{2}\phi^{n} - 2\phi^{n-1} + \frac{1}{2}\phi^{n-2}}{\Delta t}, \tag{2.46}$$

The final form of the equation becomes:

$$\frac{\frac{3}{2}\phi^{n} - 2\phi^{n-1} + \frac{1}{2}\phi^{n-2}}{\Delta t} V = -\sum_{f} \mathbf{A} \cdot H_i + (S_u + S_p \phi_p)\, V, \tag{2.47}$$

Jasak [56] discussed that the BD scheme results in a truncation error four times larger than that in the well known Crank-Nicholson method. This error can be considered as an additional diffusion and might produce undesirable results in LES as the SGS diffusion may be very small and thus the error can exceed the SGS diffusion. To keep stability throughout the simulation, the cell face Courant Number, also referred to as the Courant-Friedrichs-Lewy (CFL) condition, should be set below 1.0 at least:

$$\mathrm{CFL} = \frac{\overline{\mathbf{u}}_f \cdot n}{|d|}, \tag{2.48}$$

In LES, the time step tends to be very small, resulting in a small temporal diffusion error.

2.3.6 Solution method of Navier-Stokes equations

In the present study, the well-known pressure implicit with splitting of operators (PISO) algorithm is used, which was proposed by Issa [57]. The brief introduction of the pressure equation will be presented here as more details can be found in standard textbooks of computational fluid dynamics. A pressure correction equation is used to couple pressure and velocity and is derived from momentum equation. The corrected pressure can be obtained by the mass conservation equation. The pressure equation is defined as:

$$\overline{\mathbf{u}}_p = \frac{\mathbf{H}}{a_p} - \frac{\nabla \overline{p}}{a_p}, \tag{2.49}$$

where

$$\nabla \overline{p} = \sum_{f} \mathbf{A} \cdot \overline{p}_f, \tag{2.50}$$

where a_p is a set of coefficients depending on $\overline{u}_p$ from convection, diffusion and transient term. $\mathbf{H}$ is the combination of the coefficient matrix consisting of all terms except the pressure gradient. In the PISO process, a tentative velocity $\overline{\mathbf{u}}_p$ in the pressure equation is predicted by the guessed or initial pressure and does not generally satisfy the mass conservation. Thus, new pressure should be re-calculated with updated $\mathbf{H}$.

The pressure gradient term remains undiscretised and it allows face interpolation of the coefficients. So, the face velocity $\overline{\mathbf{u}}_f$ is expressed by interpolating $\overline{\mathbf{u}}_p$:

$$\overline{\mathbf{u}}_f = \left(\frac{\mathbf{H}}{a_p}\right)_f - \left(\frac{\nabla \overline{p}}{a_p}\right)_f, \tag{2.51}$$

The face velocity $\overline{\mathbf{u}}_f$ must satisfy the continuity equation to solve the pressure equation:

$$\nabla \cdot \overline{\mathbf{u}}_f = \sum_f \mathbf{A} \cdot \overline{\mathbf{u}}_f = \sum_f \mathbf{A} \cdot \left(\frac{\mathbf{H}}{a_p}\right)_f - \sum_f \mathbf{A} \cdot \left(\frac{\nabla \overline{p}}{a_p}\right)_f = 0, \tag{2.52}$$

The PISO procedure within one time step with respect to the solution method of the linear algebraic equations to solve the discretised equations is briefly described below:

1. With initial condition for the unknown flow variables $\overline{\mathbf{u}}, \overline{p}, \nu_t, F$, turbulent properties are first updated.

2. The momentum equation predicts new velocities $\overline{\mathbf{u}}^*$ using the guessed pressure: momentum will be conserved, mass will not be conserved. The solution matrix is calculated by the biconjugate gradient method applicable to handle both symmetric and asymmetric matrices with the diagonal incomplete-LU decomposition to accelerate convergence time.

3. With updated $\mathbf{H}$ by the predicted velocities $\overline{\mathbf{u}}^*$, new pressure $\overline{p}^*$ is solved from the pressure correction equation: mass will be conserved, momentum will not be conserved. Due to the explicit nature of the non-orthogonal component of the face interpolation of $\overline{p}$, the pressure equation has to be solved iteratively. de Villiers [58] noted that a single or at most two corrector steps are sufficient to converge the non-orthogonal component. The matrix for the pressure equation is calculated by the conjugate gradient method applicable to symmetric matrices. The geometric

algebraic multi-grid solver is used as a preconditioner to improve computational time.

4. Finally, the velocities $\overline{\mathbf{u}}^{**}$ and the fluxes are updated by the pressure $\overline{p}^{*}$. The PISO loop in step 3-4 is repeated iteratively until the dependent variables stop changing. The loop corrector generally requires more than 2 iterations. In the LES study, it is known that two correctors are sufficient to achieve the quantities since the time step is quite small.

2.3.7 Boundary conditions

Inlet and outlet boundaries

The uniform velocity $\overline{\mathbf{u}}=U(x,y,z)$ is applied without a disturbance level and a zero gradient boundary condition for pressure, meaning the normal gradient of pressure is zero, used at inlet boundaries.

Jasak [56] indicated that the outlet boundary condition should specify that the overall mass balance for the computational domain is satisfied. At outlet boundaries, therefore, the fixed value boundary condition is used for pressure, $\overline{p}=p_{out}$, and a zero gradient boundary condition for velocity is applied. Overall mass conservation is guaranteed by the pressure equation.

Periodic boundary

Periodic boundaries at the ends of a cylinder axis in the spanwise direction are employed to approximate infinite homogeneous directions. This is accomplished by linking the coupled cell pair at the ends of the axis.

Impermeable no-slip boundary

As the velocity of the fluid on cylinder wall is equal to that of the wall and the flux through the wall is zero, the constant velocity $\overline{\mathbf{u}}=U(0,0,0)$ and zero gradient condition for pressure are imposed on the cylinder wall respectively.

2.3.8 Moving grid method

In order to calculate the predefined cylinder oscillation as explained in Equation 1.1, a deforming or moving computational grid is used in the present study. The computational grid is adjusted according to the prescribed motion which is updated in every time step.

The gird points on the cylinder wall are calculated according to the prescribed sinusoidal motion of the cylinder and the resulting mesh deformation is determined by solving the Laplace equation with the distance-based diffusion parameter γ from Jasak and Tuković [59]:

$$\nabla\cdot(\gamma\nabla\mathbf{u}) = 0, \tag{2.53}$$

Where $\mathbf{u}$ is the point velocity used to modify the point position from old to new:

$$\mathrm{x}_{new} = \mathrm{x}_{old} + \mathbf{u}\Delta t, \tag{2.54}$$

The boundary conditions for the motion equation are enforced to the known boundary motion.

In order to maintain the internal mesh quality near the cylinder wall region, three different diffusion parameters are tested based on cell centre distance to a specified distance l:

- Case-1: Constant distance-based γ=l
- Case-2: Linear distance-based γ=$\frac{1}{l}$
- Case-3: Quadratic distance-based γ=$\frac{1}{l^2}$

As shown in Figure 2.3 Case-1 shows unsatisfactory mesh quality around the cylinder wall region. However, Case-2 and 3 improve the overall quality as well as mesh spacing around the cylinder. Based on the grid motion along y/D, the most robust results are obtained by quadratic distance-based γ in Case-3. Therefore the moving mesh with quadratic γ is employed in the present study.

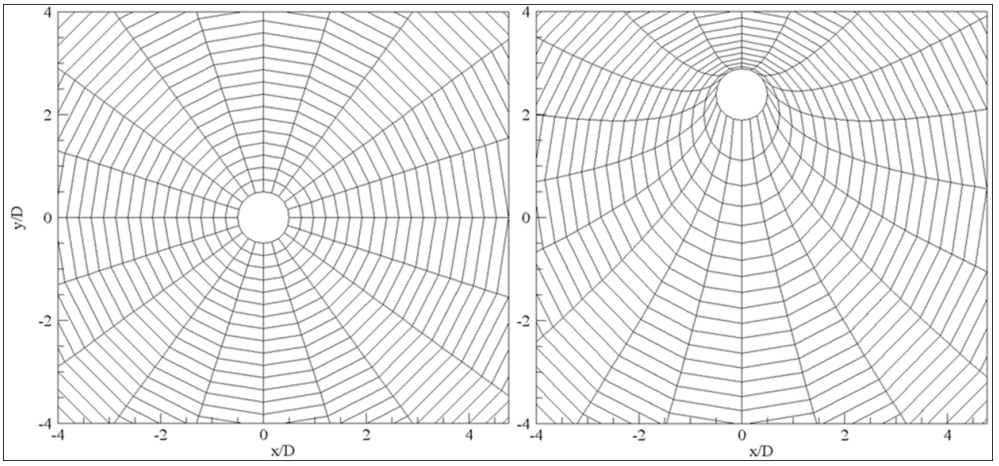

(a) Case-1: constant.

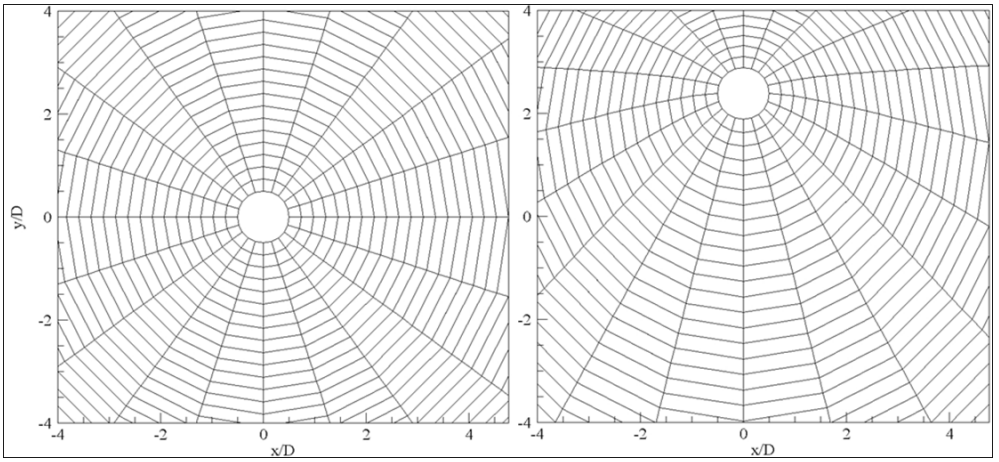

(b) Case-2: linear.

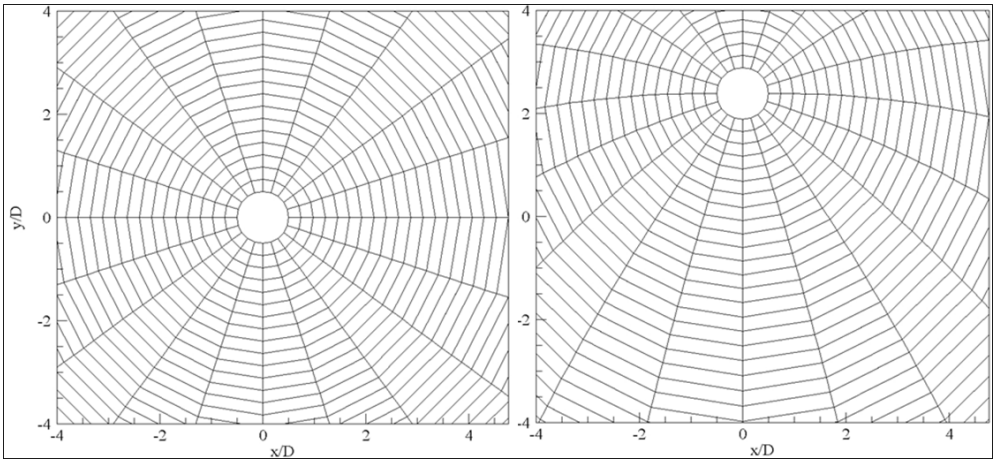

(c) Case-3: quadratic.

FIGURE 2.3: Influence of diffusivity on mesh quality before (left column) and after (right column) grid motion: In all cases the high amplitude ratio for test purposes is applied in the cylinder transverse oscillation in the crossflow direction.

2.4 Closure

In this Chapter, the principles of LES and the governing equations were presented. The classical filtering operation and the energy spectrum were briefly reviewed and three different subgrid scale models, namely the conventional Smagorinsky, k-equation and dynamic k-equation, were described. The implementation of the algebraic SGS models, which is adopted in the present study, was discussed in detail.

The discretisation approach for the governing equations was discussed for each term with particular focus on the use of the 2nd order central difference scheme for convection terms in the LES technique. A brief introduction was also provided for the PISO algorithm with a linear algebraic equation and the boundary conditions. Finally, the moving mesh method was examined for internal grid quality, especially near the wall region. The test indicated that the cylinder oscillation is well-approximated by the moving mesh method with a quadratic distance factor.

Chapter 3

VERIFICATION AND VALIDATION OF 3-D LES COMPUTATION

The near wake of a circular cylinder becomes particularly complex when transition occurs in the separating shear layers. Based on literature review, the patterns of the near wake between Re=1000 and 10000 are representative of transition phenomenon in the separating shear layers. Moreover, Norberg [2] reported that large-scale phase dislocation of vortices along the span is experimentally observed at Re≈5000 and also shear-layer instability has just started to dominate wake transition at Re≈5500. At Re=10000, pronounced small-scale concentration of vorticity is evident in shear layers shortly after separation and large-scale vortices are formed very close to the base of the cylinder. Dong and Karniadakis [42] noted that these variations, as the Reynolds number increases, have important consequences for both the steady and unsteady loading on the cylinder. Moreover, the variation of Reynolds number also influences the shear-layer instability significantly. In the present investigation, therefore, a range of Reynolds numbers of 5500, 10000 and 41300, as a challenging test case, are selected to examine the variation of the turbulent wake.

The purpose of this Chapter is to verify and validate the 3-D numerical simulation of turbulent flow behind a circular cylinder at such challenging flow conditions. The Reynolds number based on the free-stream velocity U and the cylinder diameter D is

ranging from Re=5500-41300, where the shear-layer instability in the intermediate sub-critical flow regime (TrSL3) is fully developing, as discussed in Chapter 1. In addition, the numerical data, especially from 3-D LES at higher Reynolds number of Re≥4000, are rare in literature. Therefore, the mean or time-averaged flow statistics at considered Reynolds numbers are produced in order to gain more data from 3-D LES computation.

In the initial section of this Chapter, the 3-D simulation domain is presented in detail. Then, the modelling and numerical aspects such as grid independence and SGS modelling, which influence the quality of LES solutions, are examined in terms of main wake parameters at each Reynolds number. All parameters such as hydrodynamic forces are validated with experimental data, as a basis of a complete validation of 3-D LES simulation. Furthermore, the flow statistical quantities such as mean velocity and Reynolds stress fields are graphically addressed for all Reynolds numbers. The flow fields are, of course, temporally and spatially averaged in the homogeneous spanwise z-direction. Finally, at Re=41300, the mean flow statistics at certain points around the cylinder are compared to experiments in order to examine SGS modelling effects. In addition, the characteristic flow patterns of mean and spanwise-averaged flow statistics are discussed and compared to experiments for validation.

3.1 Computational Domain

Figure 3.1 shows the 3-D solution domain used in the present study. The cylinder axis is aligned with the spanwise direction z-axis and the x-axis is along the streamwise direction. The y-axis is in a crossflow direction and orthogonal to the cylinder axis. A body-fitted and O-type structured grid is generated, which is widely used in the numerical simulations of the cylinder flow problem, e.g. see Lu and Dalton [10] and Breuer [37].

The geometric size of the computational domain is carefully determined based on previous successful numerical simulations of cylinder flow, e.g. Atluri et al. [43]. The outer boundary 15 cylinder diameters $15D$ from the cylinder centre is chosen as the width in the present study. It is noted that the computational domain should have a width of 10 diameters in the transverse direction to avoid blockage as discussed in Al-Jamal et al. [60]. Therefore, the radial distance of $15D$ is also what is required to prevent

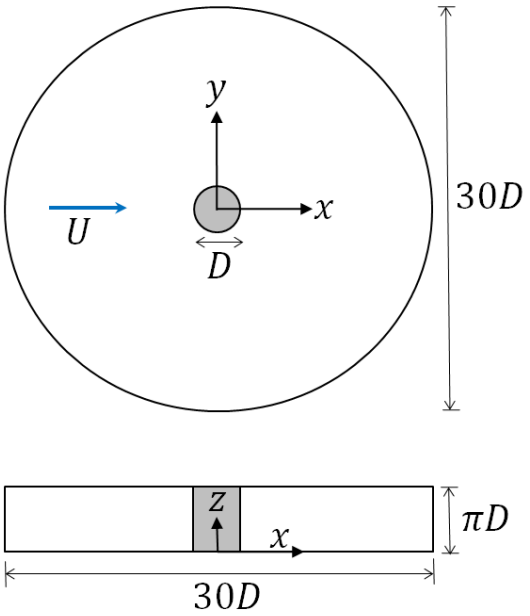

FIGURE 3.1: Physical configuration of the computational domain for a stationary cylinder: the cylinder is coloured in gray.

blockage effects. The advantage of this size of computational domain is to have a finer grid system without an increase in the number of mesh points. This approach allows the LES method to be more representative of turbulence around the cylinder.

In order to predict the 3-D nature of cylinder flow along the spanwise direction correctly, the cylinder aspect ratio $L_z/D{=}\pi$ is chosen as minimal based on careful previous 3-D LES studies of spanwise effects on cylinder flow conducted by Breuer [32] and Labbé and Wilson [15]. The prediction of main wake parameters obtained in the present domain size is validated with experimental data in the following section.

The hexahedral grid in the x-y plane is exponentially stretched in the radial direction r and is uniformly spaced in the circumferential direction θ as shown in Figure 3.2. The mesh is, therefore, highly clustered towards the cylinder surface so that maximum y^+ remained around the unit throughout the whole simulation time for a stationary cylinder.

Uniform flow U is imposed at the inflow without the disturbance level. The Neumann conditions are imposed at the outlet boundary. Periodic boundary conditions are employed at the spanwise ends of the cylinder to avoid the end wall effect. The no-slip wall conditions are imposed along the cylinder surface.

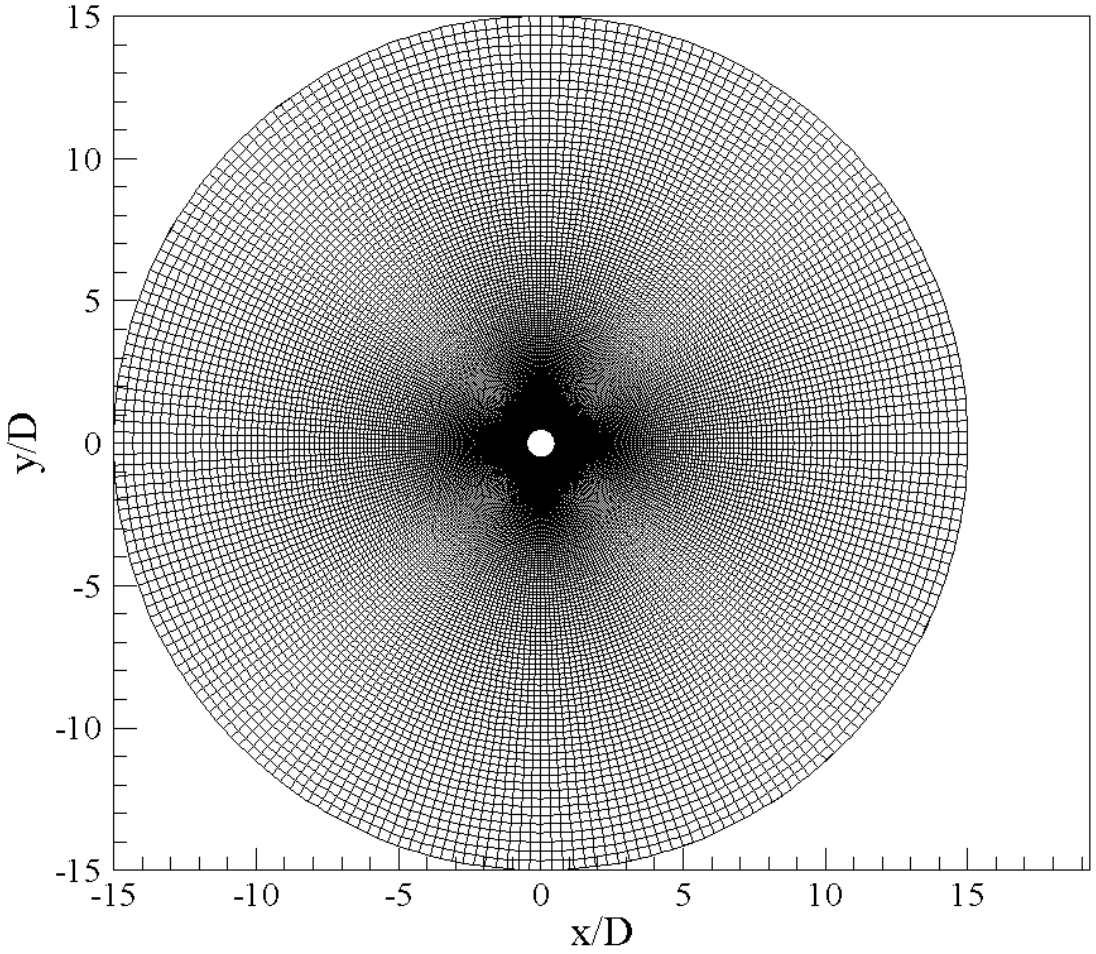

(a) 2-D slice of computational domain.

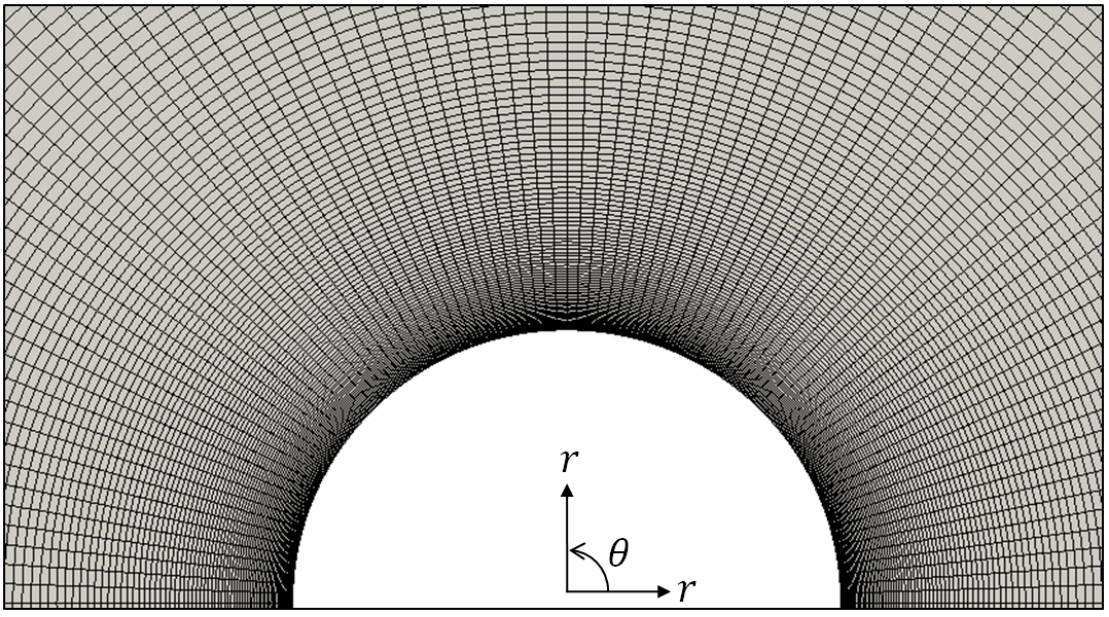

(b) Closer view of the grid in the vicinity of the half cylinder.

FIGURE 3.2: 2-D slice of grid in x-y plane.

The governing equations are advanced in time using a second-order implicit backward scheme and the spatial terms are discretised using the second-order central differencing as discussed in the previous Chapter. The pressure-velocity coupling is achieved by the PISO algorithm, using a predictor-corrector approach for the time discretisation of the momentum equation while enforcing the continuity equation.

3.2 Turbulent Flow at Re=5500

In order to demonstrate the fact that the predicted results are independent of the grid density, grid sensitivity is carefully examined in terms of global hydrodynamic coefficients and the results are compared with measurement data at considered Reynolds numbers.

To obtain a close approximation of hydrodynamic forces, the numerical and modelling aspects influencing the quality of LES solutions are extensively investigated at Re=5500. The strong impact of three-dimensionality and the important aspect of the numerical scheme for the convective fluxs are presented as well.

3.2.1 Grid sensitivity and hydrodynamic coefficients

The 3-D, turbulent, unsteady flow around the cylinder is modelled in the frame of the LES approach using the classical time-dependent filtered Navier-Stokes equations. For the turbulent flow at Re=5500, the algebraic Smagorinsky SGS model with the model coefficient of C_s=0.1 is employed together with the Van driest wall damping model to evaluate the flow field for all simulation cases, as discussed in previous section 2.2.2.

The grid resolution is evaluated in terms of global or main wake parameters as a basis of comparison with experimental results for a complete validation of the 3-D LES simulation. The constant non-dimensional time step of $\Delta tU/D$=0.002 is used to maintain numerical stability at Re=5500. The flow data are gathered over a non-dimensional time of at least $100U/D$, corresponding to approximately 21 vortex shedding cycles, to obtain converged flow data. The CPU time generally ranges from about 180 to 300 hours with 108 processors in parallel as the grid resolution increases.

The simulations are performed with different grid resolutions both in the x-y planes and in the spanwise z-direction. Table 3.1 summarises the main wake parameters together

TABLE 3.1: Grid sensitivity and main wake parameters for a stationary cylinder at Re=5500: the Smagorinsky model is used in all simulations.

Case and grid resolution ($r\times\theta\times z$)	St	$\bar{C}_D$	C'_L
N_z=64[1]			
LES-A1 ($160\times160\times64$)	0.215	1.056	0.266 [23%][2]
LES-A2 ($180\times180\times64$)	0.215	1.107	0.341 [57%]
LES-A3 ($200\times200\times64$)	0.215	1.009	0.183 [-16%]
LES-A4 ($240\times240\times64$)	0.215	1.042	0.233 [7%]
N_z=96			
LES-B1 ($140\times140\times96$)	0.205	1.161	0.391 [80%]
LES-B2 ($160\times160\times96$)	0.215	1.082	0.309 [42%]
LES-B3 ($180\times180\times96$)	0.215	1.048	0.243 [12%]
LES-B4 ($200\times200\times96$)	0.210	1.027	0.219 [1%]
Experimental data			
Norberg [2] at Re=5500	0.206[3]	-	0.217[3]
Norberg [2] at Re=5000-6100	0.209	-	0.15-0.27
Khalak and Williamson [61] at Re=5500	-	1.05-1.10	-
3-D LES result			
Doolan [62] at Re=5500	0.209	1.08	0.273

[1] N_z is the number of grid points, which are evenly distributed in the spanwise z-direction.
[2] All percentage values in lift are calculated based on the empirical value of 0.217.
[3] Obtained from empirical correlation suggested by Norberg [2].

with available experimental data. The Strouhal number St=$f_K D/U$ and the averaged drag coefficient $\bar{C}_D$ are generally in good agreements with the experimental data for all grid resolutions. Theses quantities are generally weakly dependent on the grid resolution. However, the root-mean-square of the lift coefficient C'_L shows a higher sensitivity to the resolution.

In the case of N_z=64 (LES-A1 to A4), C'_L demonstrates relatively large fluctuations as mesh resolution in x-y plane increases gradually. It is possible for LES-A4, showing a good agreement with the empirical value, to have potential numerical errors. Therefore, more fine resolution in x-y plane to obtain grid convergence is required to correctly predict C'_L in the case of N_z=64 for this study.

On the other hand, with the high resolution mesh in the spanwise direction N_z=96 (LES-B1 to B4), the values of lift coefficients sharply decrease to the empirical value as mesh resolution in x-y plane increases gradually. The lift values of LES-B3 and B4 with high resolution in the spanwise direction reasonably fall within ~10% of the empirical value suggested by Norberg [2] and also within the range of experimentally measured

values between Re=5000 and 6100. Therefore, the best results are achieved by LES-B3 as a minimum grid size and LES-B4.

The empirical solutions suggested by Norberg [2] for the Strouhal and r.m.s. lift values by considering the reported values for a number of experiments are formulated as:

$$\mathrm{St} \approx 0.1853 + 0.0261 \times \exp\left[-0.9 \times \log\left(\frac{\mathrm{Re}}{1.6 \times 10^3}\right)^{-2.3}\right], \tag{3.1}$$

$$\text{where}, 1.6 \times 10^3 \leq \mathrm{Re} \leq 1.5 \times 10^5,$$

$$C_L' \approx 0.52 - 0.06 \times \log\left(\frac{\mathrm{Re}}{1.6 \times 10^3}\right)^{-2.6}, \tag{3.2}$$

$$\text{where}, 5.4 \times 10^3 \leq \mathrm{Re} \leq 2.2 \times 10^5,$$

At Re=5500, these empirical formulae produce the Strouhal and lift levels of 0.206 and 0.217 respectively.

Figure 3.3 shows the time history of the force coefficient and power spectrum of the lift for LES-B3. The time traces present the behaviour of the drag and lift coefficients with irregular amplitudes over non-dimensional time of $100U/D$. A simple method of calculating the Strouhal number is to divide a known number of periods of the lift

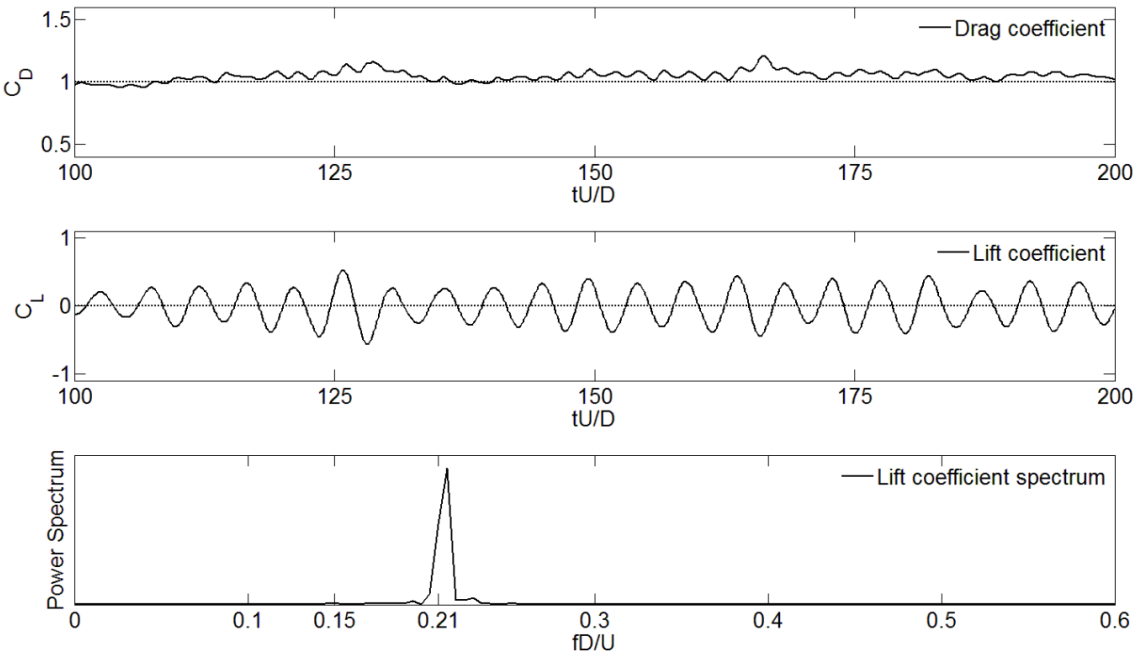

FIGURE 3.3: Time history of force coefficient and power spectrum of lift coefficient at Re=5500 (LES-B3).

TABLE 3.2: Main wake parameters for a stationary cylinder at Re=5500.

Case and grid resolution ($r\times\theta\times z$)	St	$\bar{C}_D$	C'_L
LES-C1 $(200\times200\times64)$[1]	0.205	1.051	0.313
LES-D1 $(180\times180\times64)$[2]	0.210	1.235	0.513
LES-D2 (180×180)[2,3]	0.240	1.559	1.264

[1] Smagorinsky model and second-order total variational diminishing (TVD) scheme used for convection term used.
[2] No SGS model used for turbulence modelling.
[3] 2-D simulation without SGS model.

coefficient by the time length over which they occur. Such a method, although simple, is rather inaccurate. In this study fast Fourier transform (FFT) is employed to obtain Strouhal number as the lift coefficient is recorded at regular time steps. Since the FFT method is textbook material, its details will not be presented here.

In Table 3.2 the influence of the numerical scheme of the convective term is additionally evaluated by using the bounded second-order total variational diminishing (TVD) scheme for sub-critical cylinder flow. For this purpose two simulations, LES-A3 and C1, could be compared based on the same grid resolution with the Smagorinsky type model with C_s=0.1. The result of LES-C1 based on TVD shows that C'_L is about 71% larger than LES-A3. This observation is consistent with the high level of numerical dissipation for the class of TVD schemes.

LES-D1 without the turbulence model shows the largest $\bar{C}_D$ and C'_L of all 3-D solutions. Applying the turbulence model to LES-A2 with the same grid size of LES-D1 to dissipate resolved turbulent fluctuations results in highly improved values. In order to show the necessity for 3-D computation for the present study, a 2-D simulation (LES-D2) was carried out and the result is compared to LES-D1. The large deviations of all quantities between 2-D and 3-D simulations show that three-dimensional wake structures of cylinder flow strongly influence the main wake parameters.

The mean pressure coefficient C_p distribution on the cylinder surface is examined and compared to reference experimental data at various Reynolds numbers in Figure 3.4. The angle θ was measured clockwise from the stagnation point. The pressure distribution at Re=5500 (LES-B3) shows overall agreement with experimental data between reference Reynolds numbers. After the point where the slope of the C_p curve changes ($\approx71^\circ$), the behaviour of the pressure coefficient on the cylinder surface tends to be similar with the curve at Re=3900 when compared to those at Re=3000 and 8000.

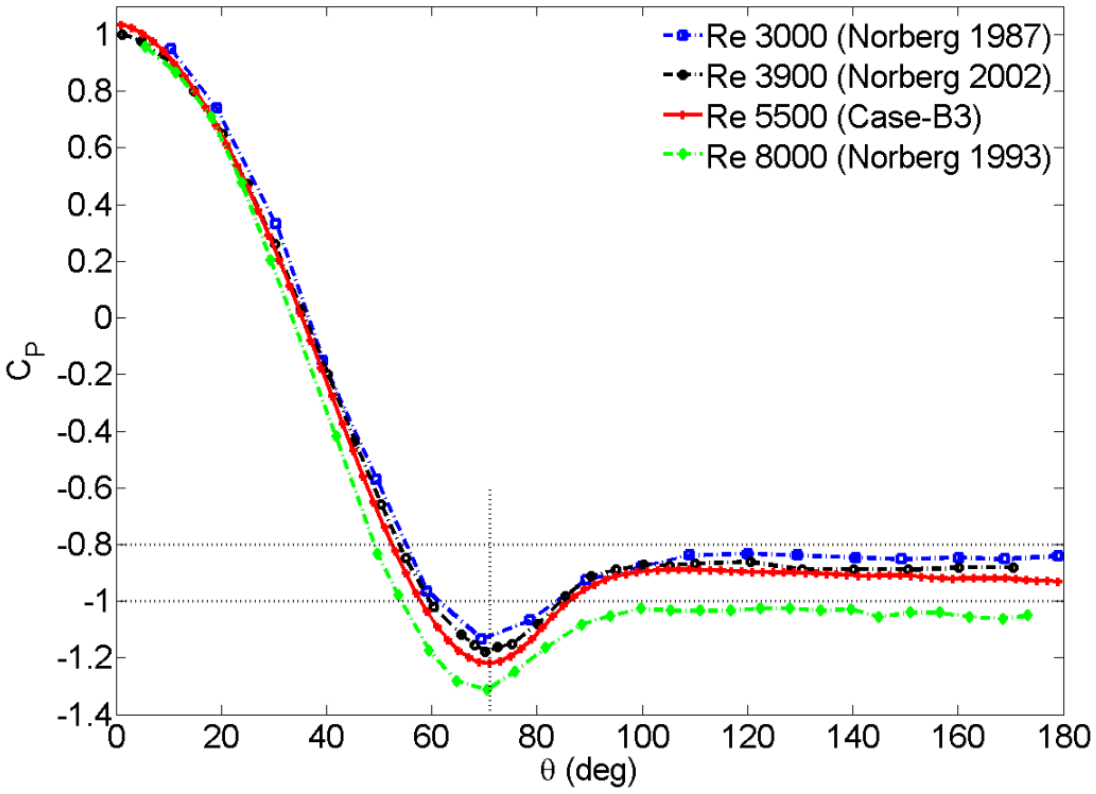

FIGURE 3.4: Comparison of pressure coefficients on the half cylinder surface at Re=5500 (LES-B3) and experimental data at Re=3000-8000: the angle is measured clockwise from the stagnation point of the cylinder.

The base pressure coefficient C_{pb} is critical to the computation because this parameter strongly correlates with the large-scale vortex formation length, shedding frequency, and spanwise vorticity of the Kármán vortices as well as the cylinder aspect ratio as discussed in Jordan [36] and Norberg [63]. In this study, the base pressure coefficient C_{pb}=-0.93 obtained in LES-B3 shows a fairly good agreement with the experimental value of $C_{pb}\approx$-0.95 at Re=5500, measured by Norberg [63]. Therefore, these good agreements of the fluid forces and pressure on the cylinder as shown in this section indicate that LES-B3 should provide sufficiently converged solutions for the objective of the present study.

Figure 3.5 shows general features of instantaneous vorticity field at Re=5500 obtained in LES-B3. The large-scale finger-like streamwise vortices along the z-axis in the cylinder axis direction are shown in Figure 3.5(left). Small-scale streamwise vortices, which are developing inside the upper shear layer at x/D=0.625 in y-z plane, are captured. The evolution of the small-scale secondary vortex pairs in high resolution grid of N_z=96 displays a characteristic shape.

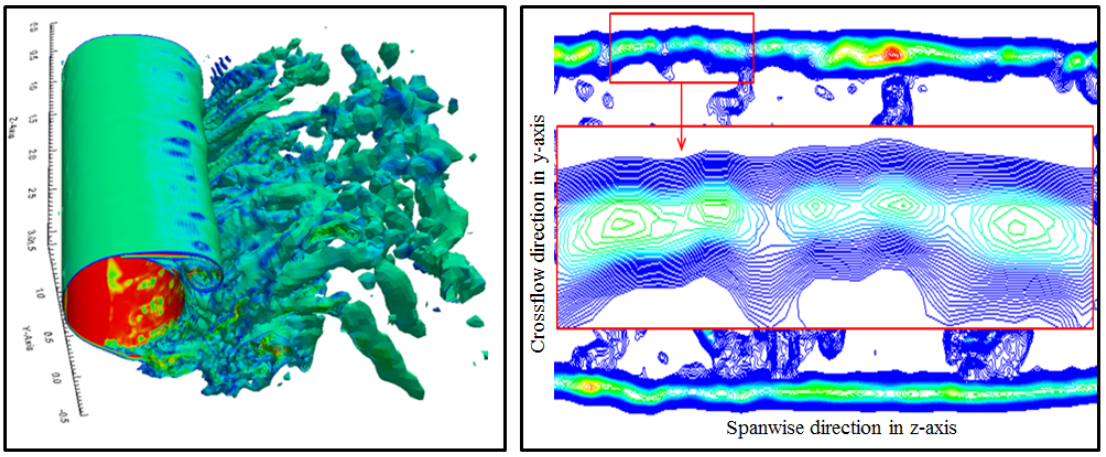

FIGURE 3.5: Perspective view of the cylinder flow in terms of iso-surface of vorticity at Re=5500 (LES-B3), showing large-scale finger-like streamwise vortices (left) and small-scale streamwise vortices pairs inside the thin shear layer along the high-resolution spanwise direction (right).

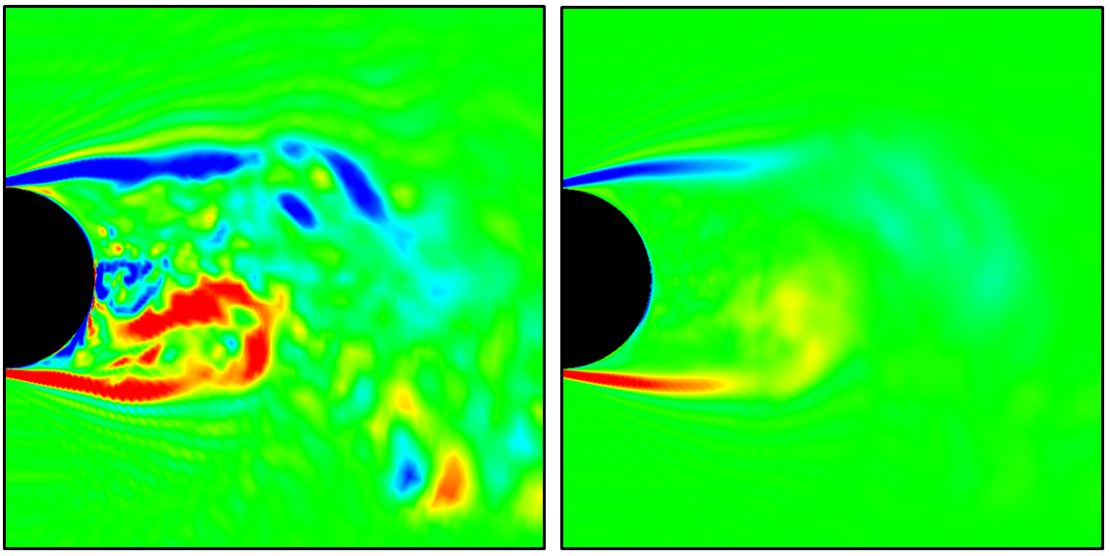

FIGURE 3.6: Instantaneous vorticity field obtained in the spanwise mid-section (left) and spanwise-averaged vorticity field (right) at tU/D=190 (LES-B3): In both plots the level is -8<ω_z<8.

In the present study the spanwise-averaged field is often used in order to make comparisons with experimental data. Figure 3.6 shows the difference between instantaneous vorticity obtained in the spanwise mid-section to the left, which is generally used as a representative flow in 3-D simulation, and the spanwise-averaged field to the right. The spanwise-averaging process clearly indicates that main flow features remain in the field, but the instantaneous effect along the spanwise direction is discarded. It is noted that both figures have the same contour level for comparison purposes.

3.2.2 Mean flow statistics at Re=5500

The components of mean velocity and Reynolds stresses are computed from LES-B3 with 3.11M cells at considered Reynolds number, as discussed in the previous section. The flow data are averaged temporally and spatially in the spanwise direction.

In Figure 3.7(a), normalised mean velocity u/U field is shown in the spanwise mid-section $L_z/D{=}\pi/2$, where u, v, w are mean velocity components in x-, y-, z-direction. It is noted that tail of the velocity is extended up to $x/D{\approx}2.0$ from the cylinder centre in this flow regime.

The normalised mean velocity fields in each direction as shown in Figure 3.7(b,c,d) are spanwise-averaged and clearly display characteristic patterns of the flow fields. The pattern of the negative velocity bubble behind the cylinder in a downstream direction

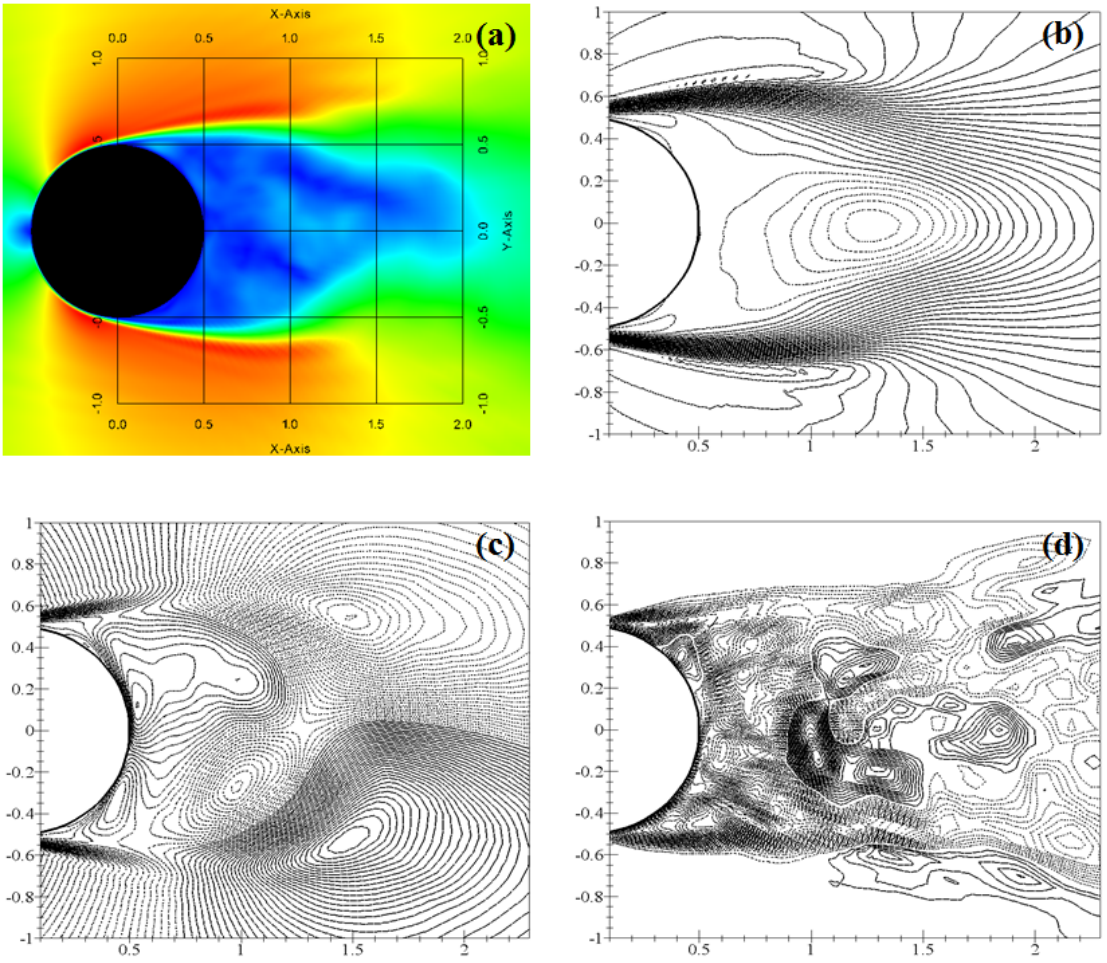

FIGURE 3.7: Normalised mean velocity fields at Re=5500: Instantaneous normalised velocity fields u/U obtained in spanwise mid-section (a); Spanwise-averaged normalised velocity fields u/U (b), v/U (c) and w/U (d).

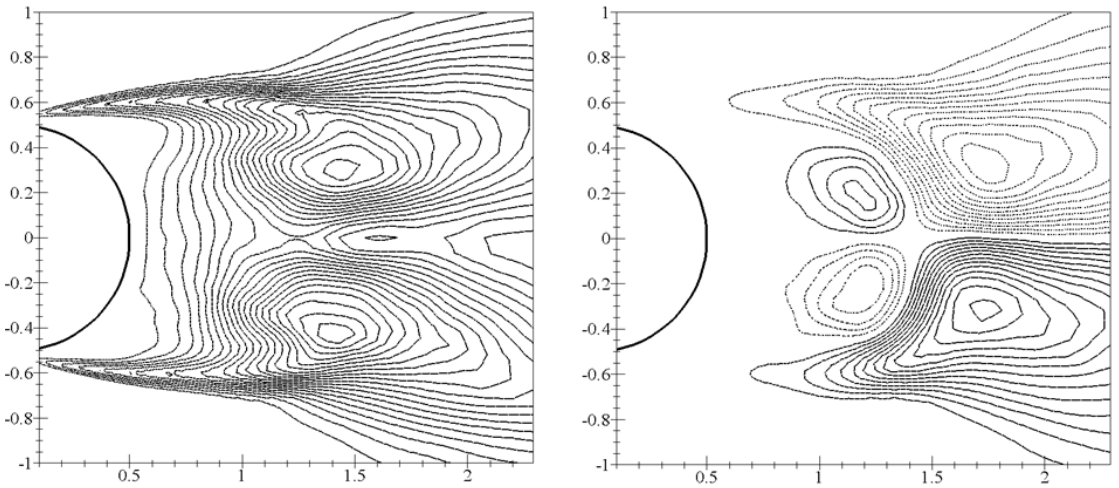

(a) $u'u'/U^2$ (left) and $u'v'/U^2$ (right).

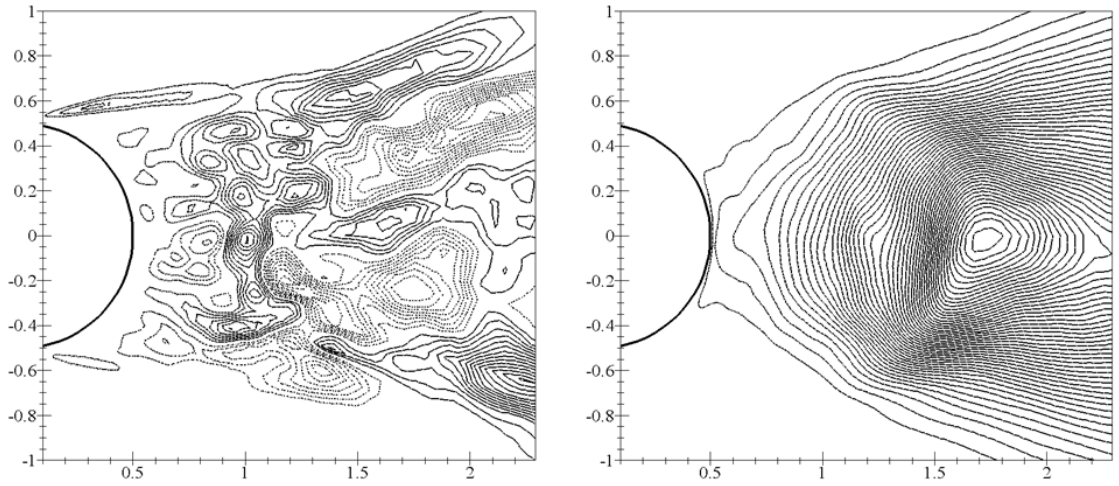

(b) $u'w'/U^2$ (left) and $v'v'/U^2$ (right).

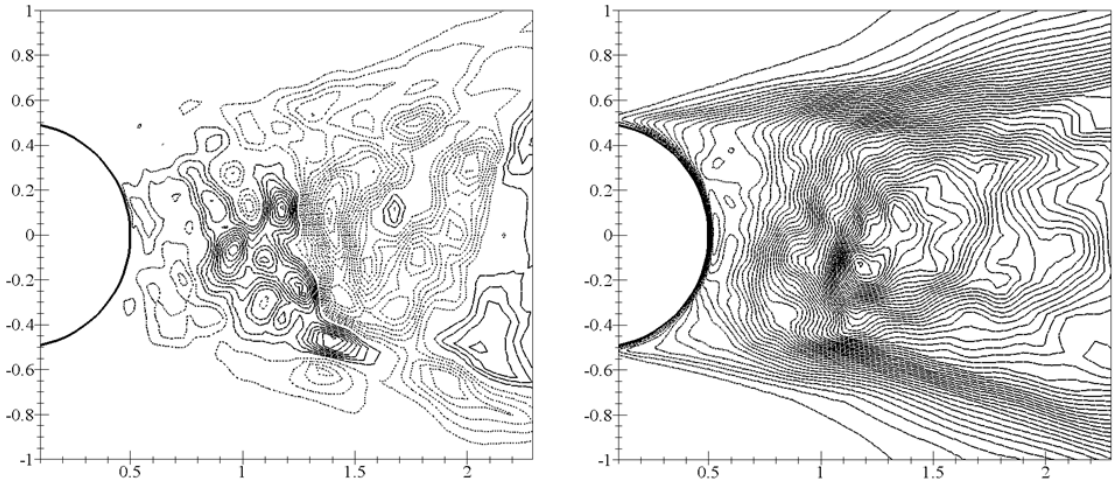

(c) $v'w'/U^2$ (left) and $w'w'/U^2$ (right).

FIGURE 3.8: Spanwise-averaged normalised Reynolds stresses fields in turbulence wake at Re=5500.

TABLE 3.3: Details of the mean flow fields at Re=5500.

Flow fields	Contour levels	Max./Min.
Velocity fields		
u/U	-0.300$\leq u/U \leq$1.400, $\Delta u/U$=0.05	-0.336
v/U	-0.820$\leq v/U \leq$0.820, $\Delta v/U$=0.010	$\pm$0.336
w/U	-0.072$\leq w/U \leq$0.048, $\Delta w/U$=0.002	-0.071
Reynolds stress fields		
$u'u'/U^2$	0.020$\leq u'u'/U^2 \leq$0.220, $\Delta u'u'/U^2$=0.010	0.23
$u'v'/U^2$	-0.120$\leq u'v'/U^2 \leq$0.130, $\Delta u'v'/U^2$=0.010	$\pm$0.13
$u'w'/U^2$	-0.014$\leq u'w'/U^2 \leq$0.016, $\Delta u'w'/U^2$=0.001	0.016
$v'v'/U^2$	0.020$\leq v'v'/U^2 \leq$0.490, $\Delta v'v'/U^2$=0.010	0.498
$v'w'/U^2$	-0.013$\leq v'w'/U^2 \leq$0.012, $\Delta v'w'/U^2$=0.001	0.012
$w'w'/U^2$	0.002$\leq w'w'/U^2 \leq$0.102, $\Delta w'w'/U^2$=0.002	0.103

base is clearly shown in the u/U field. The strong fluctuations in crossflow direction are visible at the ends of shear layers in Figure 3.7(c) and the magnitude is indicated as $\pm$0.85 in the mean transverse velocity. The details of the plots are summarised in Table 3.3.

In Figure 3.8 turbulence flow statistics of Reynolds stresses behind the stationary cylinder are calculated to provide quantitative simulation results and the flow statistics are computed by averaging the flow temporally and spatially along the homogeneous spanwise direction as well.

Figure 3.8(a-left) shows strong fluctuations in the separating shear layers and two maxima of $\pm$0.22 in turbulence, which are comparable to those in the mean transverse velocity, where u', v', w' are mean fluctuations or r.m.s velocity components in each direction.

The shear stress $u'v'$ displays four distinct distributions behind in Figure 3.8(a-right) and it is also noted that the patterns are formed at a substantial distance downstream of the cylinder base at Re=5500. Figure 3.8(b,c) shows the other components of Reynolds stress fields including spanwise velocity fluctuation w'.

3.3 Turbulent Flow at Re=10000

3.3.1 Grid sensitivity and hydrodynamic coefficients

In order to demonstrate that the computational results are independent of grid density at the more higher Reynolds number of 10000, simulations are performed on the five different mesh sizes in conjunction with the Smagorinsky (SMG hereafter), k-equation (TKE hereafter) and dynamic k-equation (DTKE hereafter) SGS models.

A constant non-dimensional time step $\Delta tU/D$=0.001 is comparable to those in Re=5500, in order to satisfy the temporal resolution requirement of LES. The simulations are performed using 112 processors in parallel, allowing efficient computations on the multi-processor cluster. In general, the CPU time for each simulation case of the stationary cylinder is approximately 200h.

The grid sensitivity and main wake parameters of the stationary cylinder are presented in Table 3.4 and Table 3.5 respectively and the resulting values are compared to available LES, DNS and experimental data at the same Reynolds number. It is noted that the number of grid in the spanwise z-direction N_z is chosen as 64 in all simulation cases. For a quantitative validation, the flow is sampled over at least 25 vortex shedding cycles for the stationary cylinder flow.

Simulations are performed with five different grid resolutions by varying the number of grid points in x-y planes in Table 3.4. The Strouhal number and drag force do not change significantly as the mesh resolution increases, showing 4% and 5% differences between LES-A1 and A5. On the other hand, the r.m.s. lift coefficient C'_L exhibits a somewhat higher fluctuations in the lower grid resolutions (LES-A1 to A3). However, the predicted values from two consecutive cases (LES-A4 and A5) agree well with each other

TABLE 3.4: Grid sensitivity for the stationary cylinder at Re=10000

Simulation cases	Resolutions (million cells)	SGS models	St	$\bar{C}_D$	C'_L	Relative[1] change
LES-A1	1.63 M	SMG	0.216	1.153	0.448	-
LES-A2	2.07 M	SMG	0.216	1.115	0.383	-17.0%
LES-A3	2.56 M	SMG	0.216	1.144	0.424	9.7%
LES-A4	3.09 M	SMG	0.208	1.104	0.356	-19.1%
LES-A5	3.68 M	SMG	0.208	1.101	0.346	-2.9%

[1] The relative change of r.m.s. lift coefficient between two consecutive grid resolutions.

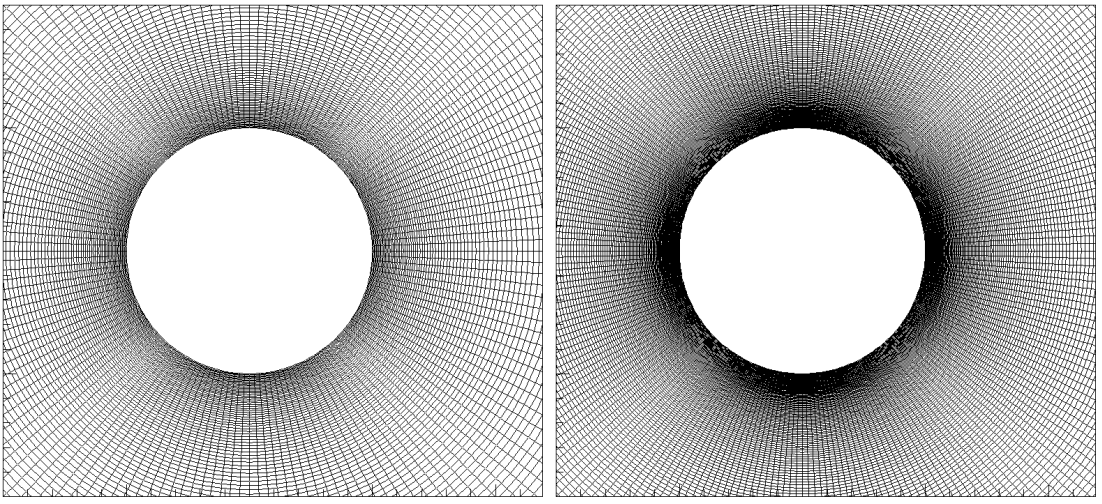

(a) Coarse grid of LES-A1 with 1.63 M cells. (b) Fine grid of LES-A5 with 3.68 M cells.

FIGURE 3.9: Zoom of the grid in the vicinity of the cylinder.

within 3% for the lift coefficient. Thus, Table 3.4 clearly indicated that grid resolution of 3M minimum is required for this flow regime. Figure 3.9 displays the zoom of grid resolutions around the cylinder in the cases of LES-A1 and A5. However, the levels of the force coefficients with SMG on the finest mesh are significantly under-predicted compared to the empirical lift value of 0.411.

In Table 3.5 an additional two simulation cases are examined on the finest grid (3.68M) with TKE and DTKE SGS models in order to obtain close approximations of the hydrodynamic forces. The force coefficients from LES-B5 with TKE show fairly good agreements with the DNS data as well as the empirical value. The predicted drag and lift coefficients from LES-B5 show the differences of 0.5% and 2.2% compared to the

TABLE 3.5: Main wake parameters for the stationary cylinder at Re=10000

Simulation cases	Resolutions (million cells)	SGS models	St	$\bar{C}_D$	C'_L	Relative[1] change
LES-A5	3.68 M	SMG	0.208	1.101	0.346	-16.0%
LES-B5	3.68 M	TKE	0.208	1.149	0.420	2.1%
LES-C5	3.68 M	DTKE	0.208	1.292	0.605	46.9%
3-D simulations at Re=10000:						
LES, Wornom et al. [38]			0.20	1.22	0.476	
DNS, Dong and Karniadakis [42]			0.203	1.143	0.448	
Experiments at Re=10000:						
Empirical formula, Norberg [2]			0.201	-	0.411	
Experiment, Gopalkrishnan [30]			0.193	1.186	0.384	

[1] The ratio of the r.m.s. lift coefficient on the empirical value.

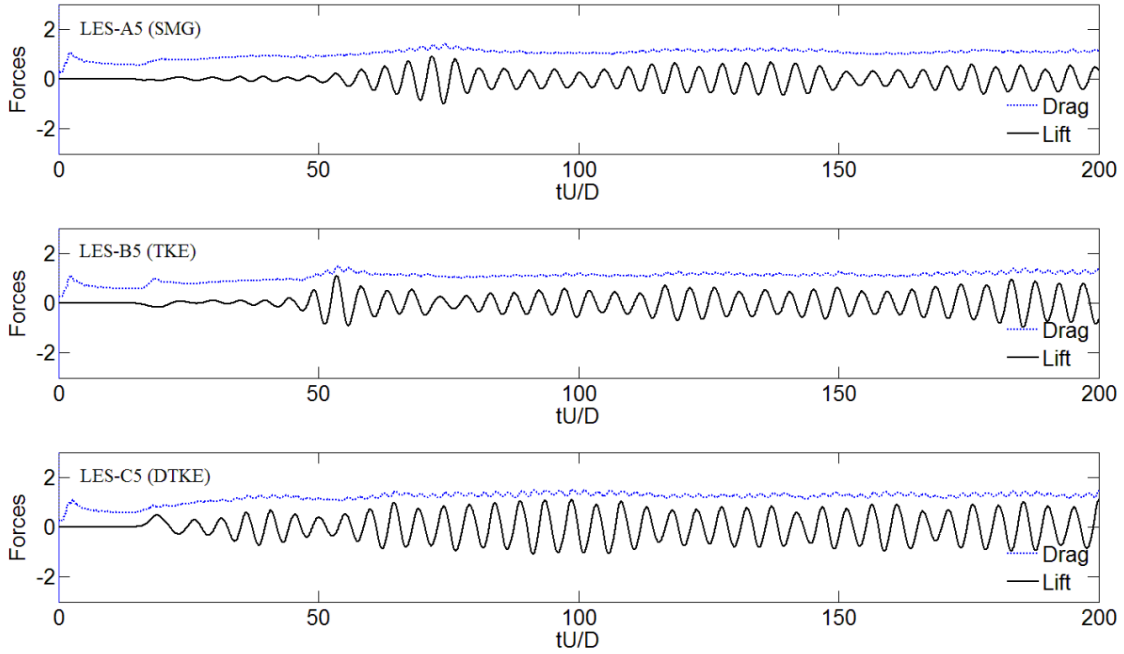

FIGURE 3.10: Time histories of force coefficients with different SGS models at Re=10000.

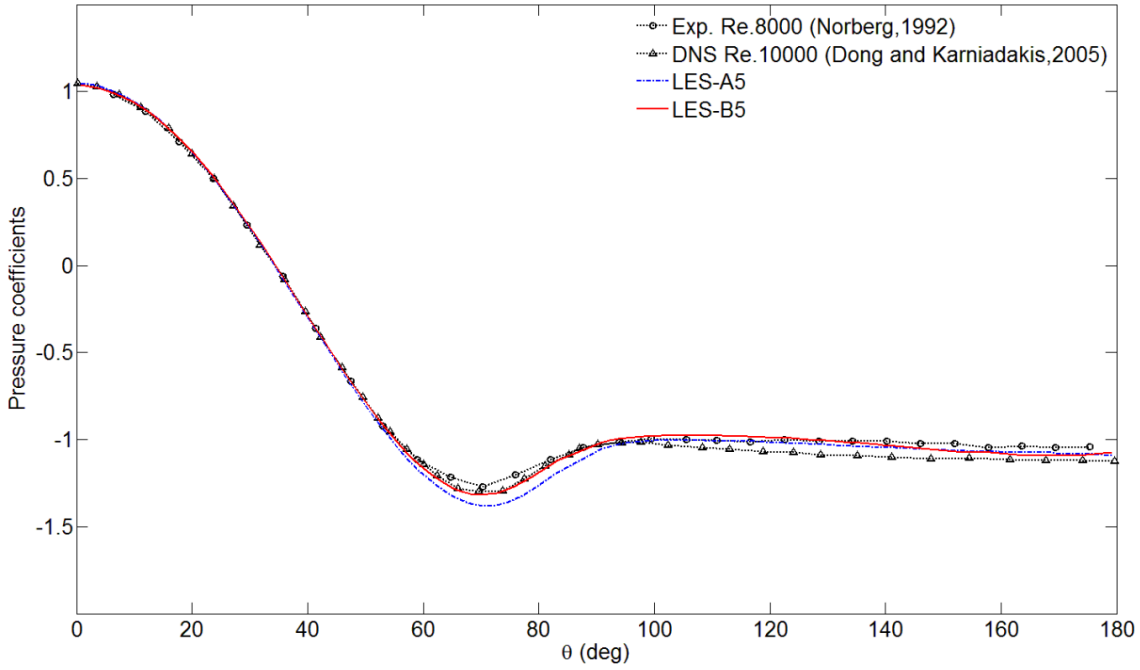

FIGURE 3.11: Mean pressure coefficient C_p distribution on the cylinder surface at Re=10000 (LES-A5 and LES-B5).

DNS and the empirical value respectively. However, the lift value from LES-C5 is highly over-estimated as about 47%. Therefore, the results from TKE on the finest resolution grid seem to be in good agreement with the reference data at Re=10000. The time histories of the force coefficients obtained with different SGS models are displayed in

Figure 3.10.

In Figure 3.11 the mean pressure coefficient C_p distribution over the cylinder, which is measured clockwise from the stagnation point, is examined for LES-A5 and B5 on the same grid resolution with 3.68 M cells. Although LES-A5 shows overall agreements with the reference data, the pressure around the point where the slope of C_p curve changes is slightly over-predicted. The pressure distribution on the entire cylinder surface calculated from LES-B5 shows much better agreement with the reference data.

3.3.2 Mean flow statistics at Re=10000

At a higher Reynolds number of 10000, mean flow statistics are computed from LES-B5 with 3.68 M cells. The resulting data are time- and spanwise-averaged as well.

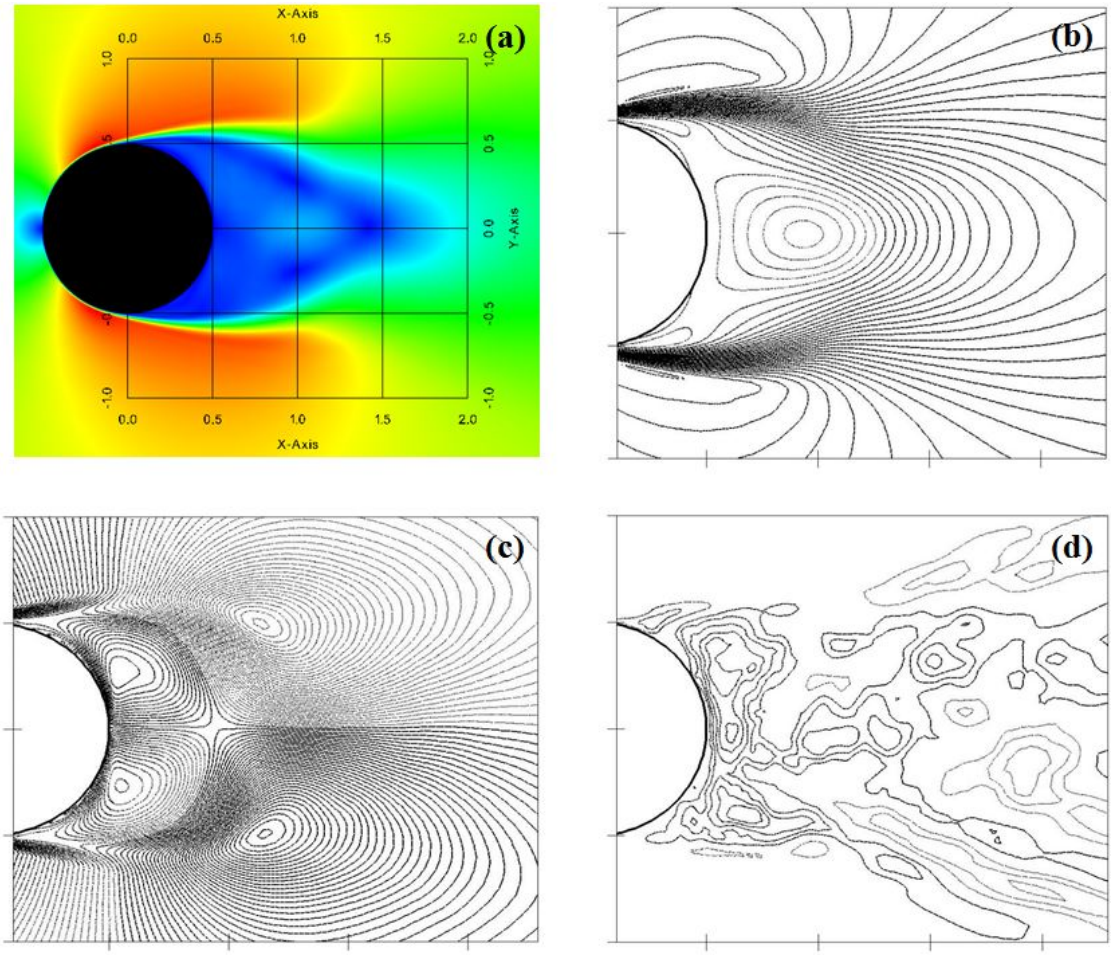

FIGURE 3.12: Normalised mean velocity fields at Re=10000: Instantaneous normalised velocity fields u/U obtained in spanwise mid-section (a); Spanwise-averaged normalised velocity fields u/U (b), v/U (c) and w/U (d).

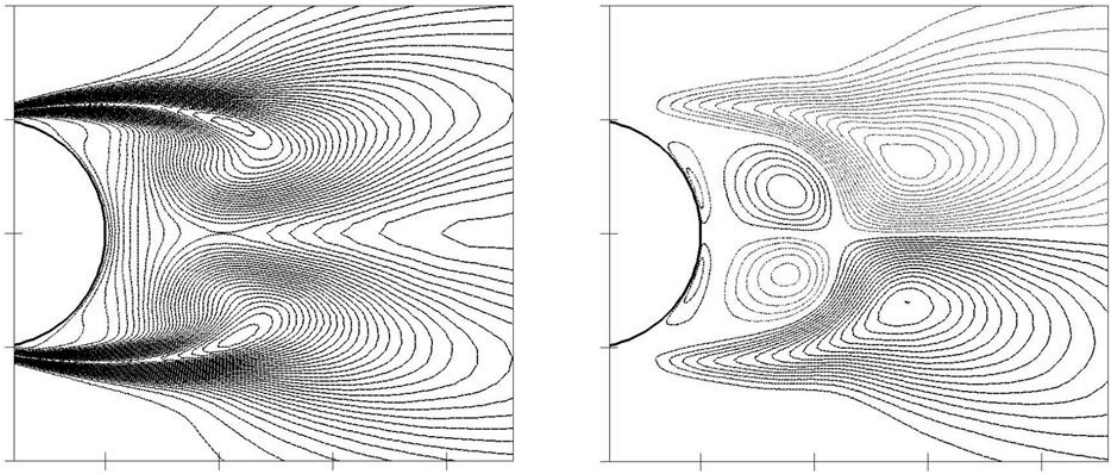

(a) $u'u'/U^2$ (left) and $u'v'/U^2$ (right).

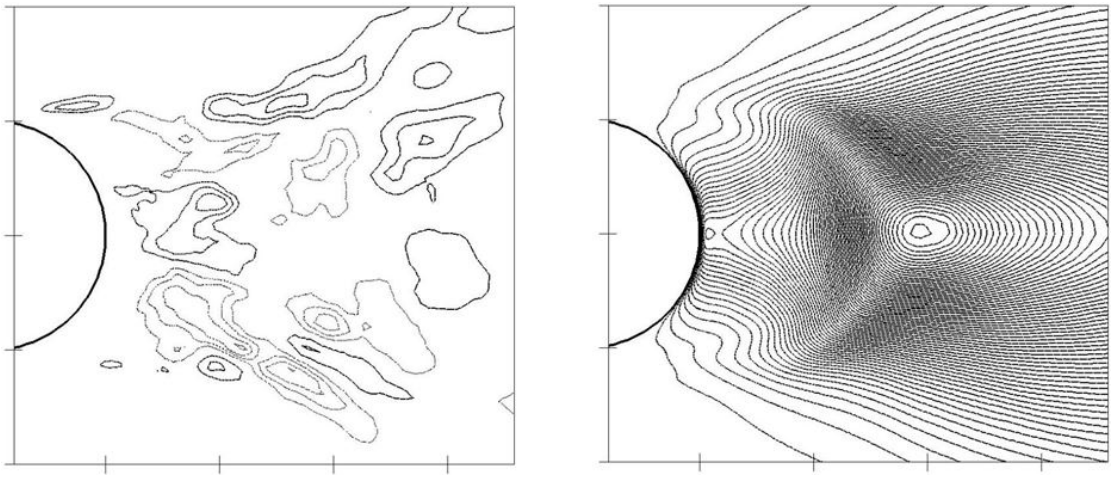

(b) $u'w'/U^2$ (left) and $v'v'/U^2$ (right).

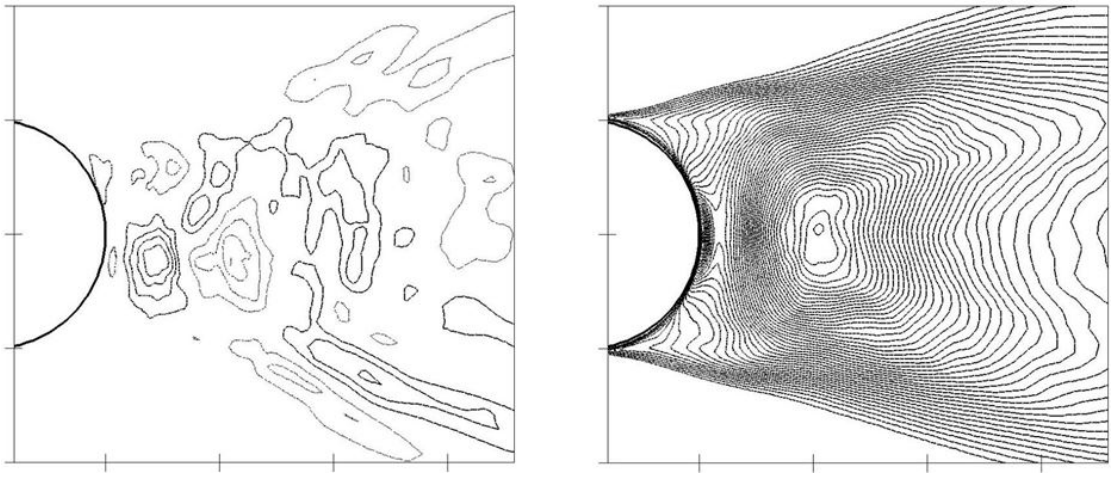

(c) $v'w'/U^2$ (left) and $w'w'/U^2$ (right).

FIGURE 3.13: Spanwise-averaged normalised Reynolds stresses fields in turbulence wake at Re=10000.

TABLE 3.6: Details of the mean flow fields at Re=10000.

Flow fields	Contour levels	Max./Min.
Velocity fields		
u/U	-0.250$\leq u/U \leq$1.400, $\Delta u/U$=0.050	-0.260
v/U	-0.850$\leq v/U \leq$0.850, $\Delta v/U$=0.010	$\pm$0.85
w/U	-0.010$\leq w/U \leq$0.010, $\Delta w/U$=0.002	-0.011
Reynolds stress fields		
$u'u'/U^2$	0.010$\leq u'u'/U^2 \leq$0.330, $\Delta u'u'/U^2$=0.010	0.33
$u'v'/U^2$	-0.170$\leq u'v'/U^2 \leq$0.170, $\Delta u'v'/U^2$=0.010	$\pm$0.17
$u'w'/U^2$	-0.004$\leq u'w'/U^2 \leq$0.004, $\Delta u'w'/U^2$=0.001	0.004
$v'v'/U^2$	0.010$\leq v'v'/U^2 \leq$0.660, $\Delta v'v'/U^2$=0.010	0.663
$v'w'/U^2$	-0.004$\leq v'w'/U^2 \leq$0.004, $\Delta v'w'/U^2$=0.001	0.004
$w'w'/U^2$	0.001$\leq w'w'/U^2 \leq$0.096, $\Delta w'w'/U^2$=0.002	0.096

In Figure 3.12(a,b), the tail of normalised mean velocity u/U field and the reverse velocity in u/U are seem to be reached more closely to the cylinder base compared with those at Re=5500. The details of the plots are summarised in Table 3.6.

In Figure 3.13 turbulence flow statistics of Reynolds stresses behind the stationary cylinder are calculated and general patterns of these fluctuations are similar to those at Re=5500 as expected. However, it seems that the locations of peak values especially in $u'u'/U^2$ and $u'v'/U^2$ move substantially close to the cylinder base as the Reynolds number increases.

Therefore, comparison study of the flow statistics, i.e. u/U, $u'u'/U^2$ and $u'v'/U^2$, will be conducted at Re=5500-10000 in great detail and the Reynolds number effect is discussed in terms of near-wake structures in the next Chapter.

3.4 Turbulent Flow at Re=41300

Breuer [32] indicated that the importance of the subgrid scale model significantly increased for higher Reynolds numbers in comparison with lower Reynolds number cases. As discussed in previous sections, the turbulent flow at Re=5500 was reasonably well-predicted by using the conventional Smagorinsky eddy-viscosity type model. However, in the case of the higher Reynolds number of 10000, the main wake parameters including lift were significantly under-estimated from the conventional model. Instead, the predicted results from the algebraic k-equation SGS model shows fairly good agreement with experimental measurements.

In this section, the turbulent flow at Re=41300 is examined with particular focus on the effect of subgrid scale model on the high-Re flow. Computations are carried out using 96 cores in parallel on 24 Intel Xeon Phi (2.6 GHz CPU, 4 GB of memory). Total ∼15 days of CPU time are required in order to compile over 30 vortex shedding cycles for each simulation case at Re=41300.

3.4.1 Grid sensitivity and hydrodynamic coefficients

A grid convergence study is performed on three sets of grids with 4.3M to 5.7M cells and the k-equation SGS model (TKE) without the wall model is used for grid refinement study. Table 3.7 shows the values of several physical quantities under three different grid resolutions. The gird resolution is gradually increased in the x-y plane, while the number of grid in the spanwise z-direction is kept as N_Z=64.

In Table 3.7, the values of Strouhal number are identical as the grid resolution increased from Grid-A to C. The differences between two consecutive Grid-A and B are 3.7% and 11.9% in drag and lift respectively. The relative changes of the force coefficients between Grid-B and C indicate minor differences as 1.1% and 1.6% respectively. In order to satisfy the spatial resolution at Re=41300, it is concluded that grid resolution with 5M cells is required as minimum resolution. Therefore, all the results presented in the following sections are obtained from the high-resolution Grid-C with 5.7M cells.

3.4.2 SGS modelling effect on hydrodynamic coefficients

For investigation of the effect of the SGS model in terms of main wake parameters, three different models, k-equation (TKE), Smagorinsky (SMG) and dynamic k-equation (DKTE), are implemented on Grid-C.

TABLE 3.7: Grid dependence analysis at Re=41300.

Grid	L_z	Average y^+	Total cells[1]	SGS model	St	$\bar{C}_D$	C'_L
A	πD	≈0.5	4,326,400	TKE[2]	0.200	1.432	0.834
B	πD	≈0.5	5,017,600	TKE	0.200	1.485	0.937
C	πD	≈0.5	5,760,000	TKE	0.200	1.502	0.948

[1] The control volume along the spanwise direction is evenly distributed as N_Z=64 in all simulation cases.
[2] For grid convergence study, the k-equation SGS model (TKE) is used with no wall damping approach.

TABLE 3.8: Main wake parameters with different SGS models on Grid-C (5.7M cells).

Cases at Re.41300	St	$\bar{C}_D$	C'_L	$-C_{pb}$
C1: TKE	0.200	1.502	0.948	1.658
C2: TKE+WM[1]	0.200	1.297	0.738	1.418
C3: SMG+WM	0.200	1.225	0.596	1.373
C4: DTKE+WM	0.200	1.195	0.531	1.244
Experiments by Ünal and Atlar [64]	0.186	1.14	-	-
Experiments by Norberg [2, 63]	0.189	-	0.496	≈1.2
2-D RANS-WKO by Ünal et al. [65]	0.193	0.951	0.240	-
3-D RANS-WKO by Ünal and Gören [66]	0.193	0.956	0.235	0.980

[1] +WM indicates use of the wall modelling approach.

In Table 3.8 the computed main wake parameters are listed together with both experimental data and numerical results from RANS with the Wilcox k-ω (WKO) turbulence model at Re=41300, where $-C_{pb}$ is the mean pressure coefficient. The presence of the wall modelling in each simulation set is marked as +WM after the name of the corresponding SGS model.

Case-C1 without wall modelling shows the highest over-prediction of force and pressure coefficients. Lift values are estimated as nearly two times compared to empirical result suggested by Norberg [2]. Applying the wall model (C2) results in slightly improved values, but it seems that TKE without the wall approach is not sufficient to predict accurate hydrodynamic forces as well as back pressure.

The importance of SGS modelling is clearly demonstrated in Case-C2 to C4. The relative difference on the lift coefficient between Case-C2 and C3 is about 19.2%, while the lift values in C2 and C3 are highly over-estimated as 32.8% and 16.8% compared to the experiment. The results obtained with the dynamic model (C4) shows better agreement with experimental values. In Case-C4 the Strouhal number and force coefficients are slightly over-estimated as about 5-6%, whereas the pressure coefficient shows a fairly good agreement with the experiment.

In the cases of 2-D and 3-D RANS simulations at Re=41300 conducted by Ünal et al. [65], Ünal and Gören [66], it seems that the results from RANS are similar to each other. The Strouhal number and drag force shows good agreements with the present study. However, the predicted values of both lift and back pressure exhibit large differences between Case-C4 and 3-D RANS simulation.

3.4.3 SGS modelling effect on mean flow statistics

The mean velocity profiles behind the cylinder obtained with the SGS models are examined in detail. It is noted that the experimental measurements of Ünal and Atlar [64] were time-averaged but taken in the spanwise mid-section of the cylinder. Figure 3.14 shows the time- and spanwise-averaged velocity profiles along the cylinder centreline for Case-C2 to C4 in comparison with experimental data measured by Ünal and Atlar [64]. In Figure 3.14(a) non-dimensional mean streamwise velocity u/U profiles are plotted along x/D=0.6 and 1.0. The results obtained at x/D=0.6, which is located around the cylinder base, show close approximations with experimental measurement. At a point downstream of the cylinder base (x/D=1.0), Case-C2 and C3 tend to slightly over-predict the velocity generally.

Figure 3.14(b) shows non-dimensional mean crossflow velocity v/U profiles at x/D=0.6 and 1.5. In contrast to the profiles of u/U, the mean crossflow velocities around the cylinder base (x/D=0.6) obtained with all the SGS models are under-estimated as y/D increased. It seems that the crossflow velocity is more affected by the cylinder wake than the streamwise velocity as Ünal et al. [65] have already pointed out. At a point more downstream of the cylinder base (x/D=1.5) the crossflow velocities are generally over-predicted compared to experiments. The comparison between simulations indicates that results obtained with the dynamic SGS model (Case-C4) exhibit a relatively satisfactory agreement with experimental measurements.

TABLE 3.9: Mean flow statistics in the cylinder wake at Re=41300.

Cases	$u/U\|_{min}$	$u'u'/U^2\|_{max}$	$\|u'v'/U^2\|$
C2: TKE+WM	-0.21[1] (0.78,0.00)[2]	0.39 (0.89,0.43)	0.17 (1.30,0.29)
C3: SMG+WM	-0.23 (0.79,0.00)	0.37 (0.92,0.43)	0.17 (1.30,0.31)
C4: DTKE+WM	-0.23 (0.86,0.00)	0.35 (0.95,0.45)	0.17 (1.30,0.33)
Experiments by Ünal and Atlar [64][3]	-0.25 (0.87,0.00)	0.20 (1.13,0.41)	0.14 (1.40,0.38)

[1] Noted as the peak value of the mean flow statistic.
[2] Noted as the location of the peak value (x/D,y/D).
[3] The statistics in the experiment were measured in the spanwise mid-section of the cylinder.

The mean flow distributions in the cylinder wake, u/U, $u'u'/U^2$ and $u'v'/U^2$, are investigated in detail. These quantities obtained with different SGS models are also averaged temporally and spatially along the cylinder axis direction.

Figure 3.15 shows a comparison of the normalised mean streamwise velocity u/U contours between the experiment and simulations obtained with the SGS models. The negative bubble behind the cylinder base along x/D is clearly shown in all simulation results. The overall distance of the negative bubble from the cylinder base to the location

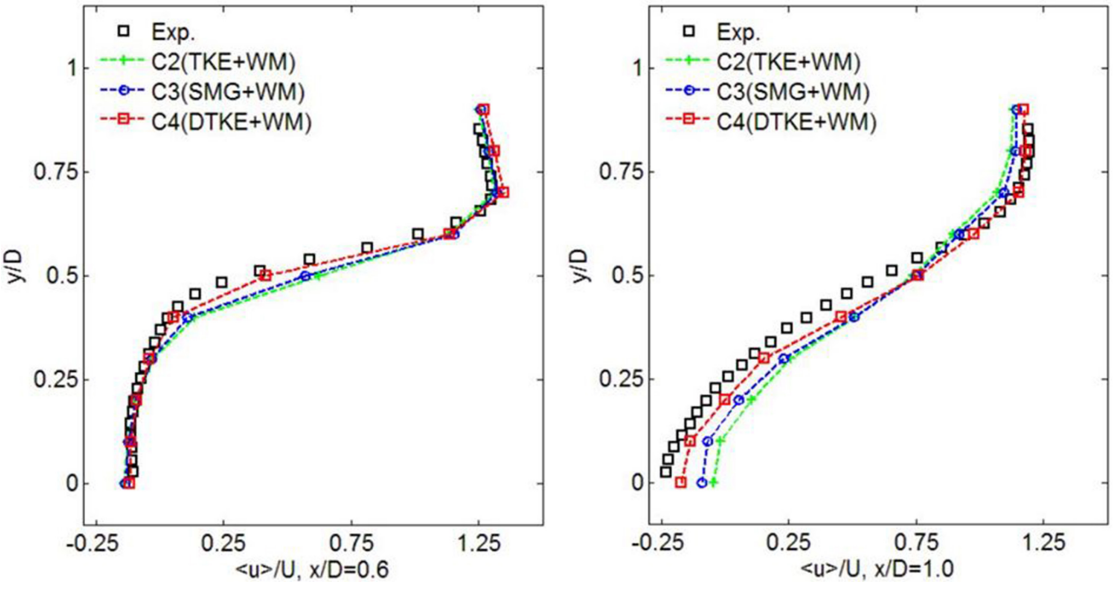

(a) Mean streamwise velocity u/U profiles at x/D=0.6(left) and 1.0(right).

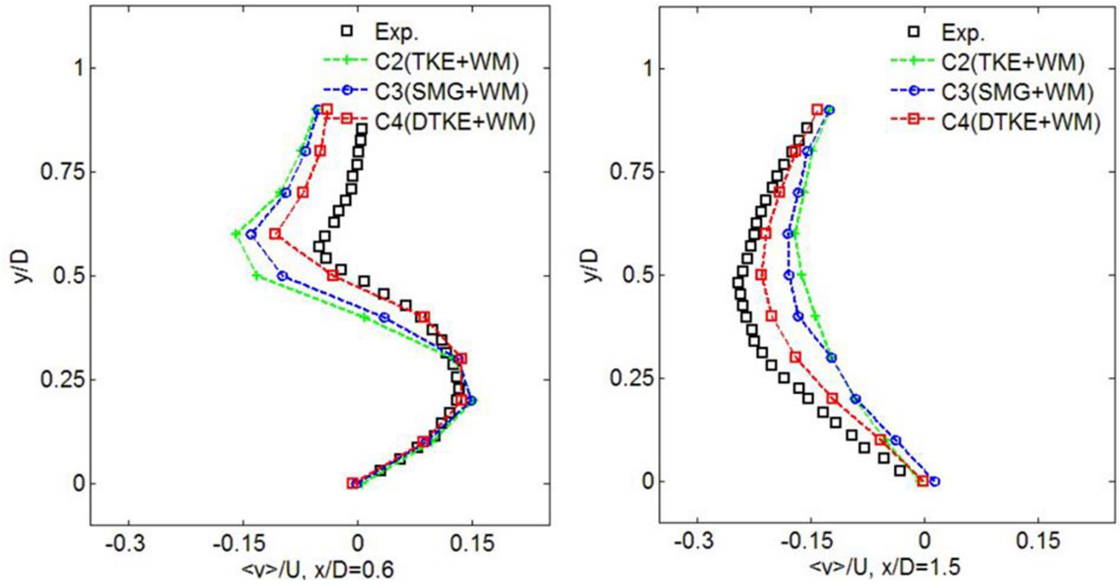

(b) Mean crossflow velocity v/U profiles at x/D=0.6(left) and 1.5(right).

FIGURE 3.14: Mean velocity profiles along centreline using different SGS models.

at zero velocity along x/D are $0.55D$, $0.59D$ and $0.68D$, for Case-C2 to C4 respectively. The relative change of the distance between Case-C2 and C4 is nearly 23.6%. The peak values of negative velocity and its locations are summarised in Table 3.9. The predicted values are slightly under-estimated in Case-C2 and C3, whereas Case-C4 obtained with the dynamic model produces close approximations compared to experimental data. The small difference between the experiment and simulation might be due to the averaging method.

The normalised streamwise velocity fluctuations $u'u'/U^2$ are plotted in Figure 3.16, where u' is streamwise r.m.s.velocity. The distributions show strong fluctuations in the separating shear layers behind the cylinder. Although the overall patterns of the distribution estimated with all the SGS models are similar to experimental observation,

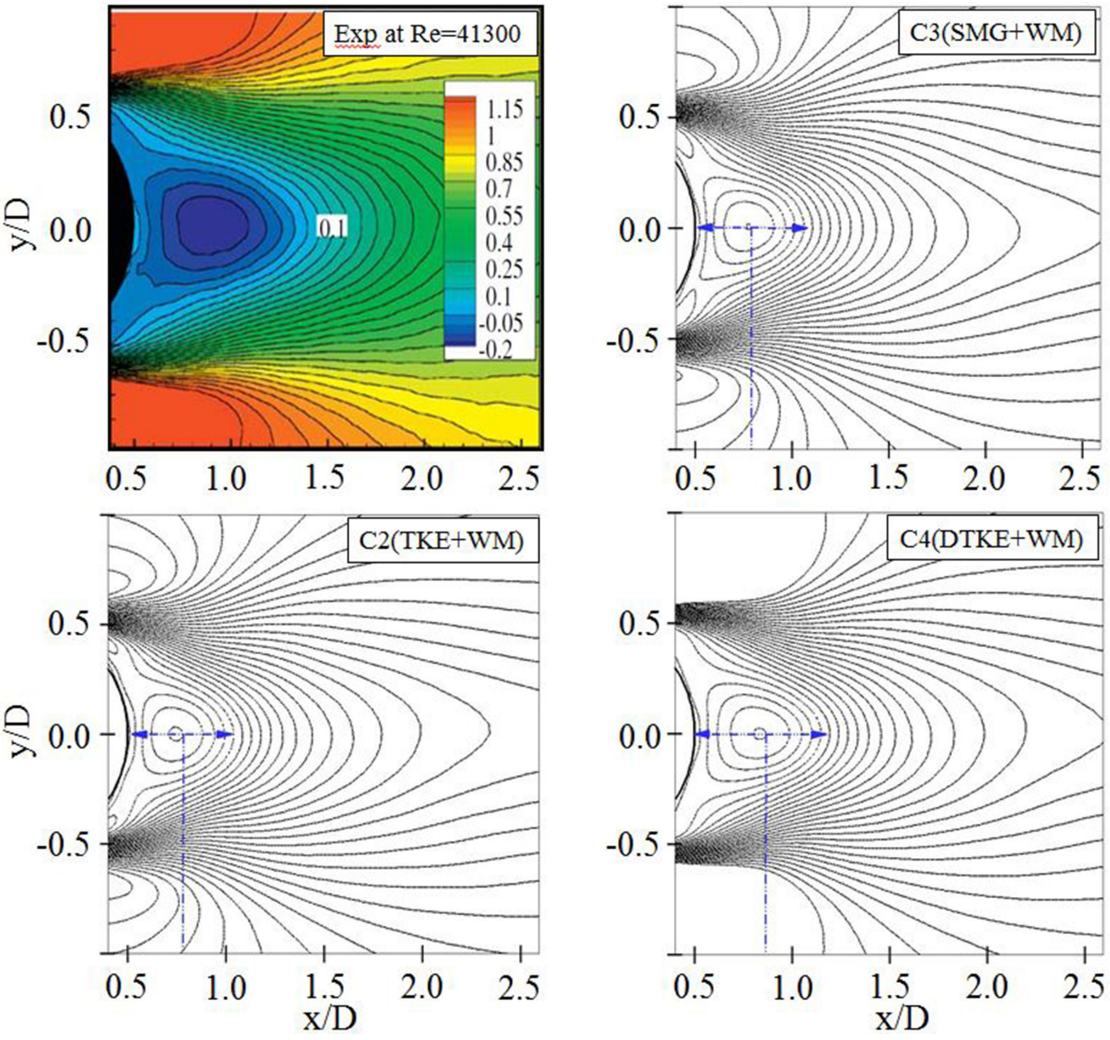

FIGURE 3.15: Comparison of the normalised mean streamwise velocity u/U between experiments and present simulations: $\Delta u/U$=0.05 in all simulation cases.

the predicted peak values in the fluctuations are considerably over-estimated and the locations of the peaks are shifted upstream for all simulation cases compared to experimental data, as shown in Table 3.9. The maximum value and its location, however, are more accurately estimated with the dynamic SGS model among the simulation sets.

Figure 3.17 shows the normalised shear stress $u'v'/U^2$ distributions, where v' is cross-flow r.m.s. velocity. The characteristic anti-symmetric pattern of the stress is clearly captured and the magnitude of the peak is 0.17 in all simulations, comparable to the experimental value of 0.14. The locations of dominant peaks are $(x/D, y/D)$=(1.3, 0.33) and (1.4, 0.38) in Case-C3 and the experiment respectively. Although all SGS models predict the stress distribution of the near-wake structure with an acceptable accuracy,

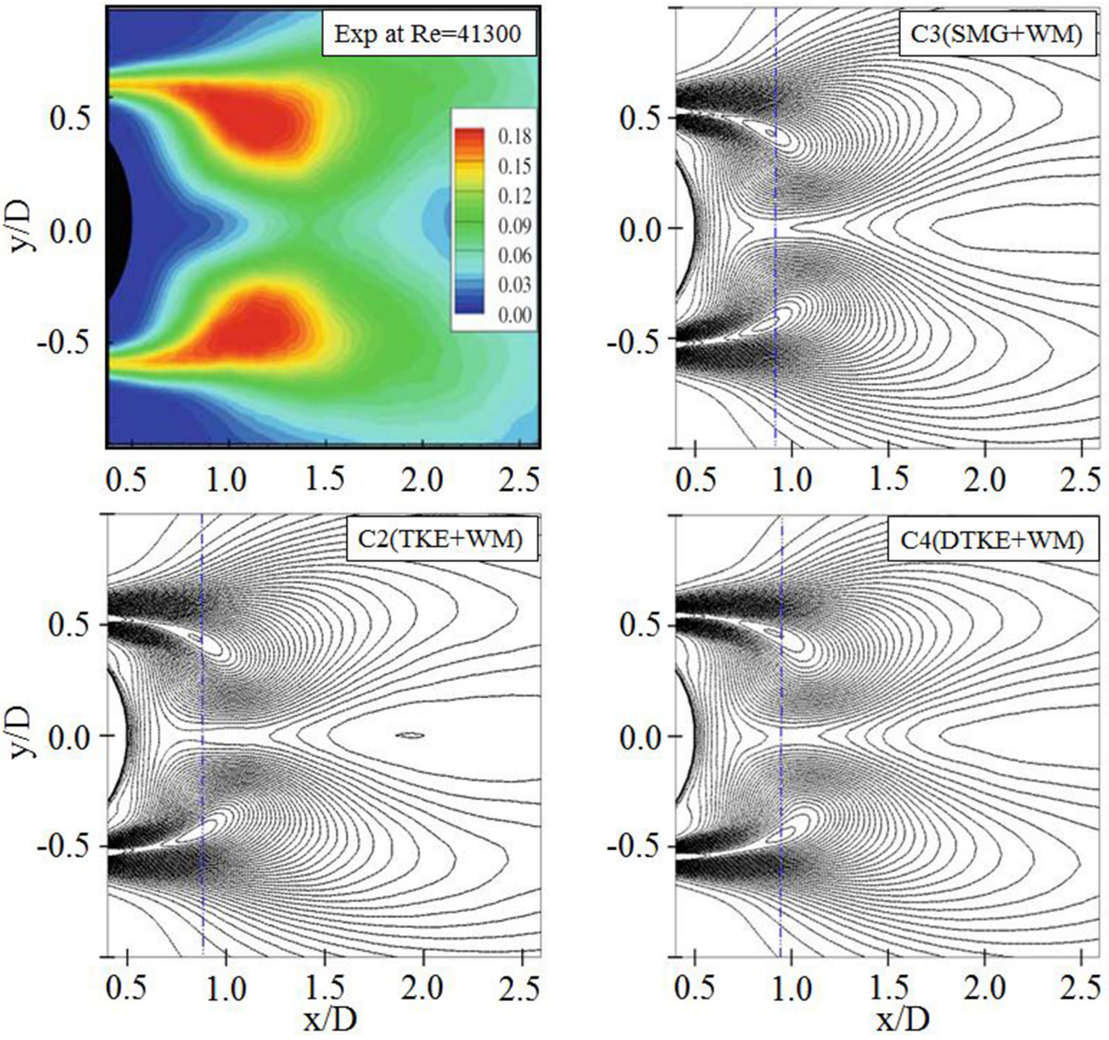

FIGURE 3.16: Comparison of the normalised mean streamwise volocity fluctuations $u'u'/U^2$ between experiments and present simulations: $\Delta u'u'/U^2$=0.01 in all simulation cases.

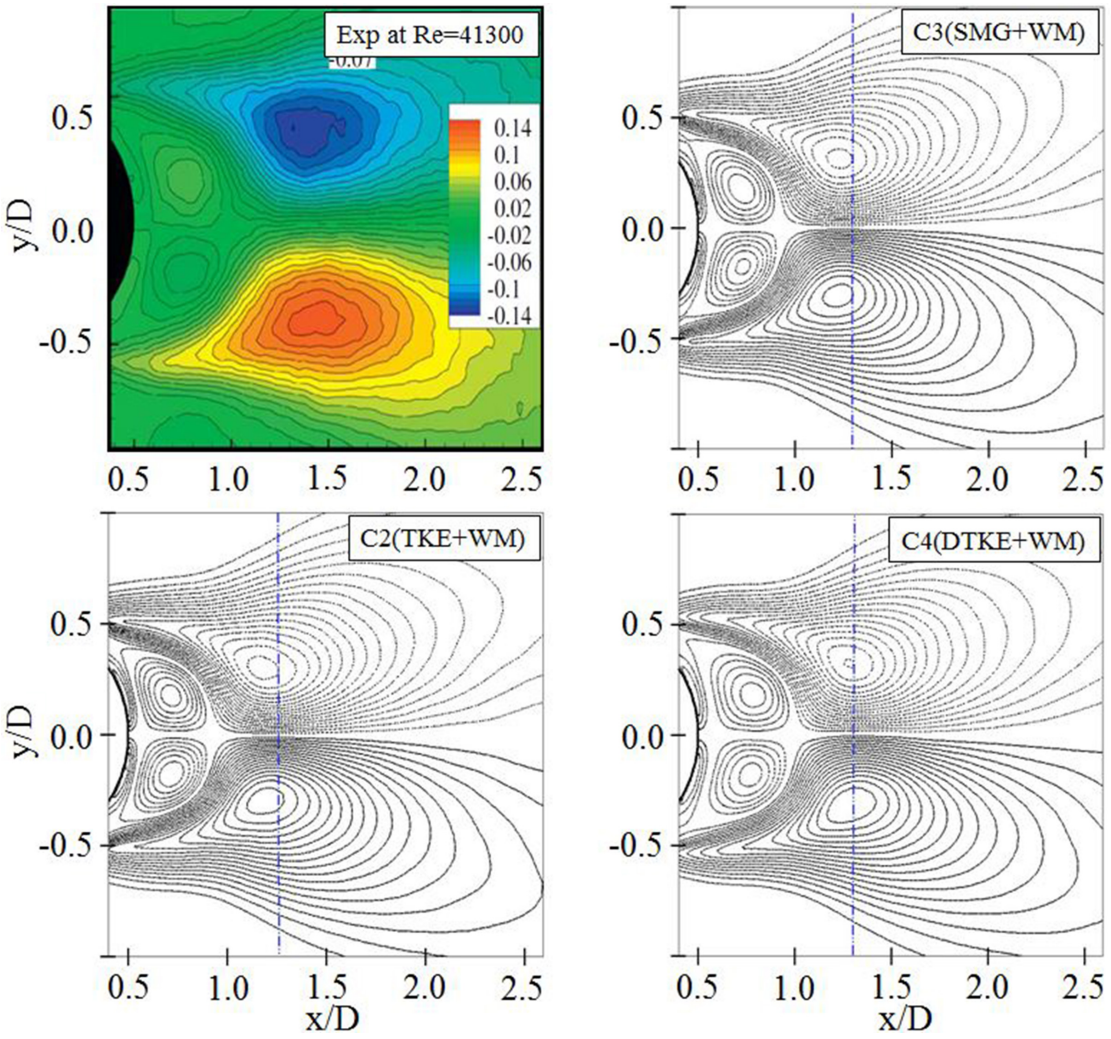

FIGURE 3.17: Comparison of the normalised mean shear stress $u'v'/U^2$ between experiments and present simulations: $\Delta u'v'/U^2$=0.01 in all simulation cases.

the better results compared to experiments are achieved by Case-C3 with the dynamic model at Re=41300.

3.5 Closure

For a complete validation of LES simulation of turbulent flow behind a cylinder, grid-sensitivity studies were conducted at a range of subcritical Reynolds numbers. At Re=5500, the extensive grid test indicated that high resolution grids in the spanwise direction are required to predict accurate force coefficients. Both the simulation without SGS modelling and 2-D calculation were carried out, emphasising the modelling effect

TABLE 3.10: Grid sensitivity results.

Reynolds	Cases	Resolutions	SGS model	Scheme	$\Delta tU/D$	Max.y^+
5500	LES-B3	3.11 M	Smagorinsky	CD	0.0020	≈1.0
10000	LES-B5	3.68 M	k-equation	CD	0.0010	≈1.0
41300	Case-C4	5.76 M	Dynamic k-eq.	CD	0.0005	≈1.0

and three-dimensionality of the cylinder wake respectively. Moreover, numerical dissipation produced by a scheme in LES was clearly presented. Based on these numerical and modelling aspects, the conventional Smagorinsky model works well in terms of hydrodynamic force and pressure at this flow condition. The mean flow statistics were also produced in order to gain data from 3-D LES simulation.

However, at a higher Reynolds number of 10000, the importance of the SGS modelling significantly increased. The force coefficients obtained with the conventional Smagorinsky model were significantly under-predicted on the highest resolution grid. On the other hand, the algebraic k-equation SGS model produced reasonable results on the same grid. The superiority of the dynamic model over two algebraic type models could not be clearly proved, with the exception that no proper model constant has to be chosen.

A challenging high-Re flow at Re=41300 was also examined with particular focus on the SGS model. Due to resource limitations, only three grids were tested and it is already a challenge to achieve grid-independent results for 3-D LES. To achieve the grid independence, fine grid resolution around the cylinder was generated, resulting in a lower y^+ value. Moreover, the near-wall model was applied to all SGS models. The dynamic model yielded the best solution which agrees fairly well with experimental measurements. The study of SGS modelling effects was extended to the mean flow statistics at Re=41300. Although three models produced overall agreement with experimental measurements, the results with the dynamic model demonstrated superior performance in predicting the mean flows.

To conclude of this Chapter, grid independence and the important role of the numerical and modelling aspects at each flow condition have to be emphasised. The best results are achieved as shown in Table 3.10 and could be used confidently for the rest of simulation based on the present grid-independence analysis.

Chapter 4

REYNOLDS NUMBER EFFECTS ON NEAR-WAKE STRUCTURE AND SHEAR-LAYER INSTABILITY

In this Chapter, the near-wake structure of a circular cylinder and the resulting shear-layer instability are examined for a range of Reynolds numbers. The Reynolds numbers based on the free-stream velocity U and the cylinder diameter D range from Re=5500-41300, where the shear-layer instability in the intermediate subcritical flow regime (TrSL3) is fully developing, as discussed in Chapter 1. Therefore, the present work in this Chapter is mainly devoted to describing the turbulence flow in the near wake of a circular cylinder by interaction between vortical motions of different scales, and to determine or obtain clear numerical evidence of Reynold number dependency of the shear-layer frequency as the Reynolds number increases within the subcritical flow regime.

One of the most interesting aspects of flow past a circular cylinder is the large change in the formation length of the near wake over the range of Reynolds numbers extending from Re=1000-10000, as discussed in the literature review. A variety of investigations have shown that there are substantial changes of both the mean base pressure coefficient $-C_{pb}$ and fluctuating lift coefficient C'_L over the range of Reynolds numbers. In the

initial section of this Chapter, therefore, the variation of the near-wake structures of a cylinder at Reynolds numbers of 5500-41300, which correspond to development of shear-layer instabilities, is discussed in detail in terms of time- and spanwise-averaged flow statistics such as mean flow and Reynolds stresses in turbulent flow. The LES results, which were briefly presented in Chapter 3, will be re-discussed at each Reynolds number and compared with available experimental and DNS data.

The variation of the near-wake structures is intimately associated with the shear-layer instability or Kelvin-Helmholtz instability, which leads to small-scale vortices in the thin layer. Last part of this Chapter, therefore, the Reynolds number scaling of the shear-layer instability frequency is numerically investigated and discussed. The shear layer or the separated thin boundary layer of the cylinder, rolls up and forms the Kármán vortices within a few diameters. The Reynolds number seems to have a significant influence on the characteristics of the shear layer. However, the variation of the shear-layer frequency with Reynolds number has been the subject of some debate for last two decades. Concerning the shear-layer frequency, Prasad and Williamson [24] have compiled all previous experimental data and suggested a power law of $Re^{0.675}$ for the dependency of frequency of the shear-layer vortices on the Reynolds number. To obtain the frequency of small-scale shear-layer vortices numerically, the power spectra of the flow velocities in the thin shear-layer are applied to LES data. The LES solutions of the shear-layer frequency are directly compared with experimental measurements.

It should be noted that all DNS and experimental data, which are cited in the present study, are from Dong et al. [3] for Re=3900-10000 and Ünal and Atlar [64] for Re=41300 respectively. The DNS data were averaged temporally and spatially in a spanwise or cylinder axis-direction, but the experimental data were measured in the spanwise mid-section.

The LES simulations in this Chapter are performed using different grid resolutions and SGS models in order to predict qualitative and reasonable results at each Reynolds number, as discussed in the previous Chapter. Therefore, all simulation results are based on Table 3.10 in the previous Chapter and all numerical solutions are time- and spanwise-averaged in a homogeneous z-direction.

4.1 Reynolds Number Effect on Near-wake Structure

Crucial features of the near-wake structure over the range of considered Reynolds numbers are the change in formation length of the shear layer and the development of the Kelvin-Helmholtz instability in the freely separating shear layers formed from the cylinder surface, which eventually leads to small-scale vortices. When the formation length is long, the separating shear layers are relatively unaffected by the large-scale vortex shedding, which occurs much further downstream. On the other hand, when the length is short at the higher Reynolds number, the shear layers are strongly affected. In this section, the variation of the wake structure is mainly discussed in order to predict the shear-layer frequency reasonably.

As briefly discussed in previous Chapter 3, the mean flow characteristics in the cylinder wake are examined in detail. Figure 4.1(a) shows the distribution of the normalised mean streamwise velocity u/U from the DNS data in Figure 4.1(a-1) at Re=3900 and from the simulation in Figure 4.1(-2) at Re=5500. Both plots show the cluster of the negative velocity along the cylinder x/D. The measured length of the cluster from the cylinder base to the location at zero velocity is x/D=1.36 in DNS, whereas the predicted value of 1.24 was obtained in LES. The peak values of negative velocity are -0.29 and -0.3 for DNS and LES respectively. The overall pattern and location of the peak value for the mean flow at Re=5500 shows reasonably good agreement with experimental measurement at Re=3900, considering the fact that the formation length of shear layers is severely shortened to between Re=1000-10000 as discussed in Thompson and Hourigan [19]. The predicted peak values and their locations are summarised in Table 4.1.

In Figure 4.1(b) the predicted length of the cluster from the cylinder base to the location at zero velocity is x/D=0.80, whereas the value of 0.82 was obtained in the DNS

TABLE 4.1: Summary of flow statistics in the cylinder wake in 3-D LES.

Mean flow statistics		Re=5500	Re=10000	Re=41300
u/U	Peak	Min. -0.33	Min. -0.26	Min. -0.23
	Bubble length	$1.24D$	$0.80D$	$0.68D$
$u'u'/U^2$	Peak	Max. 0.22	Max. 0.33	Max. 0.35
	x/D	1.5	1.15	0.95
$u'v'/U^2$	Peak	$\pm$0.13	$\pm$0.17	$\pm$0.17
	x/D	1.8	1.5	1.3

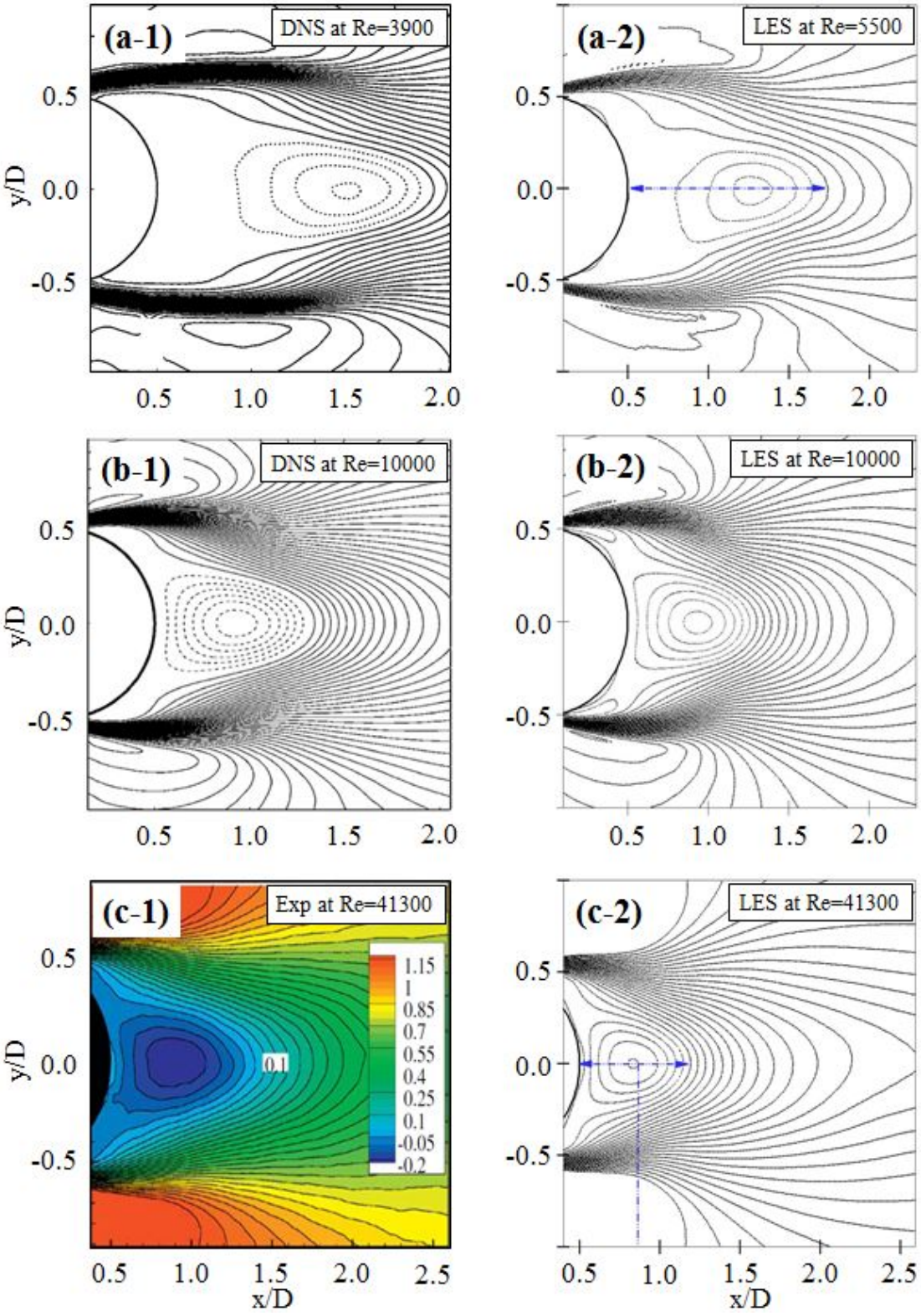

FIGURE 4.1: Contours of normalised mean streamwise velocity u/U over Re=5500-41300: reference data are in the left column and simulation results are in the right column. Noted that the experiment was measured in the spanwise mid-section of the cylinder.

data. It is noted that the recirculation length in the PIV experiment of Dong et al. [3] was measured as x/D=0.78 at Re=10000. This good agreement with the experiment indicates that the present study has entirely well calculated the essential feature of the flow at the subcritical Reynolds number. In LES from Re=5500-10000, the length of the cluster is significantly decreased from 1.24 to 0.80 as about 35.5%.

The distribution of u/U at Re=41300 is computed as shown in Figure 4.1(c). The minimum value of negative velocity was measured as -0.25 at x/D=0.87 in the experiment and -0.235 at x/D=0.86. As the Reynolds number increased from Re=10000-41300, the LES solutions clearly show that the length of the cluster also substantially decreased from 0.92 to 0.68 about 35.3%.

The variation of the cluster of negative velocity in u/U indicates that the bubble length severely shortened and finally reached very close to the base of the cylinder over Re=5500-41300. This variation of the length seems to be accompanied by corresponding variation of the magnitude of the base suction pressure coefficient $-C_{pb}$, which is obtained at a location 180° from the forward separation point or the cylinder base, as shown in Figure 4.4.

Figure 4.2 shows strong fluctuations of the streamwise velocity in the separating shear layers at the considered Reynolds number. At Re=5500, the peak values of $u'u'/U^2$ in the separating shear layer are 0.20 at x/D=1.55 and 0.22 x/D=1.5 in DNS and LES respectively. It is noted that the original data used in Dong et al. [3] is u'/U=0.45 and the peak value of 0.20 cited in the present study is simply calculated as 0.45^2.

The distribution of the normalised r.m.s. streamwise velocity $u'u'/U$ at Re=10000 is computed as shown in Figure 4.2(b). The location of maximum fluctuation in the shear layer is at x/D=1.15 in LES and 1.13 in the DNS data. The peak value of the fluctuation is $u'u'/U$=0.33 and 0.25 respectively.

The velocity fluctuation at Re=41300 is, however, measured as peak value of 0.20 at $(x/D, y/D)$=(1.13,0.41) in the experiment, whereas the predicted value is 0.35 at (0.95,0.45). The present LES shows significant upstream movements of the peak locations of the fluctuations in the shear layers at Re=5500-41300. This variation of the velocity fluctuation magnitudes in the separating shear layers seems to cause the variation of lift fluctuation C'_L with increasing Reynolds numbers.

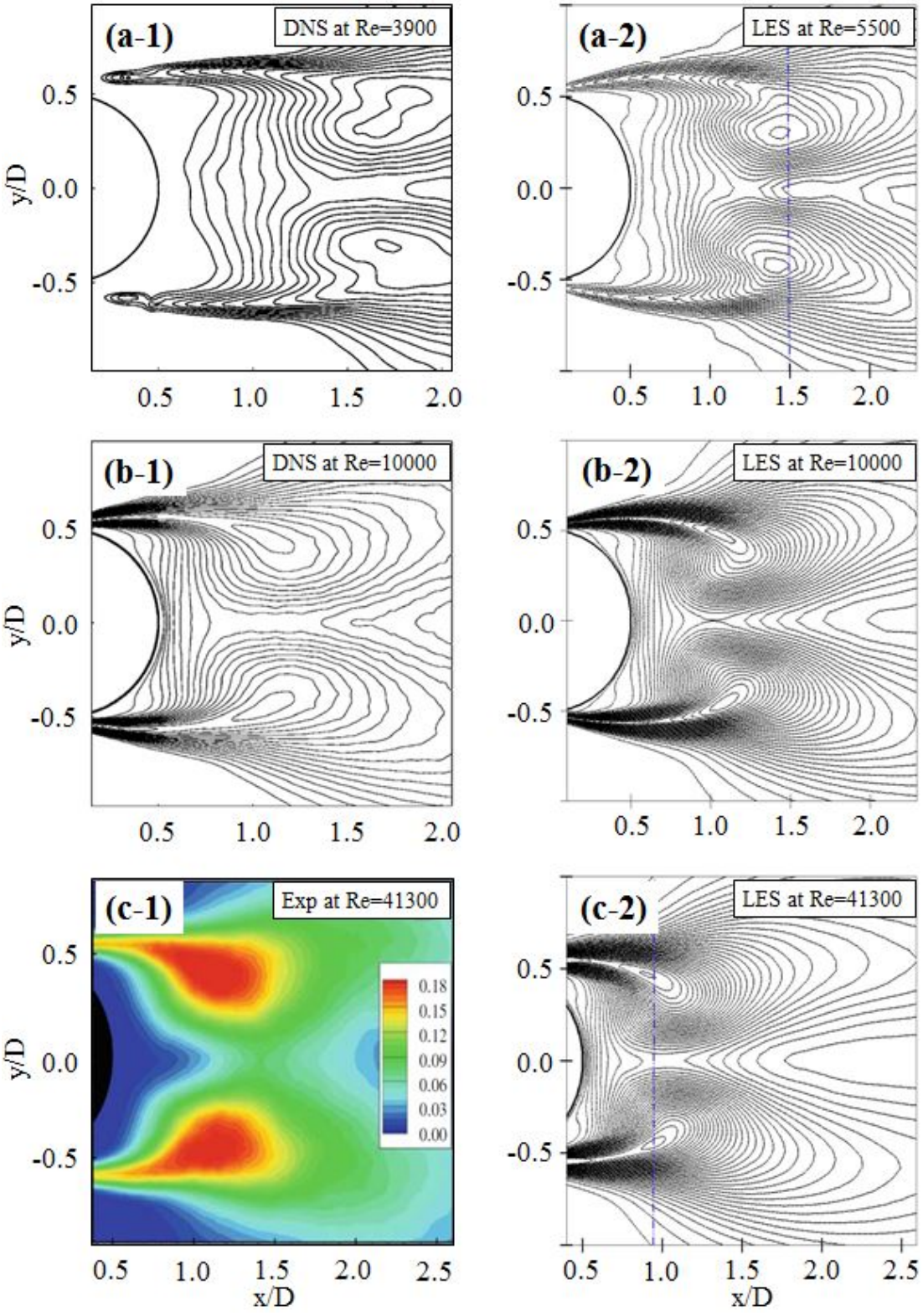

FIGURE 4.2: Contours of normalised streamwise velocity fluctuations $u'u'/U^2$ of Reynolds stresses over Re=5500-41300: reference data are in the left column and simulation results are in the right column.

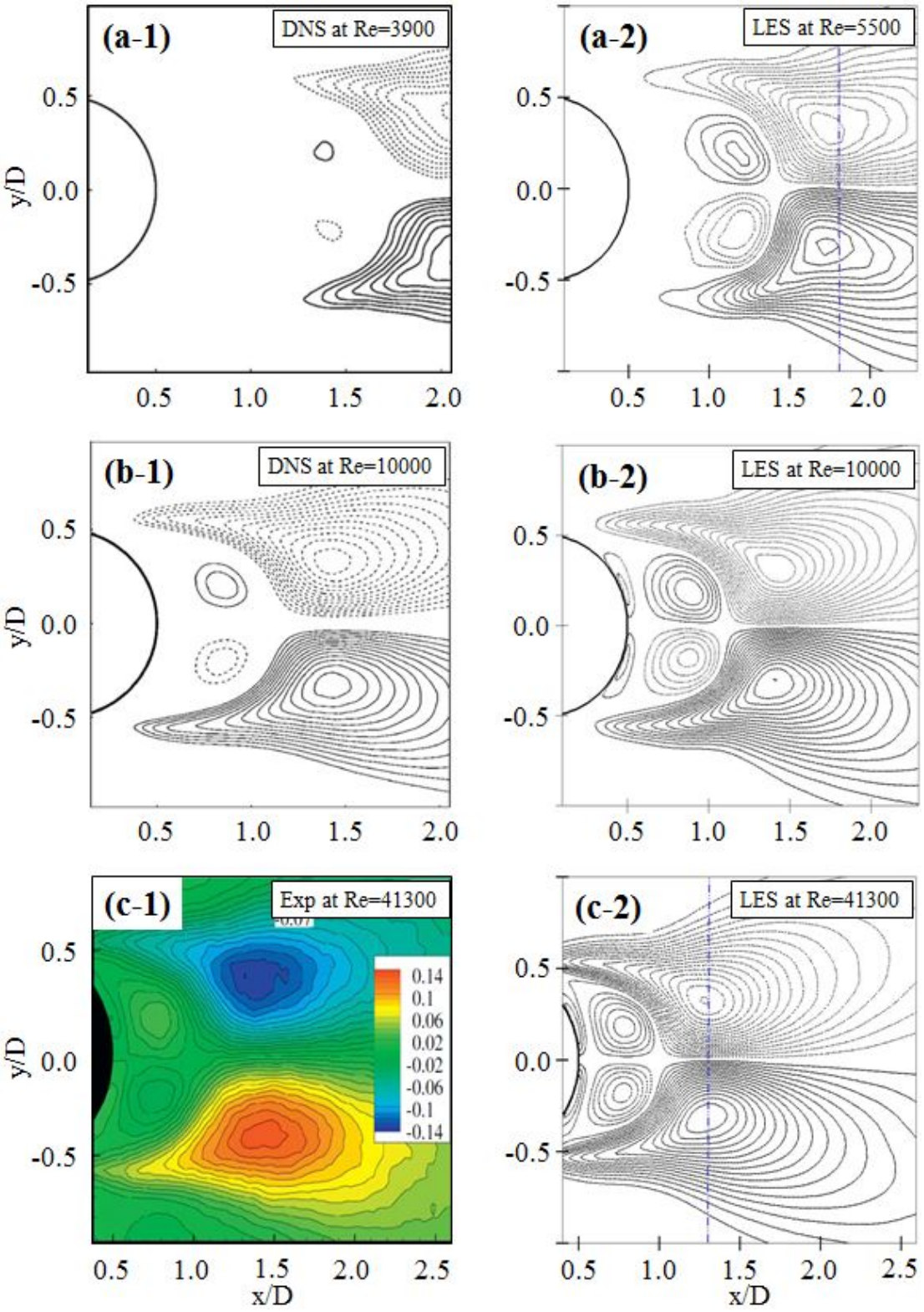

FIGURE 4.3: Contours of normalised shear stress $u'v'/U^2$ of Reynolds stresses over Re=5500-41300: reference data are in the left column and simulation results are in the right column.

The normalised shear stress $u'v'/U^2$ contour is plotted as shown in Figure 4.3. The overall distribution of the four distinct clusters, which are antisymmetric along the cylinder centreline y/D=0, is similar to each contour. The maximum peak level of the shear stress for Re=3900/5500 is 0.14 at x/D=1.90 and 0.13 at x/D=1.81 in DNS and LES respectively.

The computed normalised shear stress $u'v'/U^2$ contour at Re=10000 is plotted as shown in Figure 4.3(b). The predicted location of the peak stress is at x/D=1.5 in the present study and 1.4 in the DNS data. The maximum peak level of the stress is 0.17, comparable to the value of 0.15 in the DNS data.

The maximum magnitude of shear stress at Re=41300 is 0.17 at $(x/D, y/D)$=(1.4,0.38)

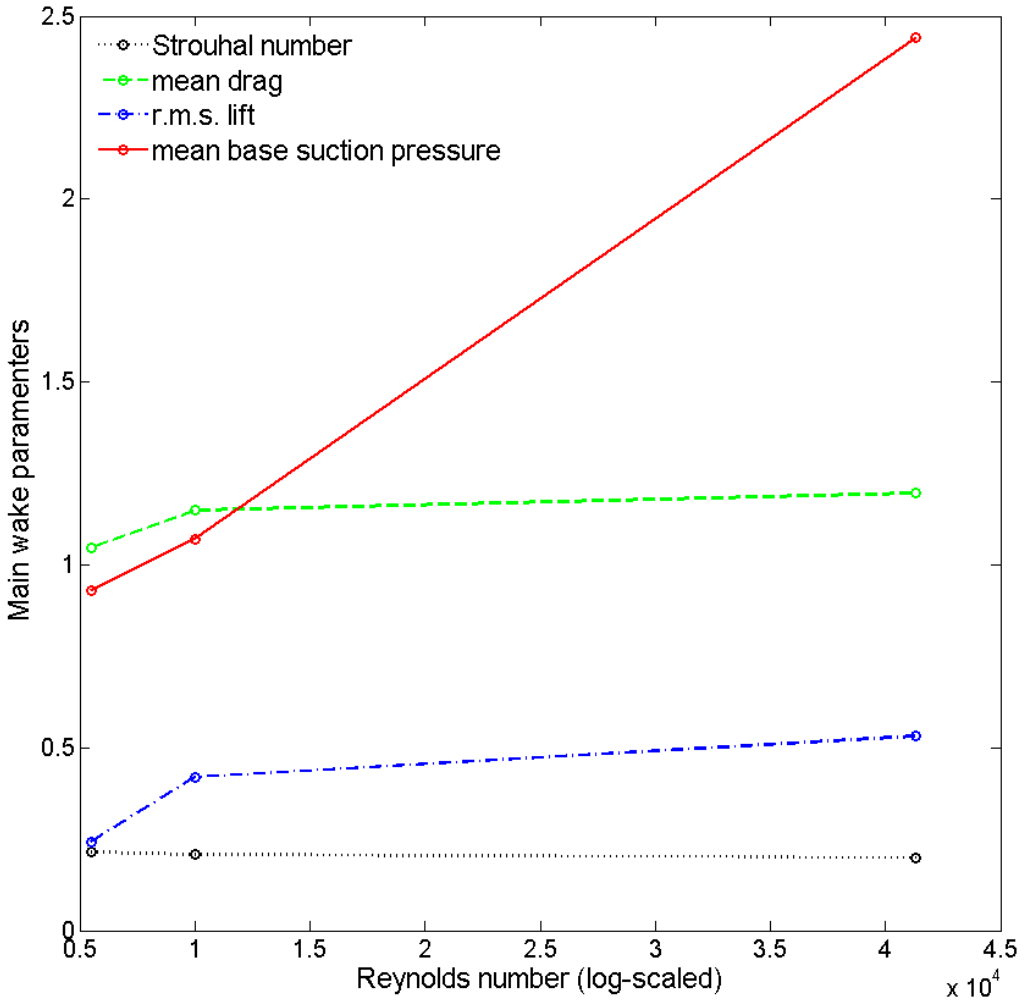

FIGURE 4.4: Variations of main wake parameters between Re=5500 and 41300.

in the experiment, comparable to the predicted value of 0.17 at (1.3,0.33). The small difference between the experiment and simulation might be due to the averaging method. In the experiment, all the flow quantities and the pattern of near-wake structures were measured with time averaging but obtained in the spanwise mid-section of the cylinder. As discussed in Figure 3.6 in the previous Chapter, the instantaneous flow in the spanwise mid-section and the spanwise-averaged flow variable showed some difference in their patterns.

In the LES solution of the shear stress, it is noted that the tip of the large-scale cluster with the maximum peak level of the shear stress tends to extend very close to the separation point on the cylinder surface as the Reynolds number increases, which is indicative of the early transition of the shear layer at Re=41300, compared to those at Re=5500 and 10000.

Figure 4.4 shows variations of main wake parameters obtained from LES simulations. The Strouhal number St is a relatively insignificant change when the Reynolds number is varied over Re=5500-41300. The mean drag $\bar{C_D}$ and fluctuating lift coefficient C_L' show substantial increases from Re=5500-10000 and gradually increase up to Re=41300. The mean base suction pressure $-C_{pb}$ describes a similar change compared with the variation of the forces over Re=5500-10000, but shows a sharp increase when the Reynolds number further increases.

In this section, the averaged flow fields from LES clearly showed the upstream movement of the near-wake structures immediately adjacent to the cylinder base with increasing Reynolds numbers. Furthermore, the averaged representations of the velocity field and Reynolds stresses in the near-wake of a circular cylinder clearly showed the wake structures associated with the variations in the base suction pressure and force coefficients over the Reynolds numbers range of $5500 \leq Re \leq 41300$.

4.2 Reynolds Number Effect on Shear-layer Frequency

The shedding of the large-scale Kármán vortices from a circular cylinder results from the interaction of the two separating shear layers from the thin boundary layer. Wu et al. [18] noted that small-scale vortices, because of the Kelvin-Helmholtz (KH) instability, develop in the separated shear layers prior to the formation of the large-scale

vortices. The variation of the near-wake structure and shear-layer instability, therefore, are intrinsically linked to each other and the variation of Reynolds numbers influences the shear-layer instability significantly. Based on reviews of the literature on shear-layer instability, the KH vortical structures or shear-layer vortices appear in a very intermittent way within the subcritcal flow regime, indicating that it is difficult to observe the small-scale vortices on instantaneous flow fields. Previous experimental and numerical works, however, clearly showed the normalised ratio of the shear-layer frequency over the Kármán frequency increased as a power of the Reynolds number, even though there has been some controversy regarding the dependence of the normalised shear-layer frequency on the Reynolds number. In this section, power spectral analysis is employed to capture the frequency of small-scale vortices in thin separating shear layer.

In Figure 4.5(a,left), the time history of the instantaneous crossflow velocity is at the point of x/D=1.00 and y/D=0.65, which is located around the upper shear layer in the near wake. In order to obtain the frequency of shear-layer vortices at the point, the power spectrum of the crossflow velocity is calculated as shown in Figure 4.5(a,right).

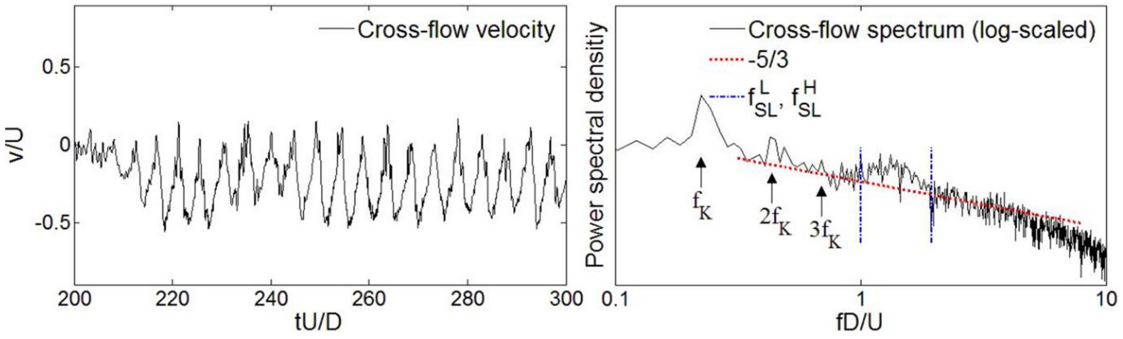

(a) The velocity and power spectra at the point of $(x/D,y/D)$=(1.0,0.65) around upper shear layer in the wake.

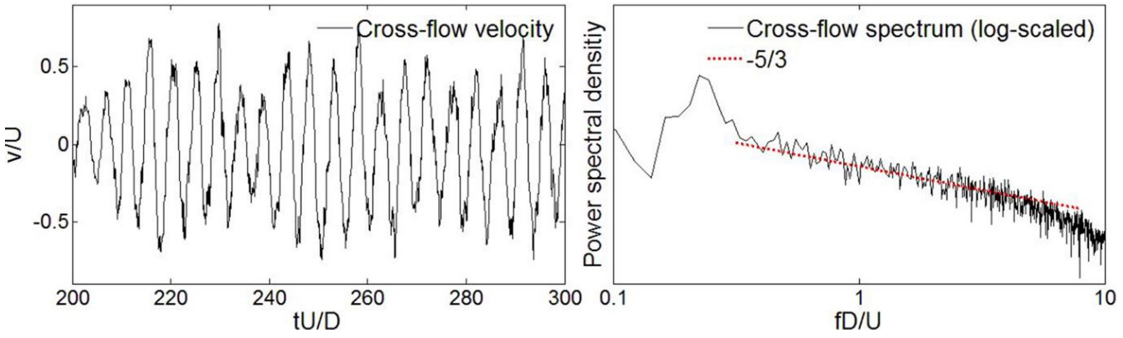

(b) The velocity and power spectra at the point of $(x/D,y/D)$=(1.0,0.0), the downstream location of the upper shear layer in the wake.

FIGURE 4.5: Time trace of instantaneous crossflow velocity v (left column) and its power spectra of the velocity (right column) at Re=5500.

The computed flow spectra are spanwise-averaged at the corresponding point. The Kármán frequency f_K and its sub-harmonics $2f_K$ and $3f_K$ are visible at a range of low frequencies in the spectrum, and the spectrum exhibits exponential decay following the -5/3 law in the inertial subrange as discussed in Figure 2.1. In contrast to the sharp peaks of f_K at lower frequencies, the broadband peak is numerically captured at a range of higher frequencies, which is consistent with the broadband nature of the shear-layer frequency f_{SL} observed in previous experimental studies. The present LES study clearly shows well-defined broadband spectral peaks between lower and higher bounds of shear-layer frequencies f_{SL}^L and f_{SL}^H.

The mean value of normalised shear-layer frequency f_{SL}/f_K=7.372 is estimated as defined in Dong et al. [3]:

$$\frac{f_{SL}}{f_K} = \frac{1}{2} \times \left(\frac{f_{SL}^L}{f_K} + \frac{f_{SL}^H}{f_K} \right), \tag{4.1}$$

However, the normalised shear-layer frequency f_{SL}/f_K is predicted to be slightly lower than the value obtained from the correlation suggested by Prasad and Williamson [24]:

$$\frac{f_{SL}}{f_K} = 0.0235 \times \mathrm{Re}^{0.67}, \text{ where } 1200 \leq \mathrm{Re} \leq 45000. \tag{4.2}$$

The power spectrum in Figure 4.5(b,right) is obtained at the point of x/D=1.0 and y/D=0.0, which is located the cylinder base downstream along the cylinder centreline. The sharp spectral peak indicates the Kármán frequency and then the spectrum exhibits exponential decay as well. It is noted that the broadband peak of shear-layer vortices vanishes outside of the shear layer and the disappearance of the signature in the spectra is indicative of the spatial locality of the small-scale vortices.

Figure 4.6 shows the instantaneous velocity components, u and v, and the power spectra of each velocity component at two different points, outside and inside of shear layer. At a point of (x/D,y/D)=(0.70,0.00) downstream of the cylinder base along the cylinder centreline, the instantaneous crossflow velocity v exhibits low-frequency dominant behaviour of large-scale fluctuation and also displays high-frequency fluctuations on the top of large-scale fluctuations as shown in Figure 4.6(b-left). In the corresponding power spectra in the right column, as expected, the sharp peak is captured at f_K and the spectrum at Re=10000 exhibits exponential decay in the inertial subrange as well.

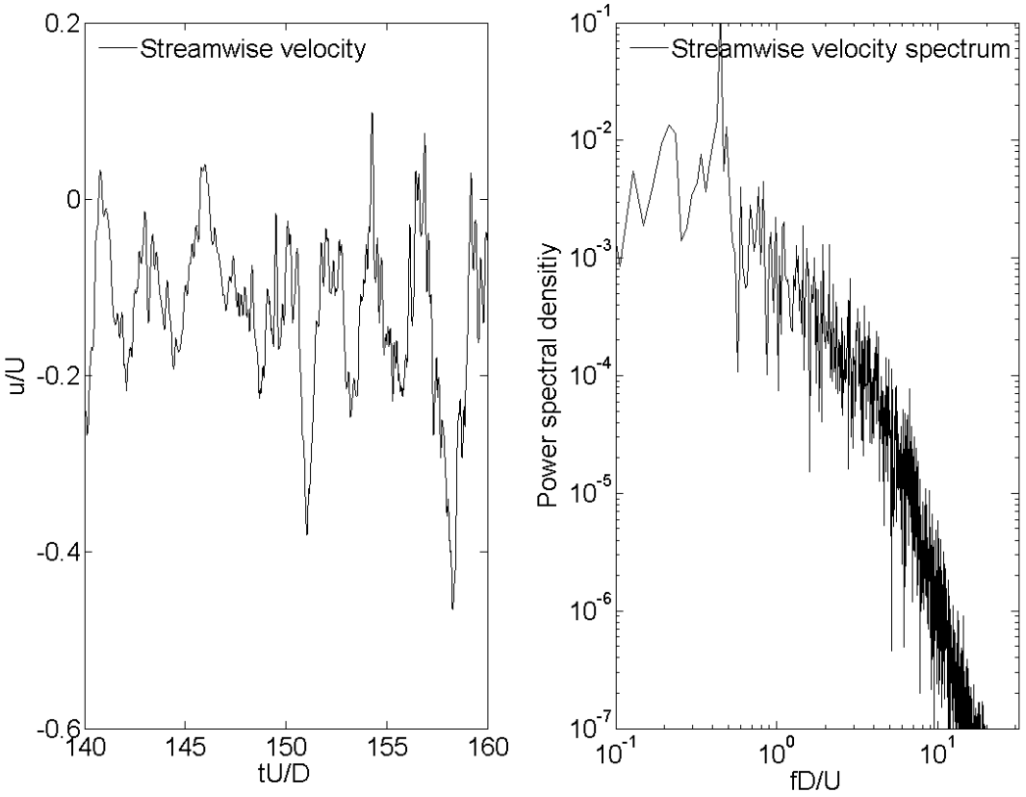

(a) Time trace of instantaneous streamwise velocity u.

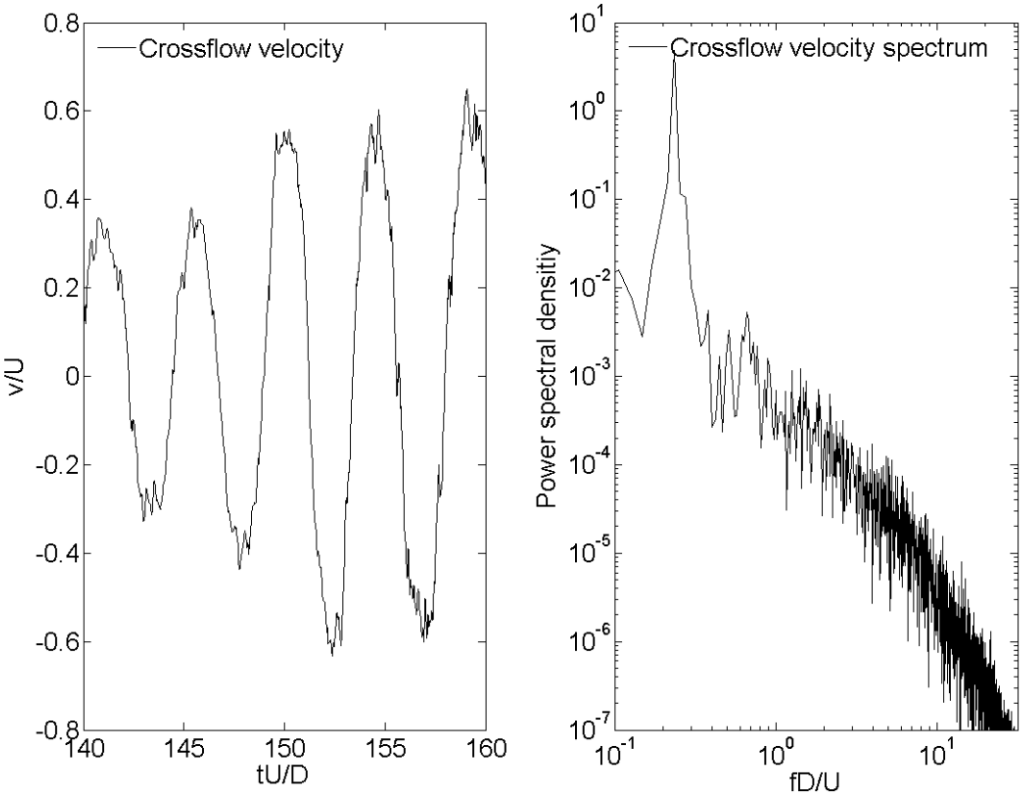

(b) The power spectra of instantaneous crossflow velocity v.

FIGURE 4.6: Time trace of instantaneous velocities (left column) and power spectra of the velocities (right column) at Re=10000: all plots are obtained at the point of $(x/D,y/D)$=(0.70,0.00) outside of the shear layer.

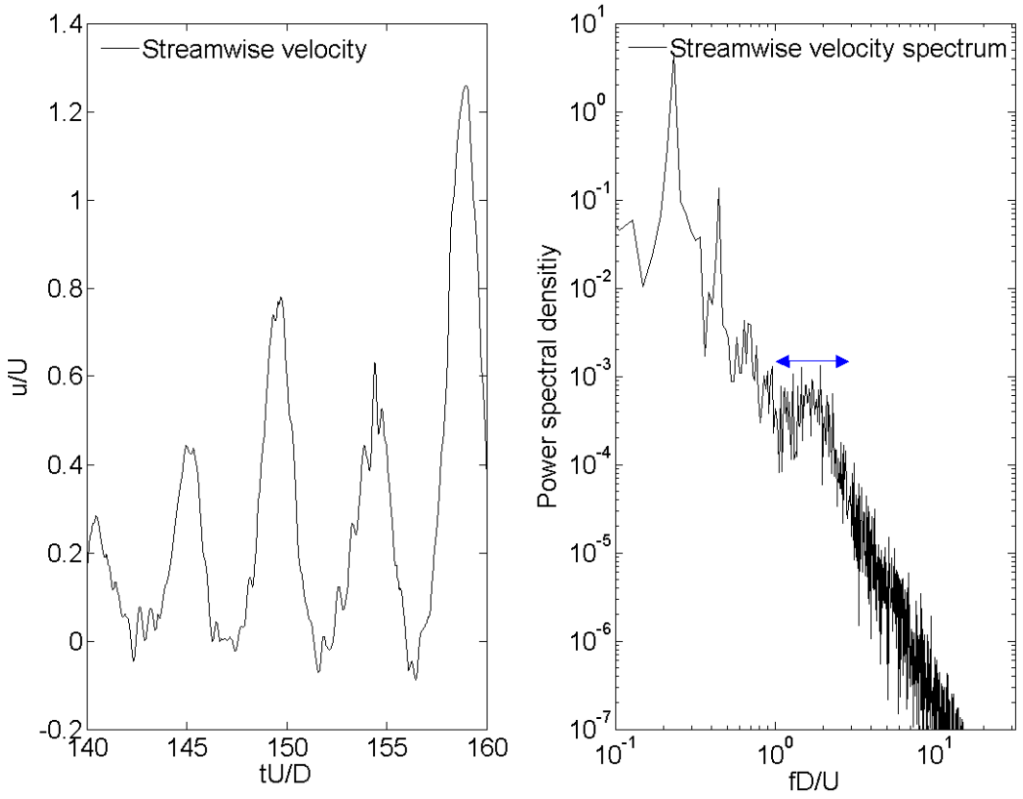

(a) Time trace of instantaneous streamwise velocity u.

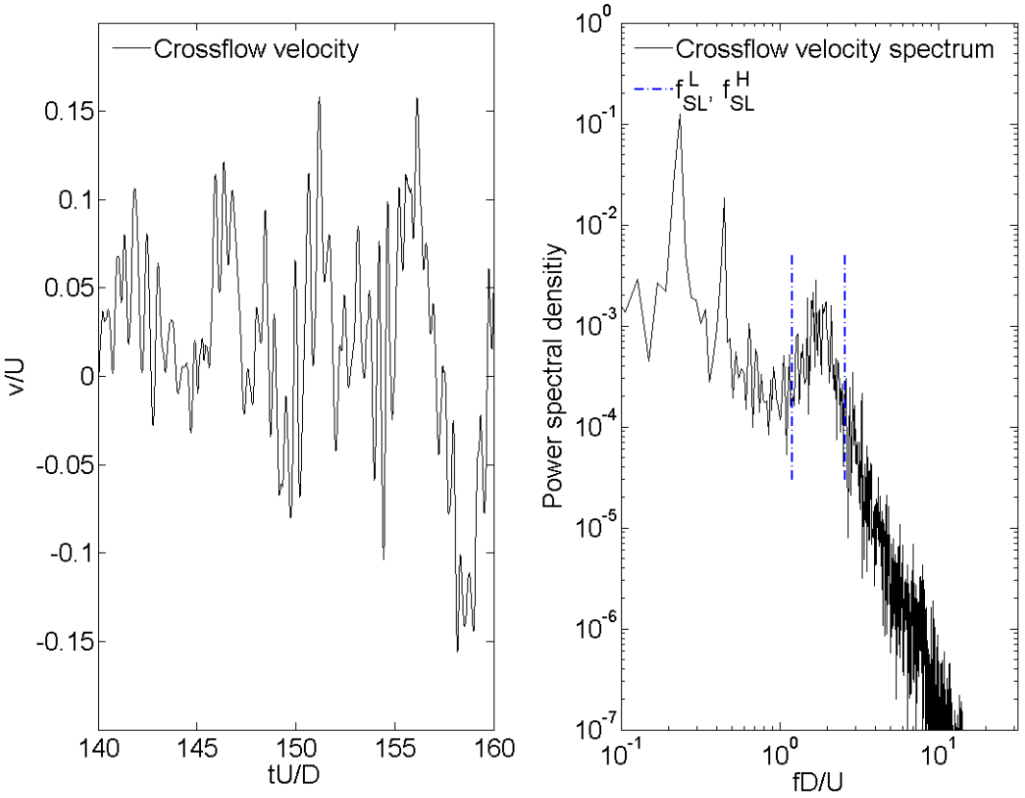

(b) The power spectra of instantaneous crossflow velocity v.

FIGURE 4.7: Time trace of instantaneous velocities (left column) and power spectra of the velocities (right column) at Re=10000: all plots are obtained at the point of $(x/D,y/D)$=(0.50,0.53) around the upper shear layer.

The flow feature of the shear-layer instability at Re=10000 is demonstrated in Figure 4.7. The spectra obtained with streamwise velocity component u at a point of $(x/D,y/D)$=(0.50,0.53) around upper shear-layer adjacent to the cylinder surface shows weak broadband peak at high-frequency. On the other hand, Figure 4.7(b-right) clearly shows the well-defined broadband peak due to the small-scale shear-layer vortices around f_{SL}/f_K=9.844 estimated by Equation 4.1. The corresponding instantaneous crossflow velocity describes the dominance of high-frequency fluctuations, which is comparable to those at the point around the cylinder base as shown in Figure 4.6(b-left).

In the DNS study at Re=10000 conducted by Dong et al. [3], the shear-layer frequency was captured as a plateau or flat spectral peak and the value was estimated as the range of f_{SL}/f_K=7.83 to 15.83, indicating the mean value of 11.83. Their mean result shows reasonably good agreement with the value of 11.2 from the correlation formulation in Equation 4.2. In the present study, however, the predicted shear-layer frequency is slightly lower than both reference values.

Figure 4.8(a) shows comparison of flow spectra at Re=41300 calculated from three different subgrid scale models, the Smagorinsky (SMG), k-equation (TKE) and dynamic k-equation (DTKE) SGS, as summarised in Table 3.8. The flow spectra are obtained at the same point of $(x/D,y/D)$=(0.30,0.57) and show the Kármán and its sub-harmonic frequencies as well as broadband peaks at nearly similar levels of non-dimensional frequencies fD/U. The power spectra exhibit basically identical behaviours with each other. As already indicated in the previous 3-D LES study at Re=8000 performed by Jordan [36], the SGS model itself is not a major contributor to the predicted shear-layer characteristics.

In Figure 4.8(b) the shear-layer frequency at Re=41300 is clearly captured both at the points of $(x/D,y/D)$=(0.30,0.57) and (0.50,0.57). The power spectra are, of course, obtained with the dynamic k-equation (DTKE) model. Upstream, close to the cylinder surface, it seems that the normalised frequency is notable, which is compared with those obtained at $(x/D,y/D)$=(0.50,0.57). The mean value of the dominant shear-layer frequency is f_{SL}/f_K=29.166. However, at the downstream point, f_{SL}/f_K=27.777 is predicted and it is slightly under-estimated compared with the correlation value of 29.090. These are indicated that the frequency of shear-layer vortices is highly sensitive to which level is obtained.

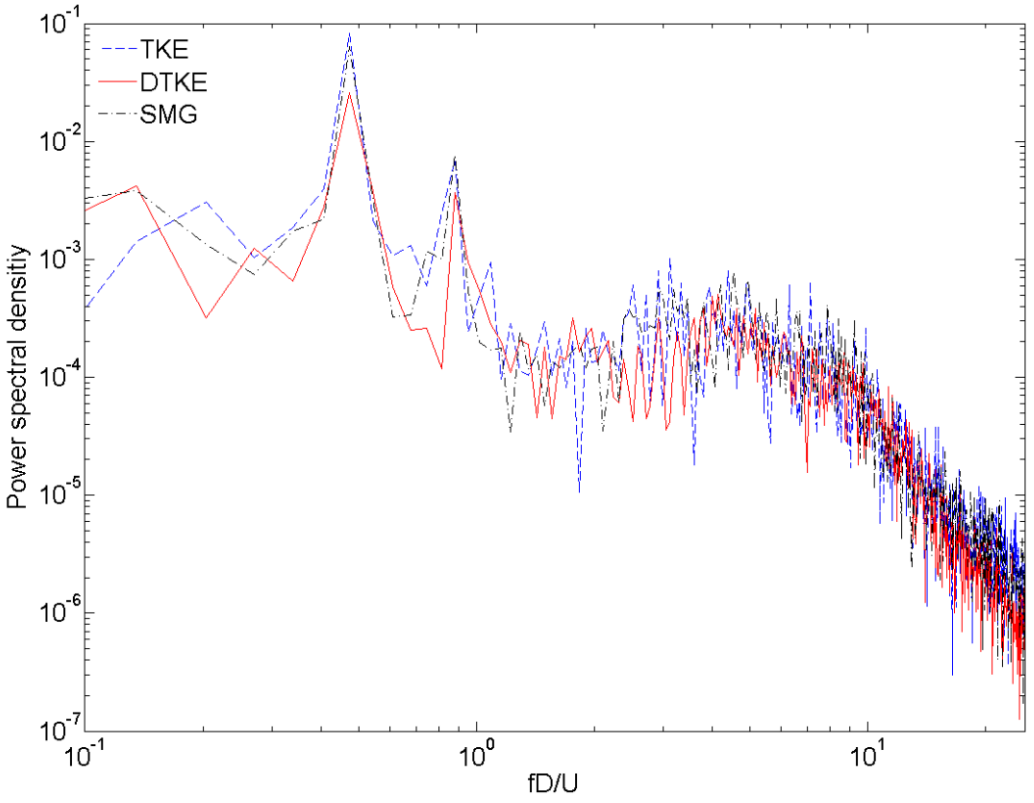

(a) Comparison of the power spectra obtained with three different SGS models: all spectra are obtained at the point of $(x/D,y/D)$=(0.30,0.57).

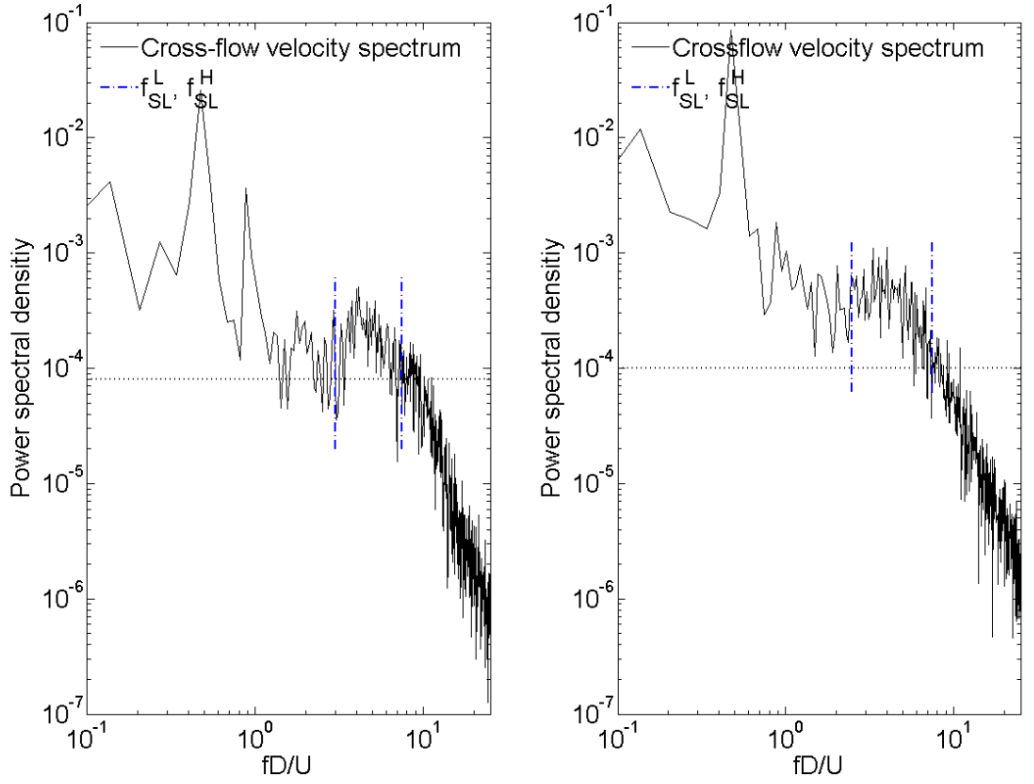

(b) The power spectra of instantaneous crossflow velocity v at $(x/D,y/D)$=(0.30,0.57) on the left and (0.50,0.57) on the right.

FIGURE 4.8: The power spectra obtained with various SGS models (a) and obtained at different positions (b).

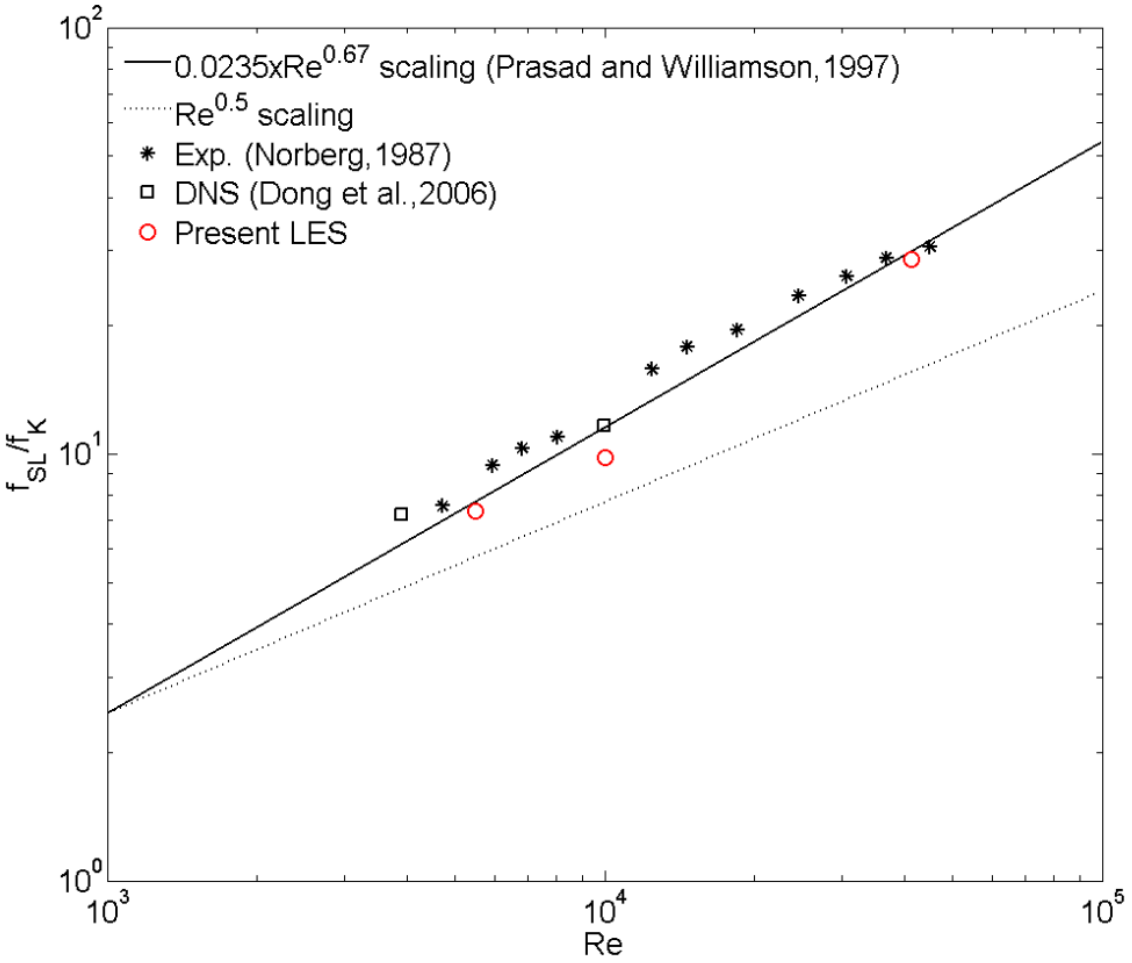

FIGURE 4.9: Variation of the normalised shear-layer frequency with Re=5500-41300.

In Figure 4.9, the mean values of the shear-layer frequencies over Re=5500-41300 are plotted together with previous experimental measurements and DNS data as a function of Reynolds number. The power-law scaling correlations of $Re^{0.5}$ and $Re^{0.67}$ suggested by Bloor [16] and Prasad and Williamson [24] are plotted as references. The predicted normalised frequencies in the present LES study are slightly lower than the experimental measurements; however, the results at Re=5500-41300 clearly exhibit the $Re^{0.67}$ dependence.

4.3 Closure

In this Chapter, the effects of Reynolds number on the statistical features of the cylinder wake and on the shear-layer instability over the transitional flow range have been

examined. All the quantities in 3-D LES were temporally and spatially averaged in the spanwise direction in order to obtain representative and qualitative results.

The flow statistics such as the mean velocity and components of Reynolds stresses were compared with available reference data and clearly showed the notable difference of the near-wake structures with increasing Reynolds number Re=5500-10000, as observed in previous experiments. In addition, the extended numerical study of the flow statistics were examined at the higher Reynolds number of 41300. The present 3-D LES clearly reproduced the principal feature of upstream movements of the flow statistics with increasing Reynolds numbers. The characteristic lengths, e.g. the cluster of the negative velocity in the mean velocity u/U and the velocity fluctuations $u'u'$ fields, reached close to the cylinder base at Re=41300. Simultaneously, the base suction pressure $-C_{pb}$ and force coefficients were increased as the near-wake structures showed the upstream movement. The flow pattern of the normalised shear stress $u'v'/U^2$ described extensions along the edge of the separated shear layer towards the upstream separation point over Re=5500-41300, which suggests earlier onset of transition.

These variations of the near-wake structures with increasing Reynolds number also influence on the shear-layer instability. The velocity spectra around the upper shear layer clearly showed a broadband peak at shear-layer frequency f_{SL} at Re=5500. The broadband peak vanished from the flow spectra around the cylinder base. The instantaneous velocity around the shear layer described the characteristic of the shear-layer velocity with high-frequency low-amplitude fluctuations, which are caused by small-scale shear-layer vortices superimposed on top of large-scale fluctuations caused by Strouhal vortices. At Re=10000, the high-frequency fluctuation dominated the shear-layer velocity and the well-defined broadband peak was displayed at higher frequency as the Reynolds number increased. In addition, it seems that the effects of the SGS models on the shear-layer characteristic are insignificant at Re=41300. The normalised frequency of shear-layer vortices f_{SL}/f_K showed good agreement with previous experimental measurements and it seems that the normalised frequency obtained with the present 3-D LES follows the $\mathrm{Re}^{0.67}$ power law suggested by Prasad and Williamson [24].

Chapter 5

SUBMERGED OSCILLATING CYLINDER

5.1 Introduction

Much of the interest in the flow around a circular cylinder oscillating transversely to a free stream is due to its relevance to vortex-induced vibration, which occurs when a body is placed in a flow and the fluctuating lift force due to the asymmetric formation of Kármán vortices in the wake causes the body to vibrate. Large-amplitude oscillations of the cylinder at frequencies close to the frequency of formation of Kármán vortices can cause significant changes in both the wake structure and the forces on the cylinder.

A common and robust approach to studying vortex-induced vibration is to force the body to oscillate with a predefined motion that approximates the vortex-induced motion. An interesting aspect of the forced oscillation of a cylinder is how it relates to self-excited vibration induced by vortex shedding. Govardhan and Williamson [67] have presented that, as the reduced velocity decreases in self-excited vibration (analogous to an increase in frequency ratio f_e/f_K in forced vibration), the movement of the flow state from the upper or lower branch to the initial branch in self-excited vibration corresponds to a change in the mode of vortex shedding from 2P to 2S in forced vibration. Their self-excited vibration study also observed a change in the timing of vortex shedding which was firstly observed in a forced oscillation study. The changes in the forces and wake modes in vortex-induced vibration appear to have many common features with the simplified cases

where a cylinder oscillations are forced. In the present study, therefore, the controlled vibration of a cylinder is numerically examined to provide a deeper understanding of vortex-induced vibration phenomena for freely vibrating bodies.

Following the pioneering experiments of Bishop and Hassan [26] with a cylinder subjected to forced oscillations in uniform flow, several experiments, including those of Sarpkaya [27], Williamson and Roshko [28], Ongoren and Rockwell [29], Gu et al. [6], Gopalkrishnan [30] and more recently Carberry et al. [4], Morse and Williamson [5], Carberry et al. [7, 31], were conducted using forced oscillation as discussed in the literature review.

The previous literature raises a number of unresolved issues which have motivated the present research. Despite the fact that the forced oscillation of a cylinder has been the subject of a large number of investigations, the properties of the wake states are still not fully defined. The literature indicates that the jump in the lift forces is a universal feature of the oscillating cylinder flow, which occurs over a wide range of amplitude ratios A/D and Reynolds numbers. However, it is not clearly explained how the near-wake structure varies with A/D and Re, or how the transition occurs between two consecutive wake modes or patterns.

In this Chapter, 3-D LES computations of the turbulent flow behind an oscillating circular cylinder are performed for a complete validation of the predicted lift forces on a moving cylinder at the higher Reynolds number of 10000. The resulting forces are compared with the experimental measurement and DNS data at considered Reynolds numbers. Secondly, the universal flow characteristics of an oscillating cylinder flow such as the well-known abrupt jump in lift force with particular focus on the stable wake states are numerically reproduced based the previous literatures. The resulting wake patterns at corresponding frequency ratio f_e/f_K observed in the experiments are calculated by spanwise- and phase-averaging in order to produce qualitative 3-D LES solutions. Finally, the transitional area between two consecutive stable wake states is numerically investigated in a narrow band of excitation frequencies f_e close to Kármán frequency f_K and discussed in detail.

5.2 Validation of 3-D LES Computation of an Oscillating Cylinder

5.2.1 The turbulent flow of an oscillating cylinder at Re=10000

In this section, turbulent flow past a circular cylinder subjected to forced oscillations transverse to the free stream with a constant excitation amplitude A at a series of excitation frequencies of oscillation f_e is numerically studied at Re=10000 for a complete validation of 3-D LES calculation on a moving grid domain.

Based on the careful grid dependence analysis in Chapter 3.3, the simulation case LES-B5 is confidently chosen for an oscillating cylinder flow as shown in Table 3.5. In the case LES-B5, 3,686,400 cells in total were used and the eddy-viscosity type k-equation SGS model was applied to the turbulence flow behind a stationary cylinder. The viscous terms were evaluated using a second-order central differencing method and the non-dimensional time step $\Delta tU/d$=0.001 was used. The brief description of the geometry is shown in Figure 5.1

The cylinder displacement is defined as sinusoidal oscillations $y(t)=A\sin(2\pi f_e t)$ and a set of non-dimensional frequencies $0.15\leq f^*(=f_eD/U)\leq 0.27$ is considered with a moderate amplitude ratio A/D=0.3. The parameter set is based on the previous experiment by Gopalkrishnan [30] and the DNS simulation by Dong et al. [3] conducted at the same

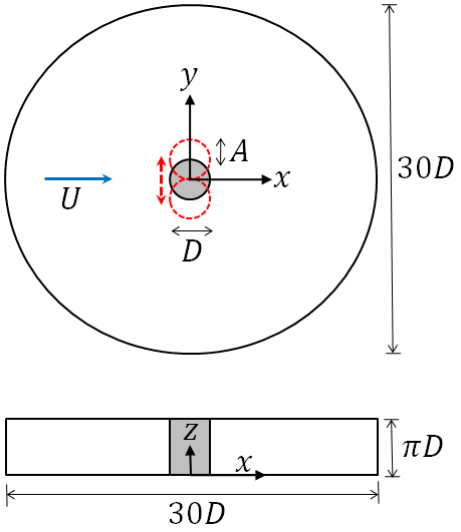

FIGURE 5.1: The physical solution domain: cylinder oscillating transverse to the free stream.

Reynolds number in order to reproduce their observation of a sharp increase of force coefficient around a certain non-dimensional frequency.

As discussed in previous section 2.3.8, the grid points on the wall of the cylinder are calculated explicitly according to the prescribed sinusoidal motion of the cylinder, and the resulting mesh deformation and quality are accounted for using a Laplace equation where a quadratic diffusion parameter γ controls the displacement of the internal mesh points.

In order to gather more qualitative numerical results compared to the stationary cylinder case, the simulation time is extended up to a non-dimensional time of tU/D=500. Therefore, the CPU time for each simulation case of an oscillating cylinder is approximately 500h in general, which is comparable with ≈200h for a stationary cylinder.

Figure 5.2 shows time histories of the force coefficients and the cylinder motion at a typical frequency value of f^*=0.18. The cylinder is starting oscillations from rest at tU/D=0, corresponding to the beginning of the force traces. The amplitude of the oscillations is held constant at A/D=0.3. It is noted that the oscillating wake appears to be fully established in fewer than about 10 oscillations or over tU/D=70 as marked in the blue dashed line.

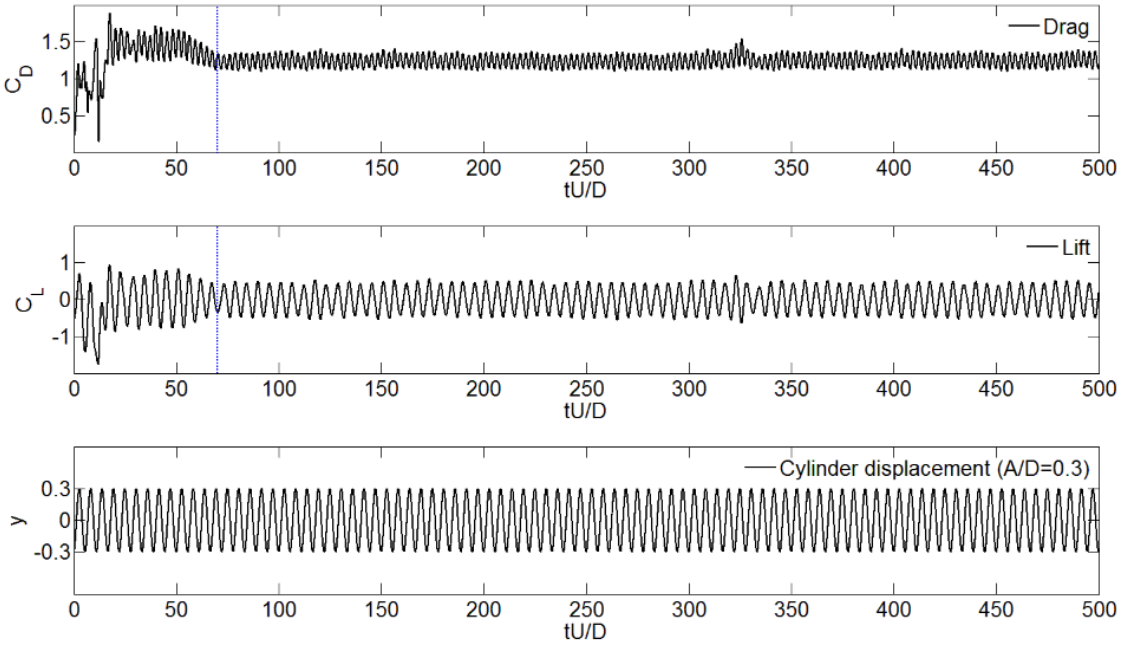

FIGURE 5.2: Time histories of force coefficients C_D and C_L, and displacement $y(t)$ of an oscillating cylinder excited with f^*=0.18 and A/D=0.3 at Re=10000 (LES-B5).

5.2.2 Hydrodynamic coefficients of an oscillating cylinder

The lift magnitude and lift phase ϕ_L are shown with respect to non-dimensional frequency f^* in Figure 5.3(a,b), together with the experimental values obtained from Gopalkrishnan [30] and DNS data from Dong et al. [3]. In Figure 5.3(a), the well-known sharp jump of lift properties is calculated when the excitation frequency f_e is approaching close to the natural shedding frequency $f_K \approx 0.2$ at Re=10000. The sharp jump of both lift and phase angle is captured at $f^*=0.19$ in the present simulations, while the experimental data showed that the jump occurred at $f^*=0.18$ for lift. The DNS data also shows the abrupt jump around $f_e/f_K \approx 1.0$, but it seems that the number of DNS data points is not enough to decide where the jump occurs. It might be due to limitation of high computational resources. The difference between the present LES and the experiment may come from the different setup between the experiment and the computation. The overall behaviour of lift properties shows good agreements with the experimental measurements and DNS data. However, the predicted values from LES are slightly under-estimated.

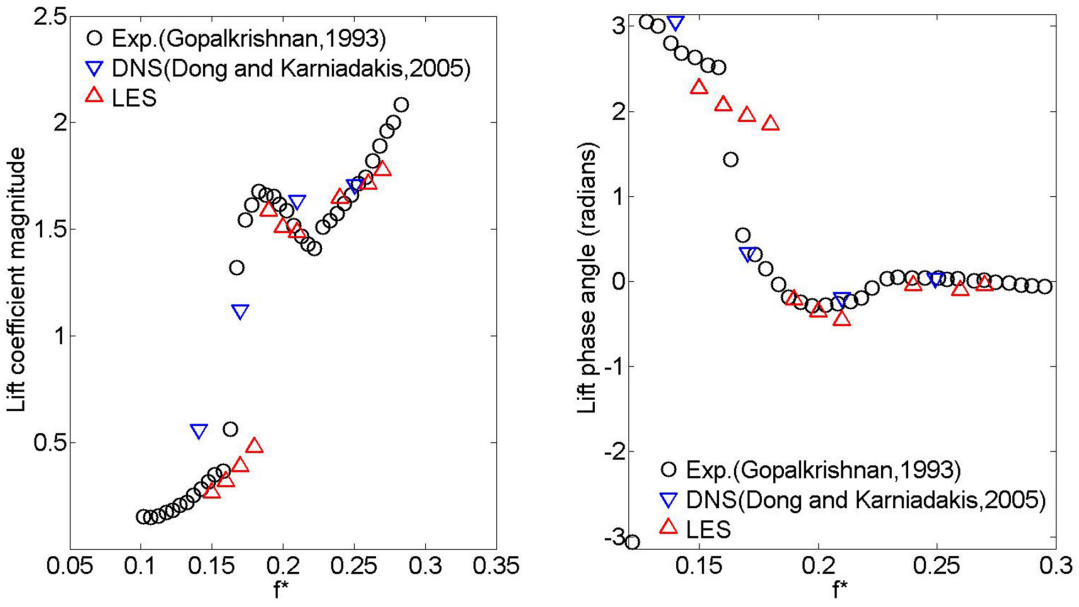

(a) Lift coefficient magnitude.

(b) Phase angle of lift ϕ_L.

FIGURE 5.3: Comparative lift properties of an oscillating cylinder flow, lift coefficient magnitude and phase with respect to the cylinder displacement, as a function of non-dimensional frequency f^* at Re=10000.

When the cylinder motion is synchronised with the vortex formation, the cylinder displacement $y(t)$ and total fluid lift forcing $C_L(t)$ are accurately represented by sinusoidal functions:

$$C_L(t) = C_L \sin\left(2\pi f_e t + \phi_L\right), \tag{5.1}$$

where ϕ_L is the phase of the lift coefficient with respect to the cylinder displacement. Figure 5.3(b) shows the behaviour of lift phase angle ϕ_L. At lower frequencies, the lift phases are under-predicted compared to the experimental measurements. The predicted phase values, however, are well-approximated after the abrupt jump of lift magnitude $f^* \geq 0.2$.

Govardhan and Williamson [67] were the first to describe the consequences of force decomposition, into vortex and apparent mass components, in the interpretation of the phase and amplitude of the lift force on a freely vibrating cylinder. Their decomposition is:

$$F_{total} = F_{vortex} + F_{am}, \tag{5.2}$$

where the apparent mass force is given by:

$$F_{am}(t) = -\frac{\rho\pi D^2}{4}\frac{\mathrm{d}^2 y}{\mathrm{d}t^2}, \tag{5.3}$$

where y is the cylinder displacement. The normalised apparent mass is in phase with the motion of the cylinder:

$$C_{Lam}(t) = \frac{F_{am}(t)}{\frac{1}{2}\rho U^2 L D}, \tag{5.4}$$

The normalised vortex lift coefficient $C_{L\mathrm{vortex}}(t)$ is calculated by subtracting $C_{Lam}(t)$ from total lift $C_L(t)$. Therefore, the vortex lift is now expressed in the same way as the total lift:

$$C_{L\mathrm{vortex}}(t) = C_{L\mathrm{vortex}} \sin\left(2\pi f_e t + \phi_{L\mathrm{vortex}}\right), \tag{5.5}$$

where $\phi_{L\mathrm{vortex}}$ is the phase of the lift coefficient due to the vorticity in the wake.

The classical expression for the added mass coefficient C_{EA} is given as the following by Gopalkrishnan [30]:

$$C_{EA} = -\frac{1}{2\pi^3}\frac{C_{Lacc}}{(A/D) f_e}, \tag{5.6}$$

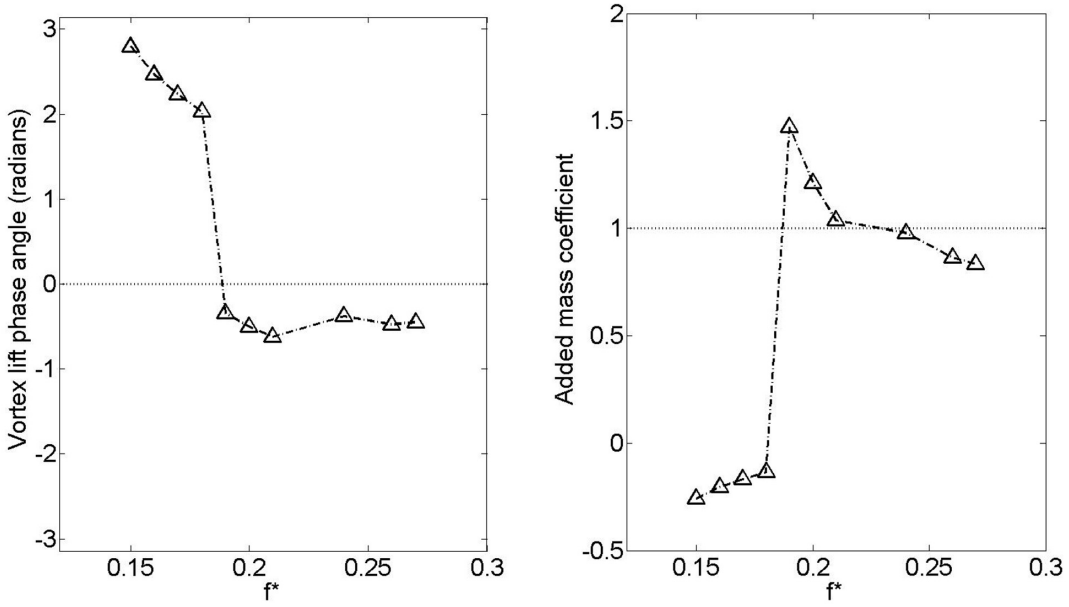

(a) Vortex lift phase.

(b) Added mass coefficient.

FIGURE 5.4: Vortex lift phase $\phi_{L\text{vortex}}$ and added mass coefficient C_{EA} as a function of non-dimensional frequency f^* at Re=10000.

where the component of the lift coefficient in phase with acceleration is expressed as:

$$C_{Lacc} = -C_L \cos(\phi_L), \tag{5.7}$$

Figure 5.4(a,b) shows the variation of vortex lift phase $\phi_{L\text{vortex}}$ and the effective added mass coefficient C_{EA} as a function of non-dimensional frequency. In Figure 5.4(a), the overall variation of vortex lift phase is very similar to those of ϕ_L, but the vortex lift phase is much more out-of-phase with the cylinder displacement as f^* increases after the jump than the corresponding lift phase.

In Figure 5.4(b), the effective added mass coefficient, which includes an apparent mass effect due to the transverse fluid force in-phase with the cylinder acceleration, is represented by negative added mass at lower values of non-dimensional frequencies. As the frequency increases, there is the sharp jump of the inertia fluid force at the resonant point as expected. After the peak point, the added mass coefficient for the cylinder decreases to around unity, which is the classical value of added mass for a circular cylinder.

5.3 Stable Wake States

In the previous section 5.2, the comparison study with the experimental and DNS data for the forced oscillation indicated that the present 3-D LES simulation has captured the physical quantities such as the fluctuating lift coefficient and the lift force phase angle fairly well at the higher Reynolds number of 10000, while the LES calculations predicted that the well-known abrupt jump of lift force occurred slightly later than with the experimental data.

In this section, numerical study of the turbulent wake of an oscillating cylinder is conducted at a range of Reynolds numbers Re=5500-10000 in detail. For the present controlled vibration study, the simulation case LES-B3 is confidently used for Re=5500, based on the previous validation study at the higher Reynolds number of 10000. As discussed in section 3.2, for achieving the grid independence, the computational grid resolution of LES-B3, with a total of 3.11M cells with high resolution of N_z=96 along the cylinder axis-direction, was chosen as the minimum. The conventional Smagorinsky SGS model on the grid resolution predicted the hydrodynamic forces and pressure coefficients reasonably well.

5.3.1 General flow features of an oscillating cylinder

The frequency dependence of the near wake of a cylinder undergoing forced oscillations transverse to the free stream is examined in more details. As discussed in the literature review, both the near-wake structure and the lift force on an oscillating cylinder are known to exhibit abrupt changes as the frequency of oscillation passes through the natural frequency of the stationary cylinder wake. According to the previous experimental observations, therefore, the relationship of the lift force and near-wake structure is numerically investigated at Re=5500.

The 3-D LES calculations are performed at a range of frequency ratios, $0.75 \leq f_e/f_K \leq 0.95$, with a constant and moderate amplitude ratio A/D=0.50. The parameters of the frequency ratios are based on the experimental observations obtained from Gu et al. [6] at Re=5000 with the goal of reproducing a close approximation of the experimental result measured by Carberry et al. [4].

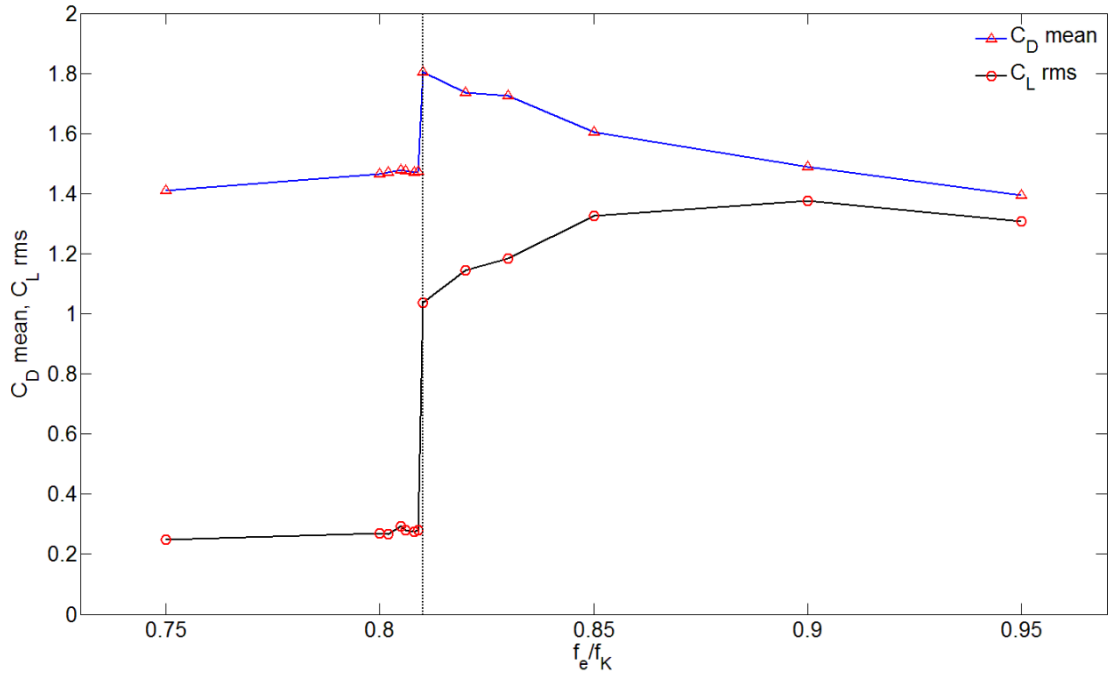

(a) Variations of the mean drag and r.m.s. lift coefficients.

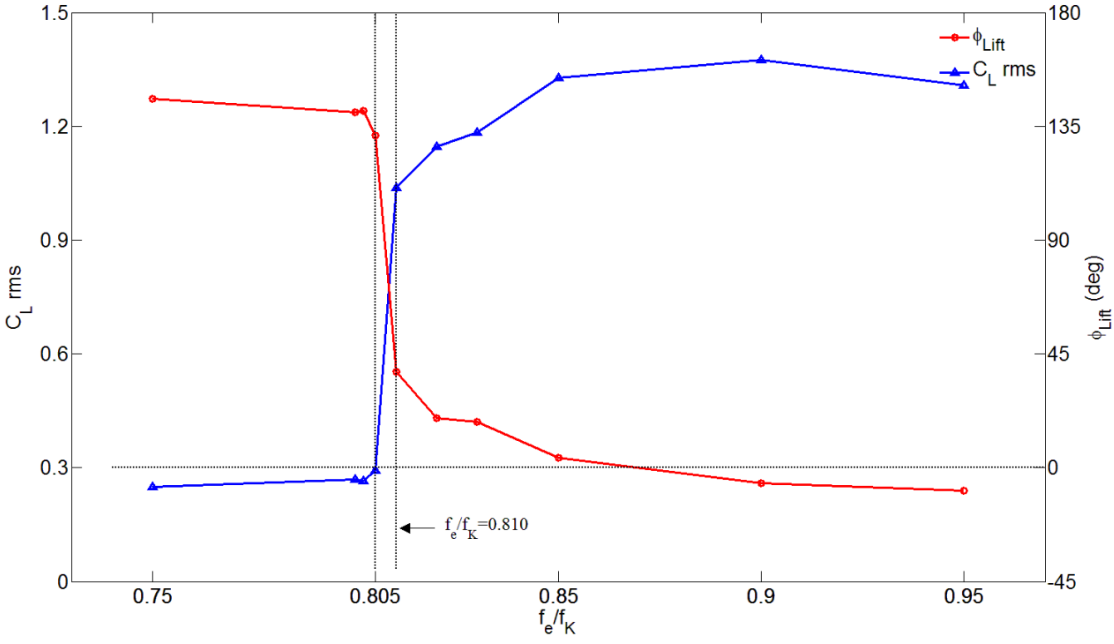

(b) Variations of the amplitude and phase of lift.

FIGURE 5.5: Overall behaviours of hydrodynamic forces and phase angle of lift as a function of frequency ratio f_e/f_K: A/D=0.5 and Re=5500.

The variations of the mean drag coefficient $\bar{C_D}$ and the r.m.s. lift coefficient C'_L are presented in Figure 5.5(a). At low oscillation frequencies below the jump, the predicted values of the force coefficients exhibit relatively small values, close to the stationary

cylinder value in the case of C'_L=0.243 for a stationary cylinder. The abrupt and sharp amplification peaks of the drag and lift occur at a particular value of non-dimensional frequency f_e/f_K=0.810, slightly below the natural Kármán frequency f_K. At f_e/f_K increases further, the mean drag displays very similar values before the sharp jump, whereas the lift coefficient gradually increases. Figure 5.5(b) shows the variation of the lift and phase angle ϕ_L with respect to the cylinder motion. At the particular frequency ratio f_e/f_K=0.810, there is simultaneously an abrupt increase in C'_L and a shift in ϕ_L from ≈150° to ≈0°, which are consistent with those found by previous experiments.

Figure 5.6 shows the time trace of the drag and lift coefficients with the cylinder displacement $y(t)$. The drag coefficient exhibits relatively large fluctuations at f_e/f_K=0.750, while the lift coefficient shows low fluctuations. The lift coefficient is nearly out-of-phase with the sinusoidal cylinder motion. As frequency ratio increases to f_e/f_K=0.950, the drag shows relatively lower fluctuations, whereas the fluctuation of the lift is much larger and nearly in-phase with the cylinder displacement.

Figure 5.7 displays the time trace of the force coefficients, especially on either side of the abrupt jump. As the frequency ratio increases from 0.805 to 0.810, the drag and lift coefficients show abrupt changes within the narrow frequency band. It is also noted that the lift is nearly in-phase with the cylinder displacement.

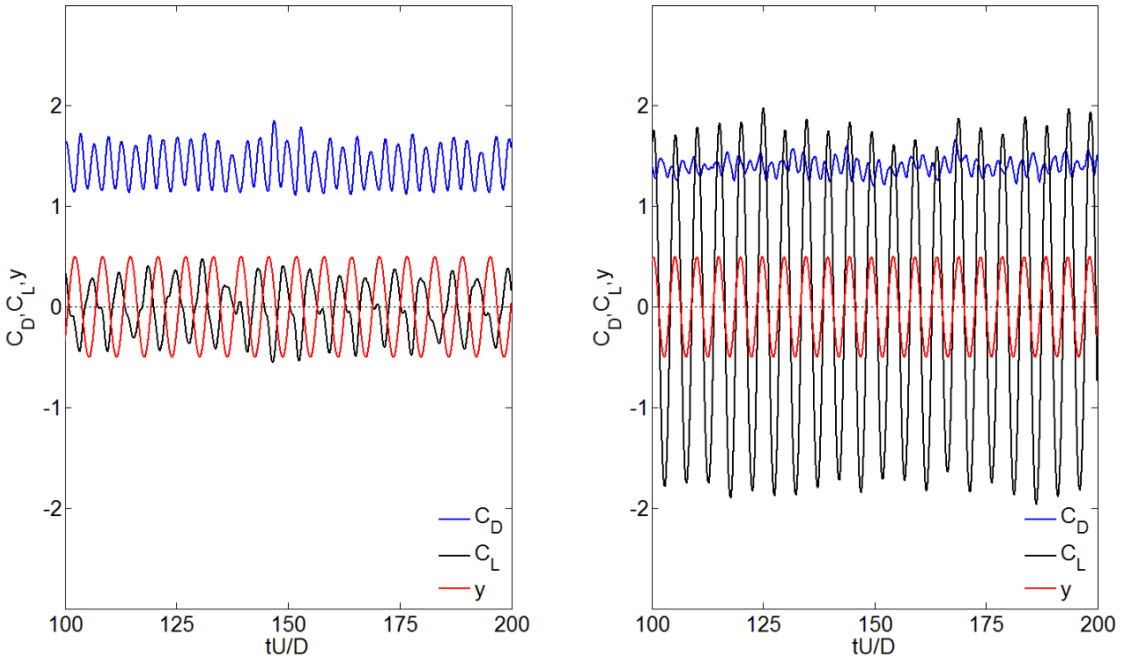

FIGURE 5.6: Time history of the force coefficients and the cylinder displacement at two end points of f_e/f_K=0.750 (left) and 0.950 (right): A/D=0.5 and Re=5500.

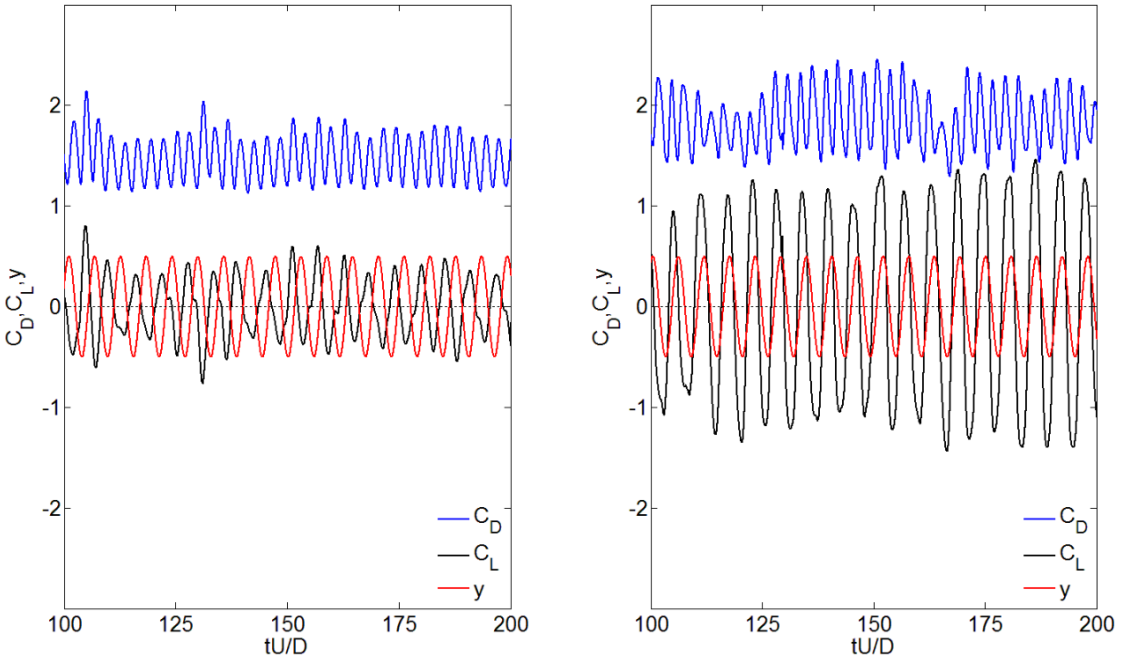

FIGURE 5.7: Time history of the force coefficients and the cylinder displacement on either side of the jump at f_e/f_K=0.805 (left) and 0.810 (right): A/D=0.5 and Re=5500.

In the controlled vibration experiment, Carberry et al. [4] clearly identified these two different behaviours of the lift properties on either side of the sharp change as the low- and high-frequency wake state respectively. Therefore, the behaviour of the lift properties in $0.750 \leq f_e/f_K \leq 0.805$ and $0.810 \leq f_e/f_K \leq 0.950$ could be described as the low-frequency state before transition and the high-frequency state after transition respectively. The present numerical study at Re=5500, therefore, indicates that the transition between the low- and high-frequency states occurs in a very narrow frequency ratio band between $0.805 < f_e/f_k < 0.810$ and A/D=0.5.

5.3.2 Amplitude and Reynolds effects on hydrodynamic coefficients

The amplitude and Reynolds number effects of an oscillating cylinder on hydrodynamic force coefficients are numerically examined at Re=5500-10000. At Re=5500, the numerical results obtained with two amplitude ratios A/D=0.50 and 0.75 within a frequency range $0.75 \leq f_e/f_K \leq 0.95$ are presented in Figure 5.8. Figure 5.8(a) shows the variation of the mean drag coefficient. The overall behaviours of the drag coefficients with A/D=0.50 and 0.75 are similar. As A/D increases, the magnitudes of the mean drag is also shifted upward and the position of the peak is shifted to higher frequency ratio

from f_e/f_K=0.810 to 0.854. The lift is also experienced with an upwind shift as A/D increases.

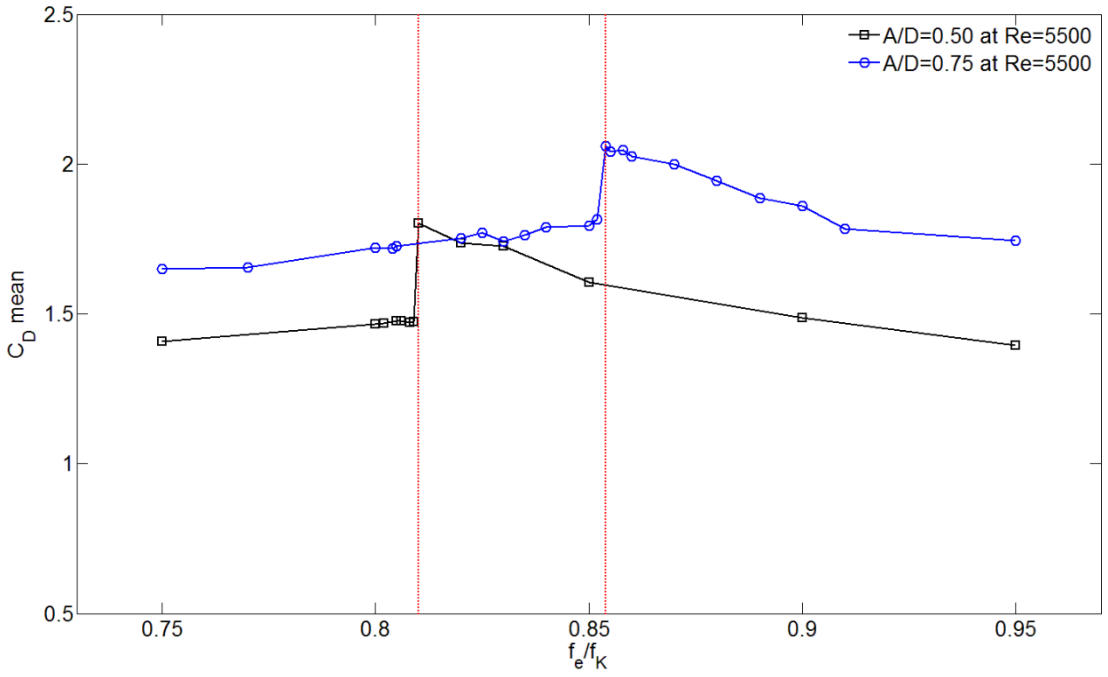

(a) Variations of the mean drag coefficient at A/D=0.50 and 0.75.

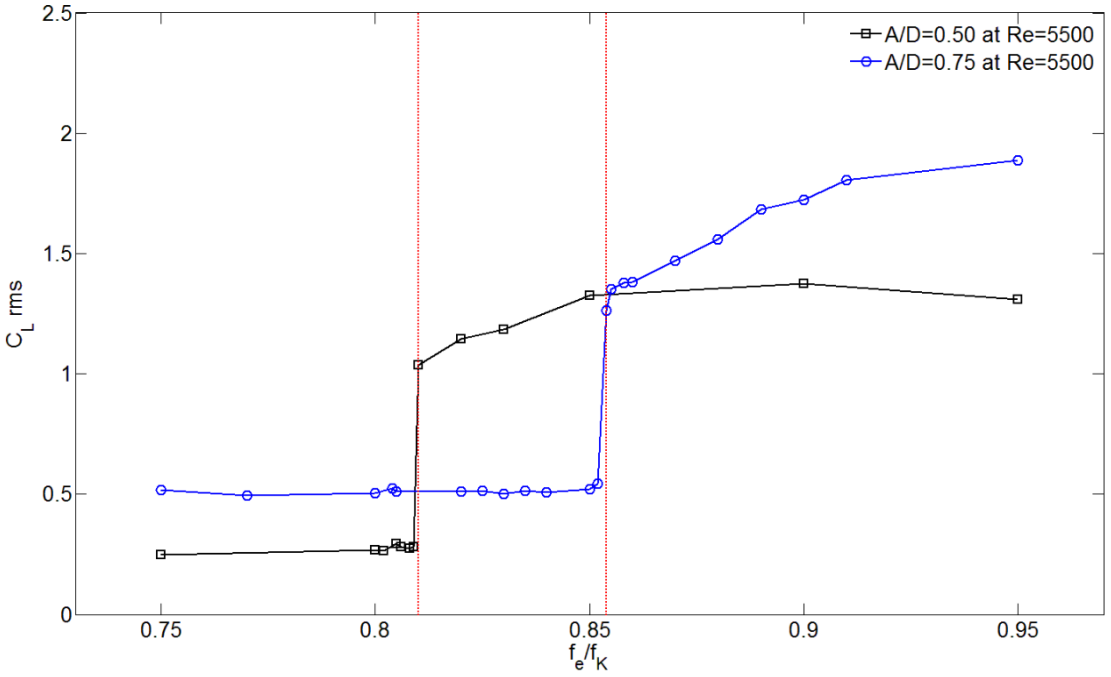

(b) Variations of the r.m.s. lift coefficient at A/D=0.50 and 0.75.

FIGURE 5.8: Overall behaviours of hydrodynamic force coefficients $\bar{C_D}$ and C'_L with different amplitude ratios A/D=0.50 and 0.75 as a function of frequency ratio f_e/f_K at Re=5500.

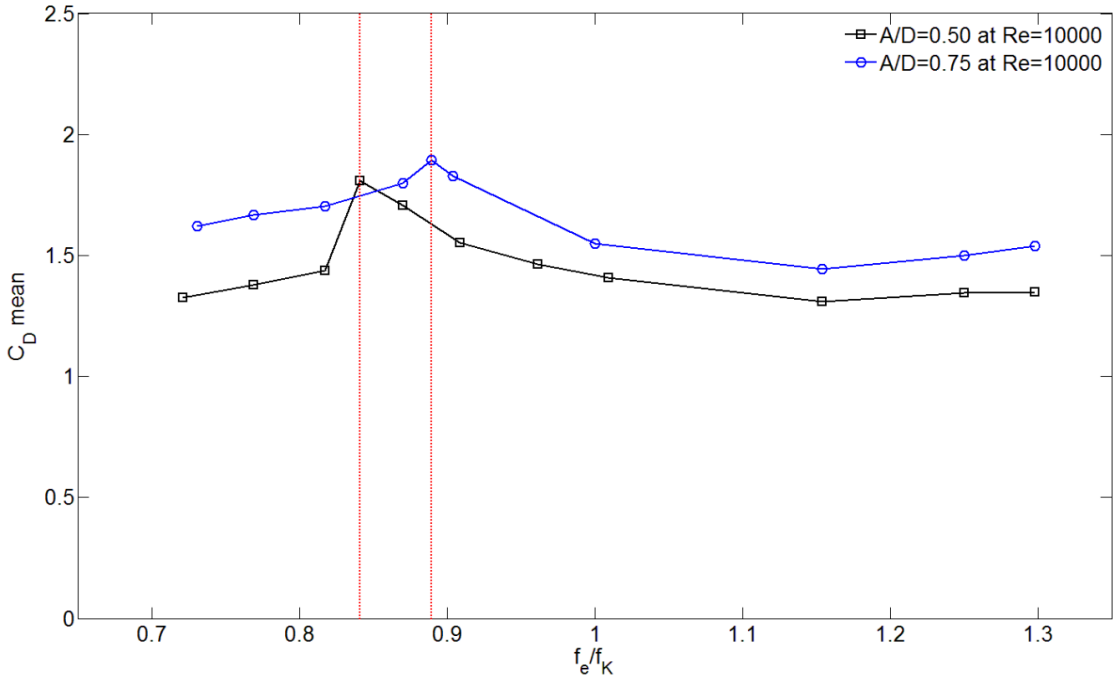

(a) Variations of the mean drag coefficient at A/D=0.50 and 0.75.

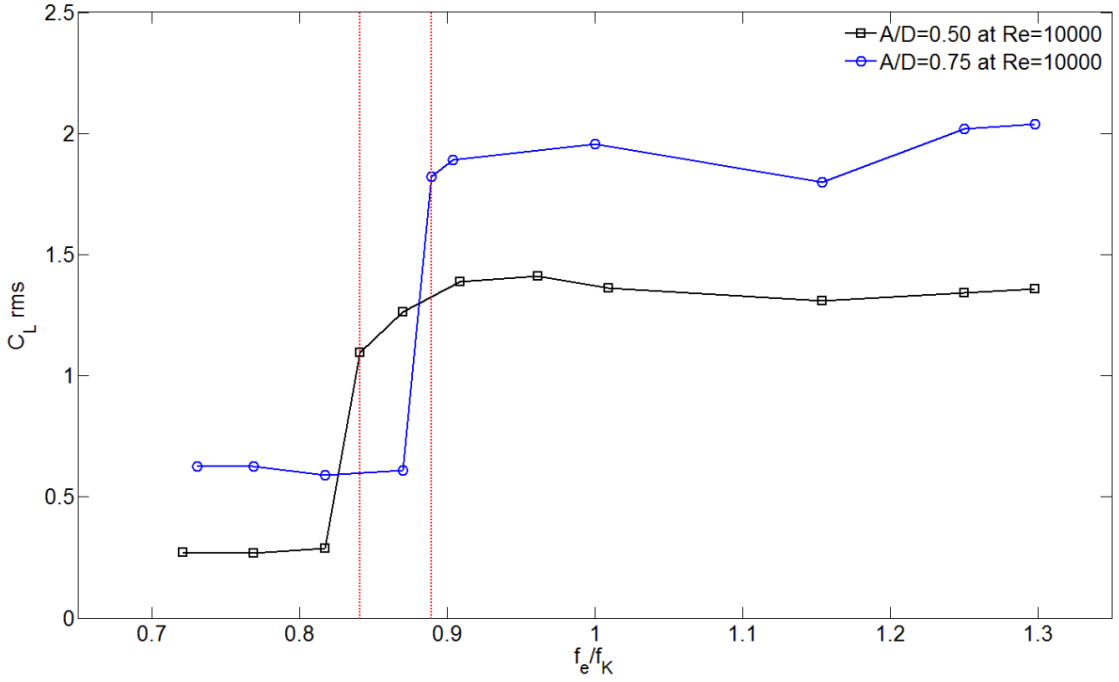

(b) Variations of the r.m.s. lift coefficient at A/D=0.50 and 0.75.

FIGURE 5.9: Overall behaviours of hydrodynamic force coefficients $\bar{C_D}$ and C'_L with different amplitude ratios A/D=0.50 and 0.75 as a function of frequency ratio f_e/f_K at Re=10000.

TABLE 5.1: Summary of hydrodynamic force coefficients at Re=5500-10000

LES case		F_{tr}	$\bar{C_D}$[1]	C'_L[1]
Re=5500	A/D=0.50	f_e/f_K ~0.81	1.8033	1.0378
	A/D=0.75	f_e/f_K ~0.86	2.0473	1.3788
Re=10000	A/D=0.50	f_e/f_K ~0.84	1.8080	1.0958
	A/D=0.75	f_e/f_K ~0.88	1.8952	1.8210

[1] The force coefficients are obtained at the corresponding transitional frequency ratio F_{tr}.

In Figure 5.9, the frequency ratio is more extended above f_e/f_K=1.0 at Re=10000. The drag coefficient exhibits a broad peak at the point corresponding to the jump in the lift. As A/D increases, the transitional frequency ratio in which the jump occurs F_{tr} is shifted close to f_e/f_K=1.0 and the peak values at the corresponding F_{tr} are shifted upward as expected.

Table 5.1 shows the characteristic values of hydrodynamic force coefficients in the present study. As the Reynolds number increases with high amplitude ratio of 0.75, the mean drag tends to decrease where the abrupt jump occurs, whereas the lift coefficient exhibits more fluctuations. The Reynolds number also influences the jump at F_{tr}. As the Reynolds number increases while holding the same amplitude ratio, transitional frequency is slightly delayed. Therefore, it is clear that the two main parameters of forced oscillations, A/D and Re, influence the timing of resonance of the cylinder.

5.3.3 Instantaneous and averaged vorticity fields in stable wake states

The plots in sections 5.3.1 and 5.3.2 clearly described that the lift force has a small amplitude and is approximately out-of-phase with the cylinder displacement at lower values of f_e/f_K. As f_e/f_K increases at a particular value of transitional frequency F_{tr}=f_e/f_K, there is simultaneously a sharp increase in the lift and an abrupt phase shift to around 0°. As f_e/f_K increases further throughout f_e=f_K, the lift and phase change gradually. The drag coefficient shows a broad peak at F_{tr} , but it does not vary significantly with increasing f_e/f_K. These numerical results show fairly good agreements with previous experimental observations. As A/D and Re increase, the transitional frequency F_{tr} is slightly delayed to f_e=f_K and the lift shows more fluctuations. Carberry et al. [4] firstly identified these two different behaviours of the lift properties on either side of

the sharp change as the low- and high-frequency wake states. According to the previous experimental study, the two different behaviours of the lift properties at Re=5500, $0.750 \leq f_e/f_K \leq 0.805$ and $0.810 \leq f_e/f_K \leq 0.950$, could be described as the low-frequency state before transition and the high-frequency state after transition respectively.

Figures 5.10 and 5.11 show the instantaneous and representative vorticity contours within the low- and high-frequency states at Re=5500 when the location of the oscillating cylinder is at its extreme upper position of the cylinder displacement. Figure 5.10 depicts the near-wake structure at f_e/f_K=0.75 and 0.80 before transition while C_L' is small and approximately out-of-phase with the cylinder oscillation. At this low-frequency state, the vortex structure of the upper side of the cylinder is formed from the attached shear layer and the length of the structure extends across the back of the cylinder. As f_e/f_K increases to the high-frequency state after transition, as shown in Figure 5.11, the initially elongated vortex structure attached to the upper side of the cylinder moves closer to the cylinder base and reaches the limiting position while the amplitude of C_L becomes large and approximately in-phase with the cylinder oscillation at this high-frequency state. Whilst the upper vortex structure has rolled up tightly

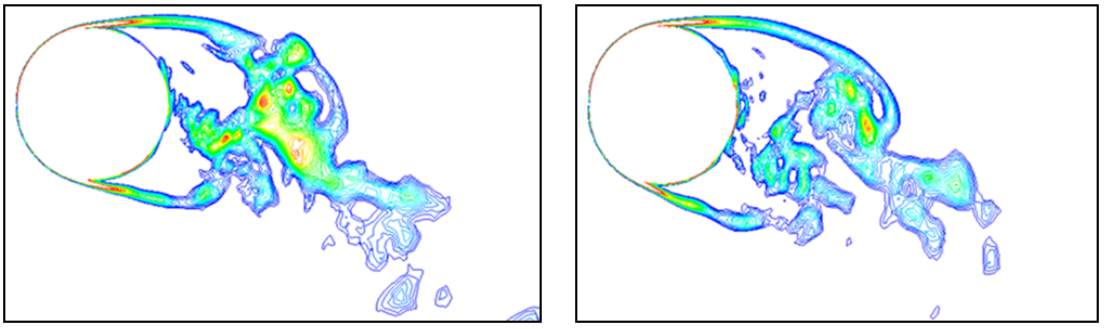

FIGURE 5.10: Instantaneous vorticity magnitude at f_e/f_K=0.75 (left) and 0.80 (right) in low-frequency state at A/D=0.5 and Re=5500: $6 \leq |\omega| D/U \leq 30$, z/D=2.6.

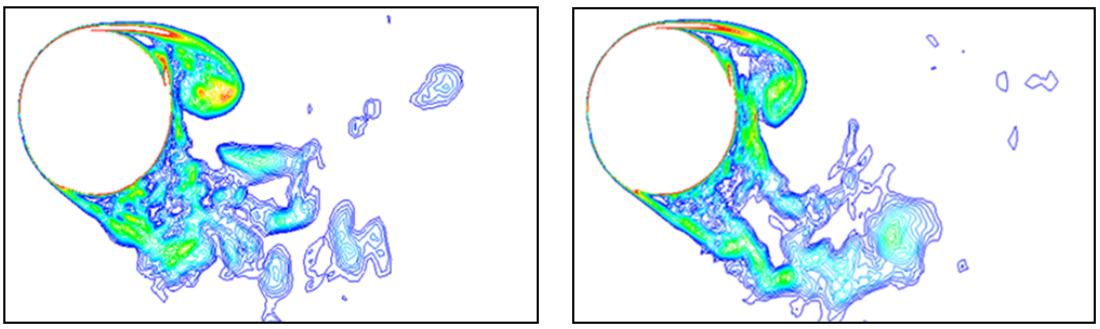

FIGURE 5.11: Instantaneous vorticity magnitude at f_e/f_K=0.85 (left) and 0.90 (right) in high-frequency state at A/D=0.5 and Re=5500: $6 \leq |\omega| D/U \leq 30$, z/D=2.6.

behind the cylinder, the streamwise length of the vortex structure of the lower side of the cylinder starts to extend in the streamwise direction as f_e/f_K increases to 0.90. Therefore, the change of near-wake structure is associated with the changes of lift properties and the vortex switching process in the present 3-D LES study is consistent with the experimental observation of Gu et al. [6] at Re=5000, as discussed in section 1.3.1.

The phase- and spanwise-averaged vorticity fields in Figure 5.12(a,b) show two distinctly different near-wake structures for the values of frequency ratio on either side of the transition at A/D=0.5 and Re=1000. In Figure 5.12(a,left), the characteristics of low-frequency wake state is clearly described as low amplitude of lift and out-of-phase with

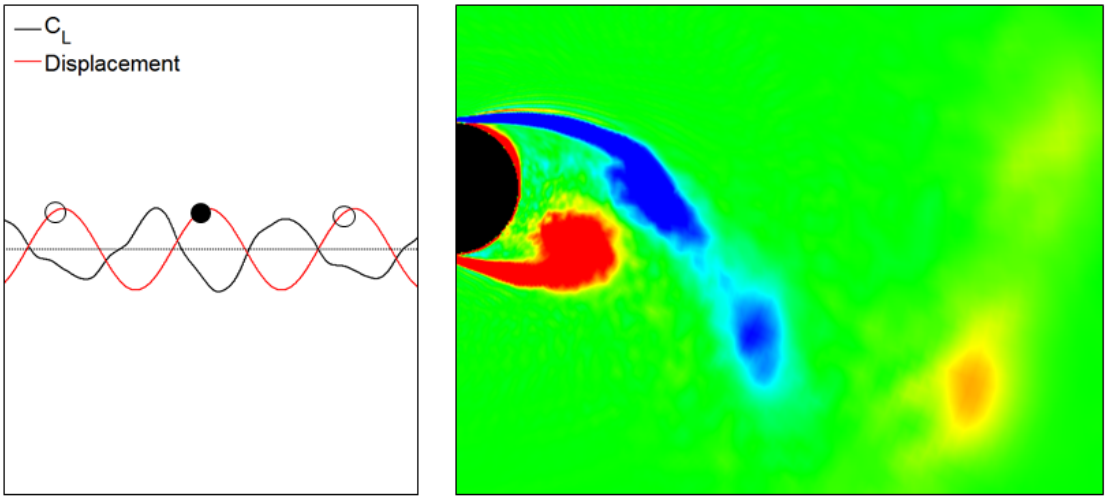

(a) Lift, displacement (left), and corresponding vorticity structure (right) at f_e/f_K=0.817.

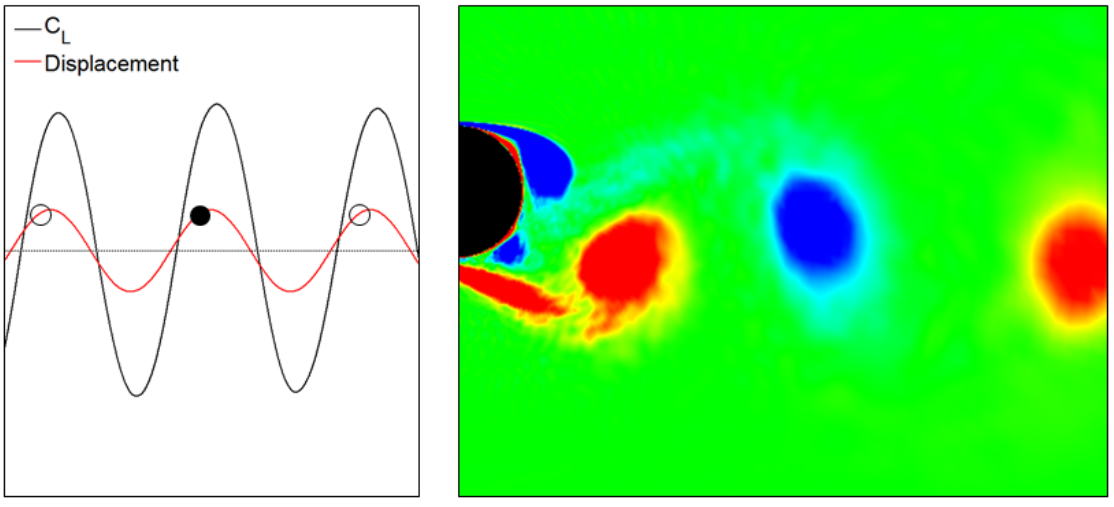

(b) Lift, displacement (left), and corresponding vorticity structure (right) at f_e/f_K=1.009.

FIGURE 5.12: Phase- and spanwise-averaged vorticity fields at A/D=0.5 and Re=10000: the plots are phase-averaged over 5 cycles and obtained where the cylinder is approaching the top of the cylinder's motion.

the cylinder motion. The spanwise-averaged vorticity field is obtained near the top of the cylinder oscillation cycle and the field is additioanlly phase-averaged over the same phase of cylinder oscillations. At the near-peak point, the averaged near wake exhibits the 2P mode of vortex shedding, the shedding of two counter-rotating pairs. Figure 5.12(b) is representative of the near-wake structure in the high-frequency wake state, characterised by high amplitude of lift and in-phase with the motion, showing the formation of the classical Kármán street. This shedding mode is described as the 2S wake mode following the terminology of Williamson and Roshko [28].

The wake modes on either side of the transition are now considered in more detail. Spanwise-averaged vorticity fields at A/D=0.5 and Re=5500 are shown in Figure 5.13(a,b) for low- and high-frequency wake states respectively. In Figure 5.13(a), the cylinder moves through the top of the cylinder motion as time increases. As the cylinder is reaching the top, the attached negative shear layer is extended to the cylinder base. When the cylinder moves downward from the top, the break in the upper shear layer is numerically captured and a portion of the negative vorticity starts to separate from the end of the longer upper shear layer. In Figure 5.13(a), the negative vortex structure forms very close to the cylinder surface in contrast to the low-frequency wake mode. As the cylinder is moving downward through the top of the cylinder displacement, the negative vortex is starting to shed and at this point the positive structure is just shed into the near wake.

Figure 5.14 shows the evolution of the two wake modes in the low- and high-frequency states at A/D=0.3 and Re=10000. At the bottom of the oscillation cycle as shown in Figure 5.14(a), the low-frequency wake mode has a long positive vortex structure extending across the cylinder base. As the cylinder moves up toward the top, the positive structure is separated from the lower shear layer and eventually forms a second counter-rotating pair with a portion of the negative structure from the upper shear layer. In the middle of the oscillation, the splitting of the positive shear-layer into two separate structures is a key step in the formation of the 2P wake mode. It is noted that, at a higher amplitude ratio, the splitting of the extended shear layer into two separate structures and the resulting wake mode is quite pronounced as shown in Figure 5.12(a) captured at A/D=0.5 and the same Reynolds number of 10000. Figure 5.14(b)shows the high-frequency wake states and the wake mode is essentially unchanged as A/D and

Re are varied. At the bottom and top of the oscillation cycle, the negative and positive vortex structures are shed into the near wake.

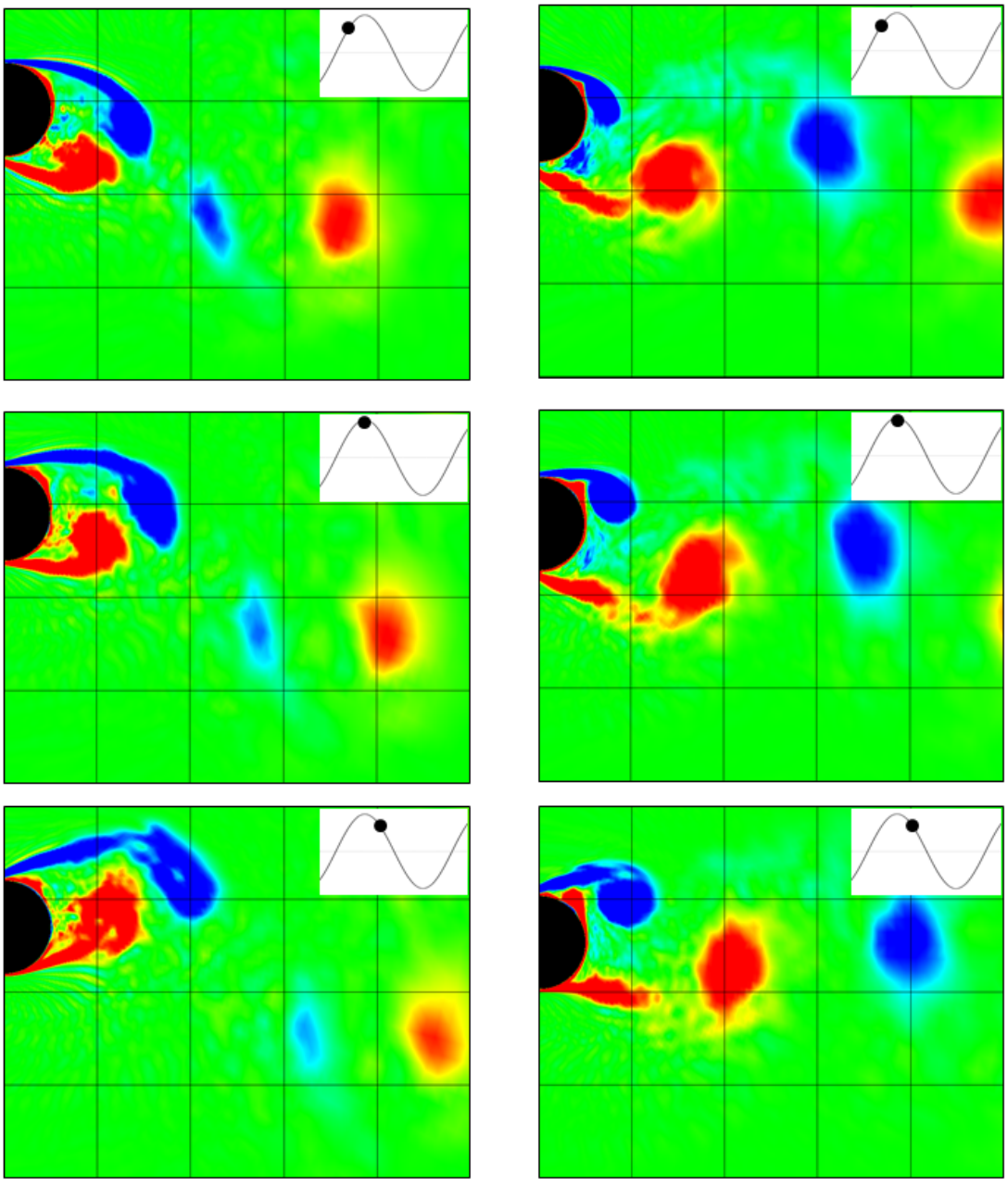

(a) Low-frequency wake modes at f_e/f_K=0.800.

(b) High-frequency wake modes at f_e/f_K=0.900.

FIGURE 5.13: Spanwise-averaged vorticity fields at A/D=0.5 and Re=5500: the images are obtained at evenly spaced intervals near the extreme maximum point of the cylinder displacement: the contour level is -0.5$\leq\omega_z\leq$0.5 in all plots and the timing of the plot acquisition is indicated by a small circle on the sinusoidal cylinder motion in a zoom box.

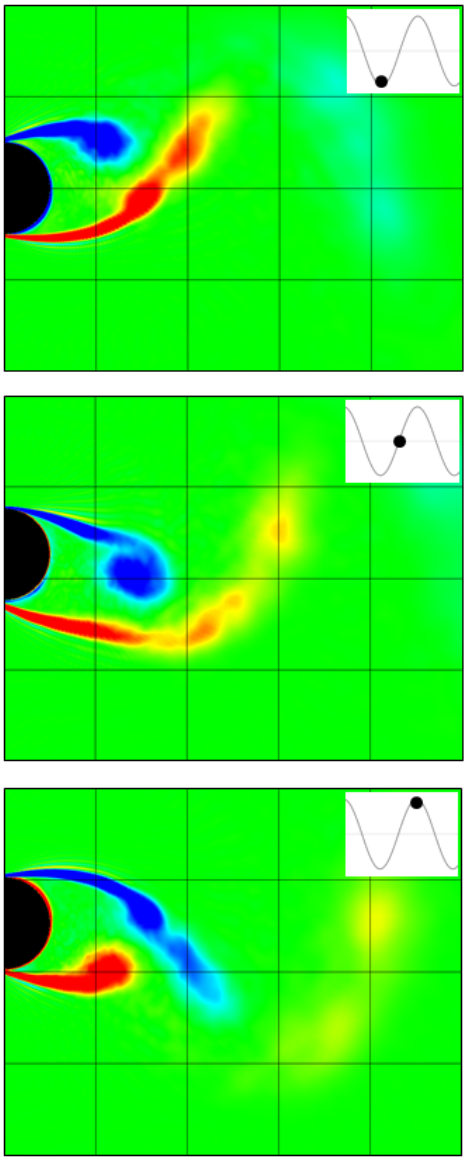

(a) Evolution of phase-averaged vortex structure at f_e/f_K=0.865.

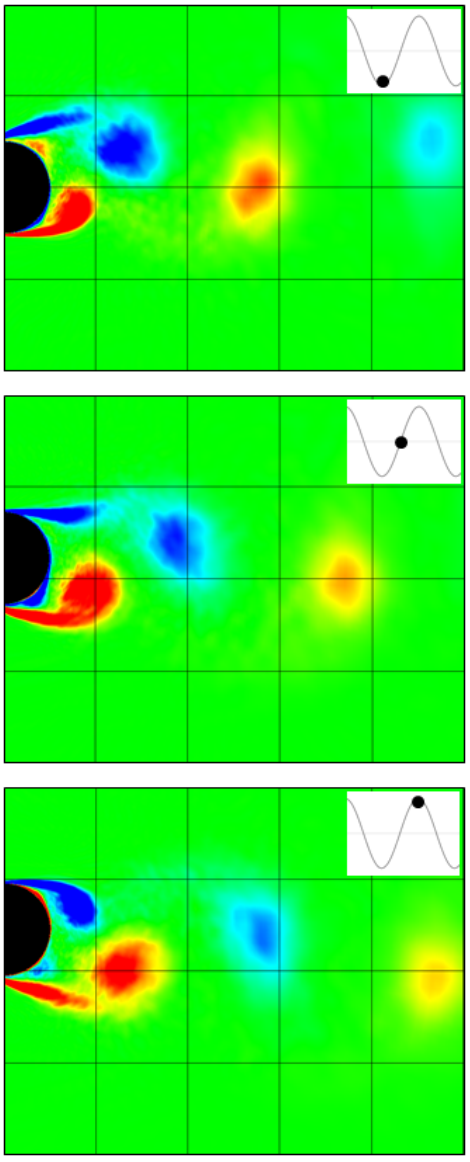

(b) Evolution of phase-averaged vortex structure at f_e/f_K=1.009.

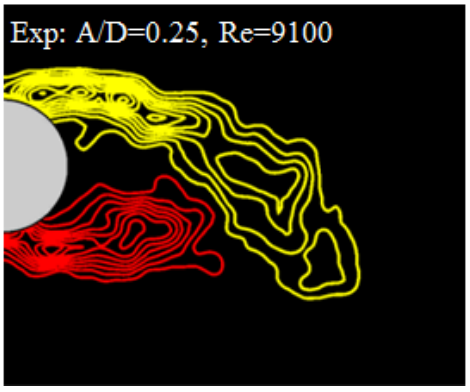

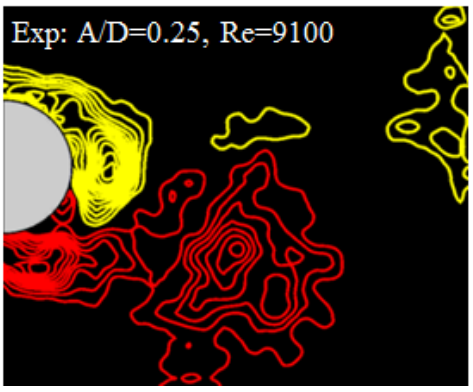

(c) Forced vibration experiments of phase-averaged low- and high-frequency states (left and right respectively) at the top of the cylinder oscillations, produced by Carberry [1].

FIGURE 5.14: Phase- and spanwise-averaged vorticity fields at A/D=0.3 and Re=10000 (a,b): the images are obtained at evenly spaced intervals of the cylinder displacement, and the contour level is -0.5$\leq\omega_z\leq$0.5 and phase-averaged over 10 cycles in simulation cases.

For comparison purposes, the experimental observations from Carberry [1] in similar parameter conditions, a low amplitude ratio of A/D=0.25 and Re=9100, are shown in Figure 5.14(c) and the plots were measured at the top of the oscillation cycles. The elongated upper shear layer across the cylinder base in the low-frequency state and the the upper vortex structure tightly formed behind the cylinder in the high-frequency state are noted and comparable with Figure 5.14(a,b-bottom). The difference between experiments and LES results in the high-frequency wake state might be due to the phase of the cylinder. It seems that the experimental measurement was captured when the

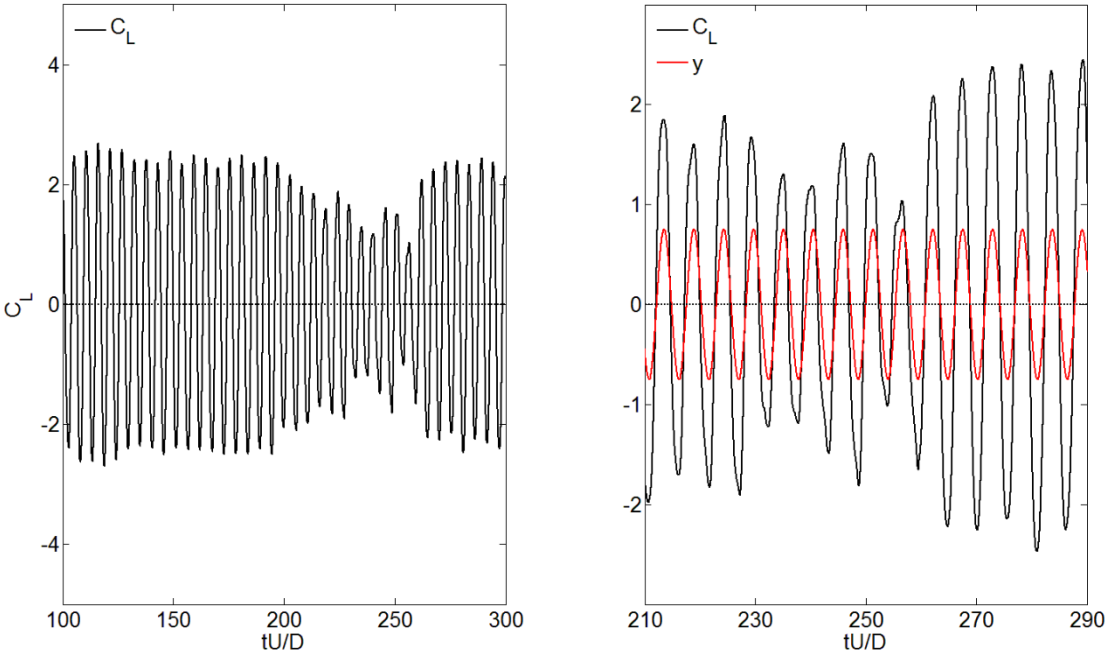

(a) Time trace of lift at f_e/f_K=0.889 close to f_K, showing that lift still has high amplitude and is in-phase with the cylinder motion like in the high-frequency wake state.

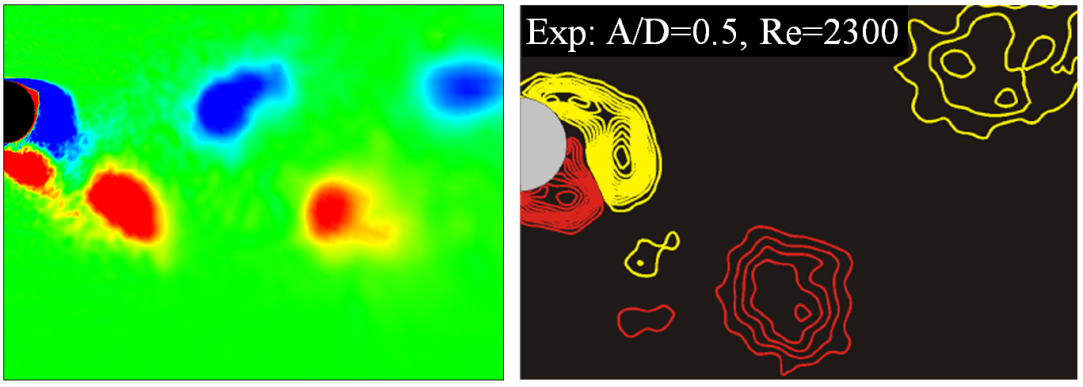

(b) Phase- and spanwise-averaged intermediate wake mode over 10 cycles between 110< tU/D <295 with a contour level of -0.15≤ ω_z ≤0.15, showing the overlap mode of the 2P and 2S patterns (left) and experiment (right) produced by Carberry [1].

FIGURE 5.15: Time trace of lift at A/D=0.75 and Re=10000 (a) and corresponding vorticity field (b): the images are obtained at the top point of the cylinder displacement.

cylinder is approaching the top of the cylinder oscillation.

Based on previous experimental observations as shown in Figure 1.8, a new wake state, which was firstly identified from recent controlled oscillation experiments by Carberry et al. [4] and Morse and Williamson [5], is numerically investigated. A new wake state has been revealed in which the two vortex formations of 2P and 2S overlap at a certain range of amplitude ratios within a very narrow frequency ratio close to f_e/f_K=1.0.

Figure 5.15(a) shows the time history of lift coefficients at f_e/f_K=0.889 in the case of higher A/D=0.75 and Re=10000. The lift trace exhibits large amplitude fluctuations generally, but beating behaviour exists in the range of $230<tU/D<270$, indicating that this state is less steady compared to both low- and high-frequency states. However, overall behaviour of lift properties, with high amplitude and in-phase with the cylinder motion, are quite similar to those in the high-frequency wake state. In the experiment at A/D=0.5-0.6 and Re=2300 performed by Carberry et al. [4], it was observed that the characteristic of the intermediate wake state is a high vortex lift phase angle $\phi_{L\text{vortex}}\approx180^\circ$ compared with those in the high-frequency wake state $\phi_{L\text{vortex}}\approx0^\circ$ to -90° with increasing f_e/f_K, as shown in Figure 5.4(left). In this study, however, the vortex lift phase is indicated as just around 45°.

In Figure 5.15(b), nevertheless, the corresponding vorticity field shows a distinctly different pattern with a 2S wake mode in the high-frequency wake state. Two single vortices formed per oscillation cycle in the wake, but the phase points, where large-scale vortices are generated, are very similar to those of the 2P wake mode. Therefore, the wake pattern in the intermediate wake state between low- and high-frequency states partially shares some features in both the 2S and 2P wake modes. In a set of the present numerical simulations, the intermediate wake state is captured only at f_e/f_K=0.889, A/D=0.75 and Re=10000.

The difference of vortex phase with those in the experiment is that either a more stable intermediate wake state could exist in a very narrow band of f_e/f_K between low- and high-frequency states or the intermediate state could be depend on the Reynolds number. It is noted that the intermediate state in the experiment was only observed at Re=2300 among a set of Reynolds numbers Re=2300,4410 and 9100.

5.4 Transition Between Stable Wake States

In the previous section 5.3, it was seen that the 3-D LES numerical study has clearly reproduced the flow characteristics of an oscillating cylinder throughout a range of frequency ratios f_e/f_K around f_e=f_K at (A/D,Re)=(0.5,5500), (0.75,5500), (0.3,10000), (0.5,10000) and (0.75,10000), whilst previously the features were calculated individually in separate forced vibration simulations at lower Reynolds numbers in a laminar flow regime or by using a 2-D solution in a subcritical regime. All LES solutions have been spanwise- or phase-averaged in order to obtain qualitative predicted results and systemically examined. The present study clearly showed the three distinct wake modes on either side of the well-known jump of lift properties, C'_L and ϕ_L. Within the stable low- and high-frequency wake states as well as the intermediate wake state, the time trace of lift properties at a constant frequency and amplitude ratio do not change as expected, indicating that the resulting wake patterns persist over the whole simulation time. Although there are slight differences of each wake mode in low- and high-frequency wake states as A/D and Re vary, the basic formation of the pattern is not changed.

In order to understand the nature of the transition or change process between two distinct different wake patterns, in this section, the transition area in which the sharp jump occurs is numerically investigated in detail. As shown in Figure 5.2 for the low-frequency state and in Figure 5.16 for the high-frequency state at A/D=0.3 and Re=5500, the 3-D LES indicates that the time trace of lift for both wake states is fully established in tU/D=70 at least after tU/D=0 and then the lift fluctuation is not changed significantly for the whole simulation time.

5.4.1 Self-excited transition

For a narrow band of frequency ratios around transitional frequency, self-excited transition is numerically observed in the lift force coefficient after the time trace is fully established, while frequency ratio is held as a constant. Two different wake patterns, 2P and 2S, therefore, have been captured at separated frequency ratios on either side of the abrupt jump in the previous section.

At a constant frequency ratio of 0.961 for A/D=0.3 and Re=10000, self-excited change in the lift from the low-frequency to high-frequency wake state is numerically captured

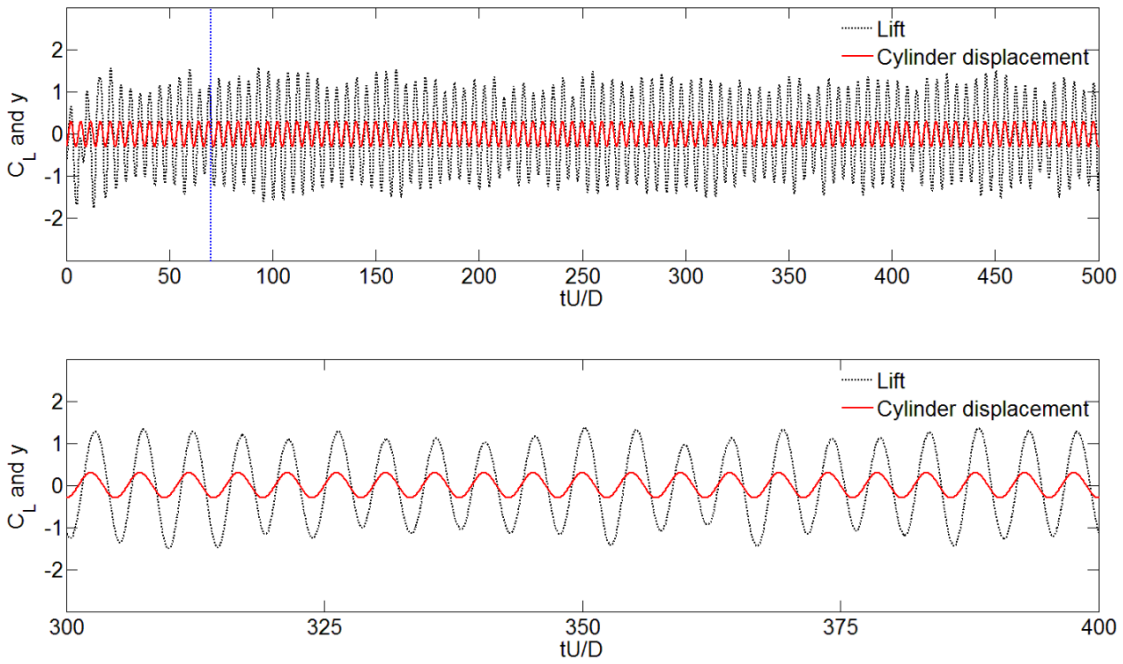

FIGURE 5.16: Time history of the lift coefficient and the cylinder displacement at f_e/f_K=1.009, A/D=0.3 and Re=10000, showing a stable high-frequency wake state after a period of staring time.

for a narrow band of frequency ratios near F_{tr}, first in a set of simulations, as shown in Figure 5.17(a). For times less than a non-dimensional time $tU/D \approx$300, the behaviour of lift conforms to the low-frequency state as discussed in the previous section. After about 4 cycles of oscillation, for times after tU/D=320, the lift is consistent with the high-frequency state. The expanded time history shows the behaviours of the lift and cylinder displacement in the transition during $240 < tU/D < 360$. It is indicated that the instantaneous lift coefficient and its phase with respect to the cylinder displacement change smoothly from the low- to high-frequency wake state at a single excitation frequency.

It is expected that the self-excited transition at f_e/f_K=0.961 corresponds to a change in near-wake structure. As is known for the controlled vibration of a cylinder with a moderate amplitude ratio of 0.3 at high Reynolds numbers, two characteristic wake modes, namely 2P and 2S, are identified at different frequency ratios in the map of vortex-shedding regimes recently measured by Morse and Williamson [5], describing the sudden transition between two wake patterns. Figure 5.17(b,c) shows two different wake modes at the constant frequency ratio. The vorticity field is spanwise- and phase-averaged over 8 cycles of oscillation in order to make close approximation with the experiment. The locations of the cylinders are mid-position in the upward direction.

Despite the fact that the excitation frequency is held as a constant, two wake modes are significantly different as a non-dimensional time tU/D increases. It is indicated that the self-excited and smooth change in the lift properties are intrinsically related to the variation in the wake modes from 2P to 2S.

The present study, therefore, provides numerical evidence that the distinct different wake modes can switch intermittently between low- and high-frequency wake modes,

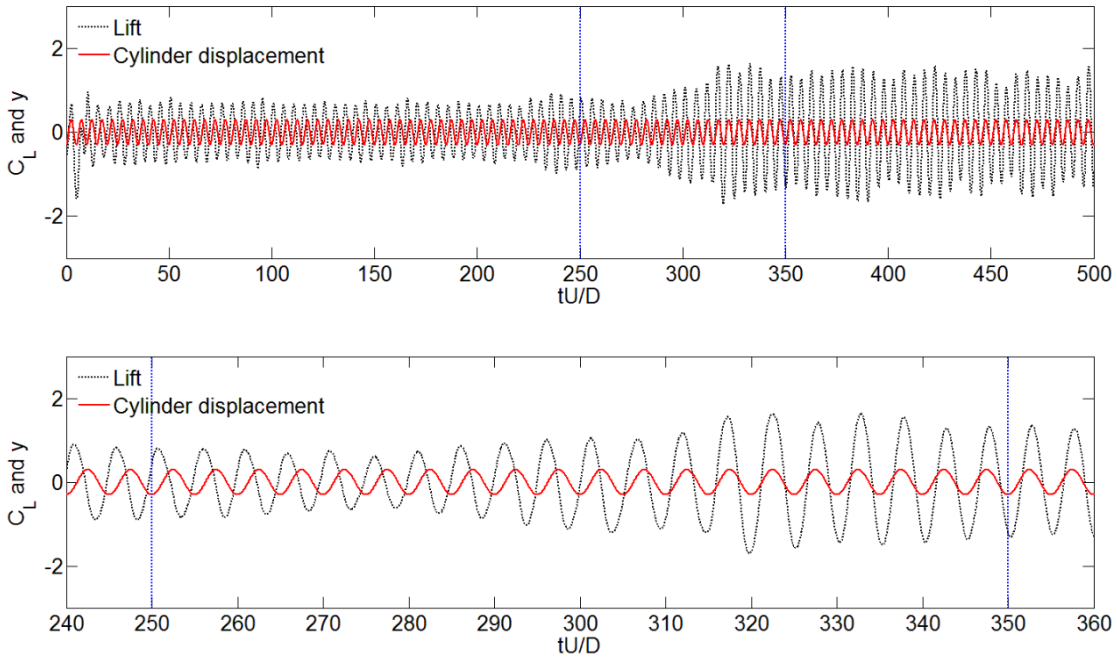

(a) The time trace of the lift coefficient at f_e/f_K=0.961.

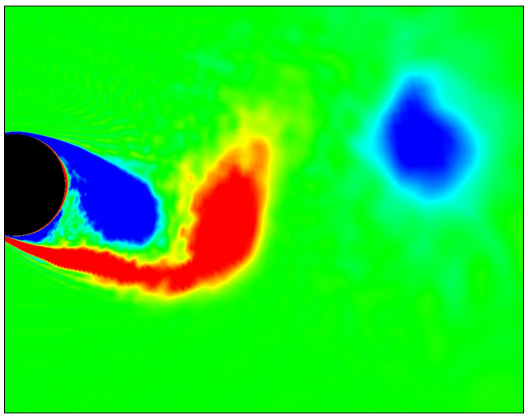

(b) Low-frequency wake modes at f_e/f_K=0.961: averaging 241.25≤tU/D≤291.25.

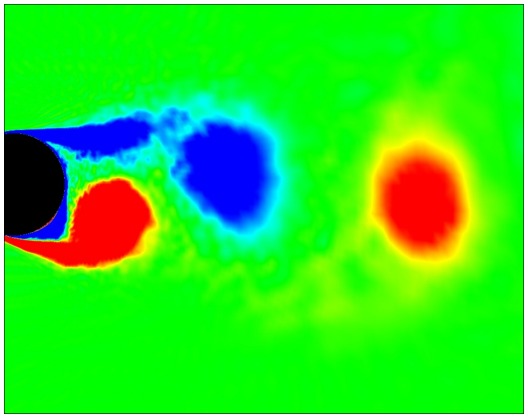

(c) High-frequency wake modes at f_e/f_K=0.961: averaging 376.25≤tU/D≤486.25

FIGURE 5.17: Time trace of lift and the cylinder displacement at A/D=0.3 and Re=10000 (a) and the corresponding variation in the phase- and spanwise-averaged wake modes (b,c): the vorticity fields are spanwise- and phase-averaged over 8 cycles of oscillation and the contour level is -0.4≤ω_z≤0.4. The locations of the cylinders are mid-position in the upward direction from the cylinder oscillation.

and the patterns are intrinsically linked with each other, even as the cylinder is oscillating with constant amplitude and frequency. At other values of A/D and Re, a self-excited transition was not always captured, indicating that the transition might be very narrow. Carberry et al. [4, 7, 31] observed the self-excited transition between low-frequency and intermediate wake states, only measured at Re=2300 with higher amplitude ratios of 0.5 and 0.6, among their extensive experimental measurements: $(A/D, \mathrm{Re})$=$(0.25-0.6, 2300-9100)$.

5.4.2 Reverse self-excited transition

As discussed in the previous section, three different wake patterns have been numerically captured with increasing f_e/f_K throughout transitional frequency F_{tr} in the case of the higher amplitude ratio A/D=0.75 and Re=10000. More detail study of the transitional process near the transitional frequency, therefore, is needed.

A change in the nature of the self-excited transition is numerically observed in Figure 5.18. In contrast to the self-excited transition at A/D=0.3, the wake moves first to the high-frequency state and after a period of time there is a reverse self-excited transition to the low-frequency wake state. The corresponding wake modes change from the intermediate to low-frequency wake state as shown in Figure 5.18(b,c).

This reverse self-excitation more often occurred in whole simulation cases at Re=5500-10000, compared to the self-excited transition, indicating the wake of an oscillating cylinder prefers to move to the high-frequency wake state. It is noted that the terminology of the reverse self-excitation was firstly used in the experiment at Re=9100 and A/D=0.5 by Carberry [1]. At Re=5500, the reverse self-excited transition exists at only two separated frequency ratios of 0.806 and 0.809 in the present study.

Figure 5.19 shows time history of the force coefficients and the cylinder displacements at f_e/f_K=0.806. After the oscillating wake is fully established at the initial part of the lift trace, the lift force firstly exhibits the characteristics of the high-frequency state, high lift amplitude and low ϕ_L value of about 54.9°. However, the lift shows somewhat irregular and beating amplitude behaviour. It seems that this unstable area within the reverse self-excited transition is not fully established to either the low- or high-frequency state.

After many oscillations, this state returns to the low-frequency state, characterised by low lift amplitude and high ϕ_L of about 136.9°.

In the reverse self-excited transition, the different behaviours of the lift indicate a change of the wake mode at a single frequency ratio. Figure 5.20 shows two different wake modes as non-dimensional time tU/D increases. The spanwise-averaged vorticity field at tU/D=262.6 in Figure 5.20(left) shows the intermediate wake state.

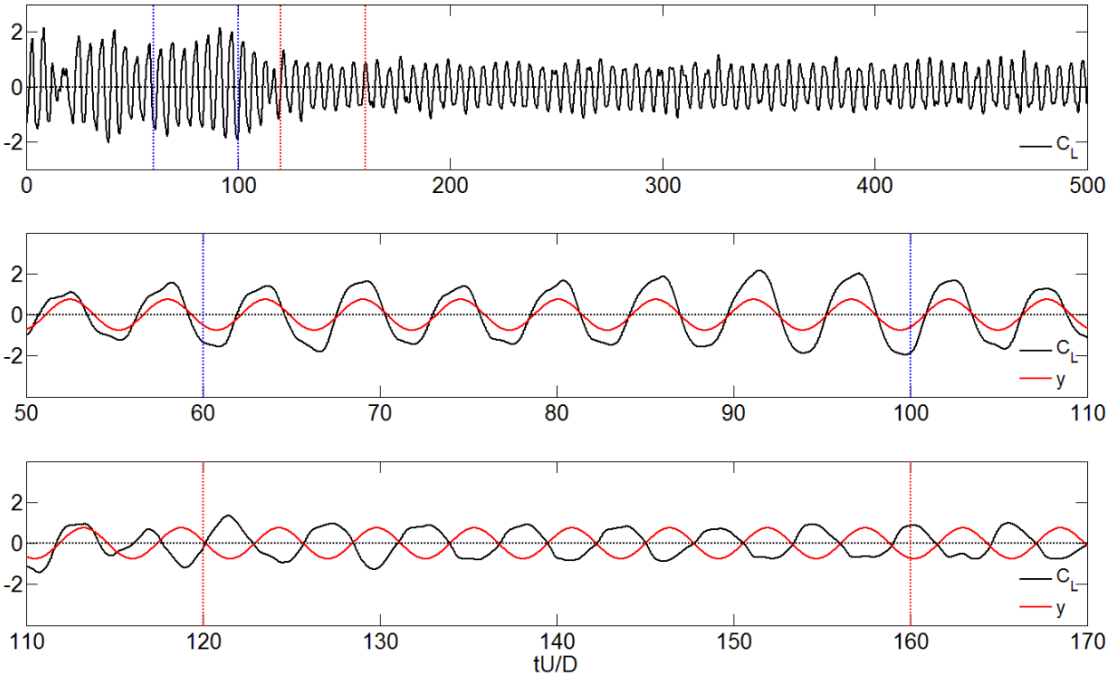

(a) The time trace of lift coefficient at f_e/f_K=0.865.

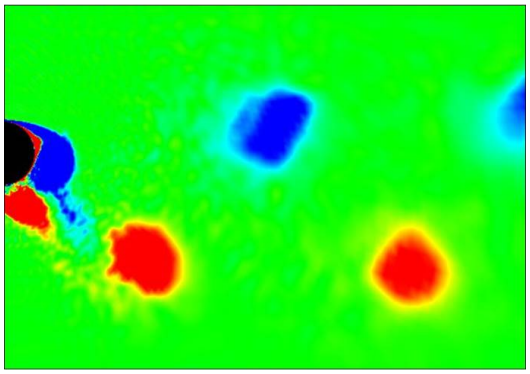

(b) Intermediate wake mode at f_e/f_K=0.865: averaging 63.54≤tU/D≤96.69.

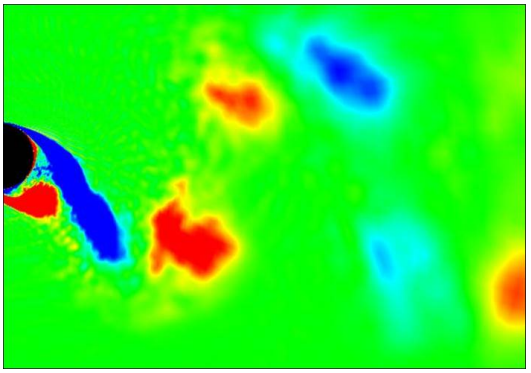

(c) Low-frequency wake mode at f_e/f_K=0.865: averaging 229.28≤tU/D≤488.95.

FIGURE 5.18: Time trace of lift and the cylinder displacement at A/D=0.75 and Re=10000 (a) and the corresponding variation in the averaged wake modes (b,c): the vorticity fields are spanwise- and phase-averaged over 7 cycles of oscillation and the contour level is -0.15≤ω_z≤0.15. The cylinders are located in the extreme upper position.

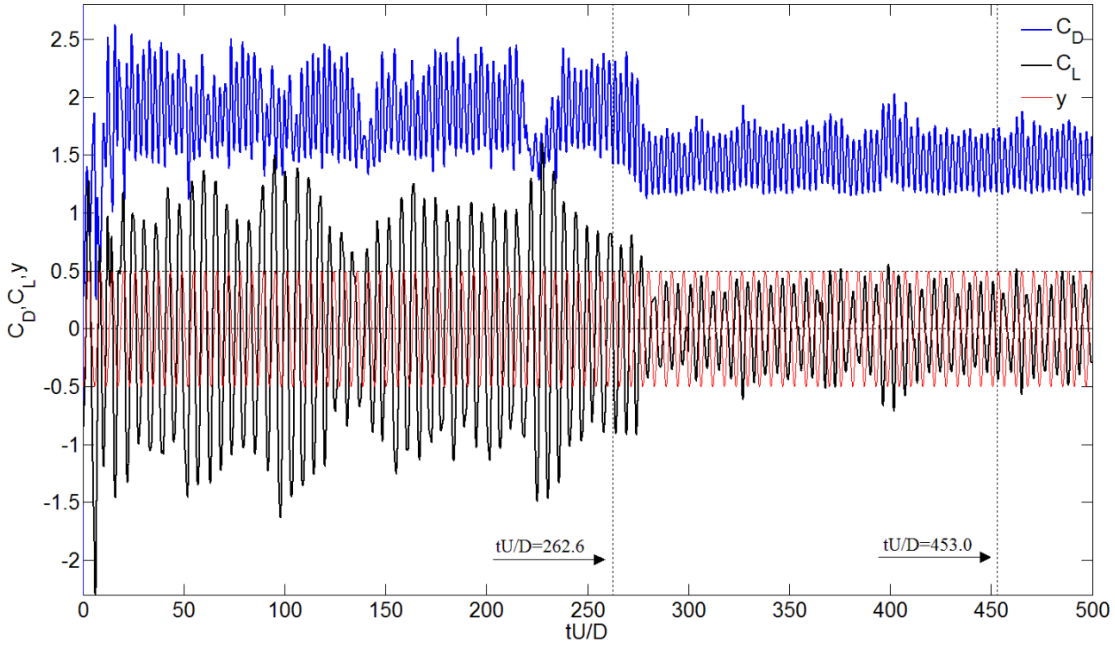

FIGURE 5.19: Time history of the force coefficients and the cylinder displacement at f_e/f_K=0.806 in the case of A/D=0.5 and Re=5500, showing that the time trace of the lift shows beating behaviour up to about tU/D=275, whilst the time history of the lift in the high-frequency state shows nearly constant amplitude in general.

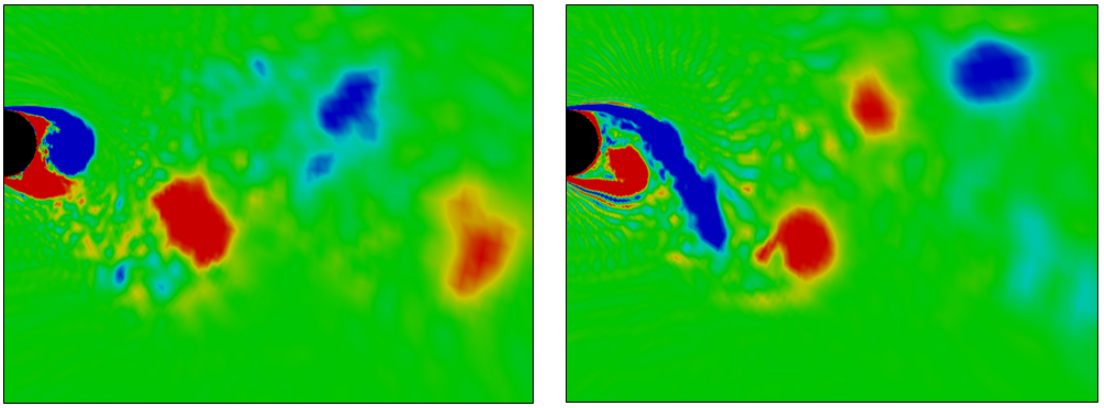

FIGURE 5.20: Spanwise-averaged vorticity fields at f_e/f_K=0.806 in the case of A/D=0.5 and Re=5500, showing the intermediate wake mode at tU/D=262.6 (left) and the low-frequency wake mode at tU/D=453.0 (right): The cylinders are located in the extreme upper position.

5.5 Closure

3-D LES calculations have been performed for the turbulent flow past a controlled vibrating cylinder with a series of constant amplitude ratios and frequency ratios at subcritical Reynolds numbers of 5500-10000. For a complete validation of the near-wall grid resolution and moving grid on an oscillating cylinder, the main wake parameters have been estimated and compared with the experiment measurements and DNS data at A/D=0.3

and Re=10000, indicating that the flow characteristics including the sharp jump of the lift properties as well as the magnitude of force coefficients are reasonably predicted by the 3-D LES technique.

The present study clearly reproduced some important and classical flow features over an oscillating cylinder throughout a range of frequency ratios f_e/f_K around f_e=f_K at (A/D,Re)=(0.5,5500),(0.75,5500),(0.3,10000),(0.5,10000) and (0.75,10000). At low values of f_e/f_K defined as the low-frequency wake state, the lift force had small amplitudes and was approximately out-of-phase with the cylinder oscillation. After passing a certain transitional frequency ratio F_{tr}, the lift properties were experienced with the well-known sharp changes, and the lift force had large lift amplitude approximately in-phase with the cylinder motion in the high-frequency wake state. The instantaneous vorticity structures at Re=5500 showed the vortex switching process on either side of the transition as observed in the experiment by Gu et al. [6]. Simultaneously, the change of the wake modes from 2P to 2S was successfully captured before and after the transition by using the phase- and spanwise-averaged contours of the vorticity fields at Re=5500-10000. Based on the recent experimental observations by Morse and Williamson [5], Carberry et al. [7], the present study showed the existence of the intermediate wake state between the low- and high-frequency wake state within a narrow band of frequency ratios at A/D=0.75 and Re=10000. The resulting overlap wake mode between 2P and 2S patterns was phase- and spanwise-averaged and compared with the experiment.

In this study, the self-excited and reverse transition from one stable state of vortex formation to another stable wake state at a constant frequency of oscillation is numerically captured first in a set of simulations. In the transition process, the instantaneous lift properties change smoothly from the one to the other wake states at a single excitation frequency. The corresponding wake modes in each wake state at a single frequency indicate that the self-excited change in the lift properties is intrinsically linked to the change in the wake modes.

Chapter 6

CONCLUSIONS

This thesis is related to investigating the force and wake state of a cylinder forced to oscillate transversely to a free-stream. This investigation seeks to numerically determine the nature of the transition between two different near-wake structures because the transition process is a fundamental issue in VIV phenomenon. This study clearly showed the numerical evidence that two distinct wake patterns are intrinsically linked with each other. Previously these wake patterns were observed separately in free vibration or VIV study. The forced purely harmonic oscillations appear to reproduce the wake structures and forces observed for a freely oscillating cylinder and to simulate many of important features of VIV. It is hoped that these results together with the other important ideas in this thesis summarised in the next section will help researchers and engineers to estimate and control of vorticity in full-scale situation.

6.1 Stationary Cylinder

In Chapter 3 of this thesis, the wake parameters and mean flow statistics around a stationary circular cylinder at a range of Reynolds numbers, Re=5500-41300, have been examined. The original motivation in conducting these calculations was to lay the basis for the next two Chapters. Therefore, the objective in Chapter 3 was not to study the physics of the cylinder flow in detail but to conduct an extensive investigation into numerical and modelling aspects influencing the quality of LES solutions.

6.1.1 Influence of spanwise grid resolution

The important role of the spanwise resolution, which has often been underestimated for LES, must be emphasised. The main wake parameters are fairly sensitive to the grid resolution, especially for the fluctuating lift coefficients. Based on the comparative results of the parameter for high Reynolds flows, the spanwise spacing $\Delta z/D \leq 0.05$ or $N_z \geq 64$ is necessary as minimum in order to predict the lift force reasonably.

6.1.2 Influence of subgrid scale model

The importance of the SGS modeling for high Reynolds flows was clearly demonstrated in Chapter 3. To capture all the flow details at the subcritical Reynolds numbers considered in this thesis, very fine grids needed to be utilized. The resolution cannot be enlarged according to the length scale, $N_{total} \approx \mathrm{Re}^{1.8}$ from Choi and Moin [68], and this leads to the prime importance of SGS modeling for high Reynolds flows being insignificant for low Reynolds.

Because there is no global SGS model which is applicable to all flow regimes, this study suggested that a suitable SGS model with a wall modelling approach should be adopted in a high Reynolds number flows in order to obtain close approximations with experimental data and the key role of SGS model on the turbulent flow at each Reynolds number is emphasised:

- The eddy-viscosity type Smagorinsky model with C_s=0.1 at Re=5500.
- The eddy-viscosity type k-equation model with C_ϵ=1.0 and C_k=0.05 at Re=10000.
- The dynamic k-equation model with C_ϵ=1.0 at Re=41300, see Kim et al. [69].

6.1.3 Shear-layer instability

In Chapter 4 of this thesis, special focus is made on the shear-layer or Kelvin-Helmholtz instability characterized by small-scale structures and high frequencies. With the large-scale von Kármán vortex street the shear-layer instability involves a complex multi-scale problem.

The outcome of this study comes from the analysis of the shear-layer instability in this range of subcritical Reynolds number, see Kim et al. [70]. The broadband nature of the shear-layer instability as well as the frequency behaviour with Re=5000-41300 were numerically captured. The predictions of the shear-layer frequency tended to follow the experimental power-law scaling of $\mathrm{Re}^{0.67}$ with increasing Reynolds number.

These multi-scale vortex interactions in the cylinder near wake are still not totally understood. Some opening questions remain as for example the role played by these interactions on the instability mechanisms leading to fluid structure interactions.

6.2 Forced Oscillating Cylinder

In Chapter 5, based on careful validations of the moving grid approach, this study clearly reproduced some important and classical flow features over an oscillating cylinder throughout a range of frequency ratios f_e/f_K around $f_e{=}f_K$. The well-known sharp and abrupt jump in the lift force was numerically reproduced at the various amplitude ratios and Reynolds numbers. As A/D and Reynolds number increased, the transition frequency was increased toward $f_e/f_K{=}1.0$ and the jump also shifted upwind.

According to recent experimental observations, three different wake states, namely low-, intermediate and high-frequency wake, were investigated in terms of the lift properties, lift fluctuation and lift phase angle. The resulting instantaneous wake modes were phase- and spanwise-averaged, and clearly captured three different wake patterns in 3-D LES calculations. Furthermore, the self-excited and reverse transition from one to other wake state at a constant frequency of oscillation is numerically captured first in a set of simulations, see Kim et al. [71, 72]. The following findings are observed:

- The numerical evidence of the wake mode $2\mathrm{P}_o$ in the intermediate wake state, which exists within a very narrow band of frequency ratios near the transitional frequency at a high amplitude ratio of $A/D{=}0.75$ and Re=10000.
- The numerical evidence of the self-excited transition even at a lower amplitude ratio $A/D{=}0.3$ and Re=10000, indicating that the wake modes of 2P and 2S could switch in a one-time transition.

- The numerical evidence of the reverse self-excited transition at higher amplitude ratios A/D=0.5 and 0.75, indicating that the wake modes of $2P_o$ and 2P could switch in a one-time transition. In the present study, the reverse self-excited transition more often occurred between two separated wake states at the considered amplitude ratios and Reynolds numbers of 5500 and 10000. It seems that the nature prefers to be in the high-frequency wake state as the excitation increases to the transitional frequency.

In the transition process, the instantaneous lift properties change smoothly from one to another of the wake states at a single excitation frequency. The corresponding wake modes in each wake state at a single frequency indicate that the self-excited change in the lift properties is intrinsically linked to the change in the wake modes. This numerical evidence supports the contentions of Carberry et al. [4, 7, 31] and Morse and Williamson [5] regardin the mechanism of the one-time transition of the wake modes.

6.3 Recommendations for Future Work

The research into the turbulent flow past a circular cylinder has been at the centre of numerous investigations. In terms of the aspect of numerical simulation, the cylinder flow involves remarkably complex flow features such as thin separating shear layers, transition and large-scale vortex motion in the wake. In LES, only the fine-scale turbulence has to be modelled by a subgrid scale model. However, the present study showed the Reynolds number dependence of the SGS models and thus the influence of the SGS model is not negligible in terms of hydrodynamic coefficients. One of the remedies to this problem is to increase grid resolution in order to predict the fine or subgrid scale turbulence on the grid scale as much as possible, but this results in huge computation time. In comparison with the dynamic and one-equation type SGS model, the algebraic Smagorinsky-type model is quite cheap in terms of computational cost. Therefore, the development or re-scaling of the model coefficients with particular focus on the high Re flow regime over a cylinder is necessary to obtain the ticket to real subsea engineering applications.

Owing to relatively long computation times and heavy hardware resource for 3-D LES calculation, detailed numerical studies on the important topics of an oscillating cylinder flow are very rare even at low Reynolds numbers. One of these interesting topics is the

spanwise wake structure along the cylinder axis direction. When a cylinder oscillates, there is an increase in the spanwise coherence of vortex shedding in three-dimensionality. As the spanwise-averaged wake states have been characterised in terms of the 2-D wake structure in the present study, the spanwise wake structures are not examined in detail even in the experiment.

Finally, an aspect that was not examined in the present study concerns the flow-induced motion or VIV. Even though the present controlled vibration study showed many of the same features as a freely-oscillating cylinder, especially on the resulting wake modes, there are some differences between forced and free vibration studies such as energy transfer between fluid and structure. Therefore, more detailed numerical study of freely-oscillating cylinder flow together with controlled oscillation study is required in order to gain a better understanding of vortex dynamics in the VIV phenomenon.

Appendix A

Academic publishing

The academic papers from the present thesis, which have been published and submitted, are listed as below order:

- **Large eddy simulation of flow past a stationary and controlled oscillating circular cylinder**, Sunghan Kim, Philip A. Wilson, Zhi-Min Chen, 32nd Conference on Ocean, Offshore and Arctic Engineering, *OMAE 2013*, Nantes, France.
- **Numerical simulation of force and wake mode of an oscillating cylinder**, Sunghan Kim, Philip A. Wilson, Zhi-Min Chen, *Journal of Fluids and Structures* 44 (2014), 216-225.
- **Controlled vibrations of a submerged cylinder**, Sunghan Kim, Philip A. Wilson, Zhi-Min Chen, *Journal of Fluids and Structures* (Submitted).
- **Large-eddy simulation of the turbulent near-wake behind a circular cylinder: Reynolds number effects**, Sunghan Kim, Philip A. Wilson, Zhi-Min Chen, *Applied Ocean Research* (Submitted).
- **Effect of turbulence modelling on 3-D LES of transitional flow behind a circular cylinder**, Sunghan Kim, Philip A. Wilson, Zhi-Min Chen, *Ocean Engineering* (Submitted).

Bibliography

[1] J. Carberry. *Wake states of a submerged oscillating cylinder and of a cylinder beneath a free-surface*. PhD thesis, Monash University, 2002.

[2] C. Norberg. Fluctuating lift on a circular cylinder: Review and new measurement. *Journal of Fluids and Structures*, 17:57–96, 2003.

[3] S. Dong, G.E. Karniadakis, A. Ekmekci, and D. Rockwell. A combined direct numerical simulation-particle image velocimetry study of the turbulent near wake. *Journal of Fluid Mechanics*, 569:185–207, 2006.

[4] J. Carberry, J. Sheridan, and D. Rockwell. Controlled oscillations of a cylinder: Forces and wake modes. *Journal of Fluid Mechanics*, 538:31–69, 2005.

[5] T.L. Morse and C.H.K. Williamson. Prediction of vortex-induced vibration response by employing controlled motion. *Journal of Fluid Mechanics*, 634:5–39, 2009.

[6] W. Gu, C. Chyu, and D. Rockwell. Timing of vortex formation from an oscillating cylinder. *Physics of Fluids*, 6:3677–3682, 1994.

[7] J. Carberry, J. Sheridan, and D. Rockwell. Controlled oscillations of a cylinder: A new wake state. *Journal of Fluids and Structures*, 17:337–343, 2003.

[8] P. Catalano, M. Wang, G. Iaccarino, and P. Moin. Numerical simulation of the flow around a circular cylinder at high Reynolds numbers. *International Journal of Heat and Fluid Flow*, 24:463–469, 2003.

[9] H.M. Blackburn, R.N. Govardhan, and C.H.K. Williamson. A complementary numerical and physical investigation of vortex-induced vibration. *Journal of Fluids and Structures*, 15:481–488, 2000.

[10] X.Y. Lu and C. Dalton. Calculation of the timing of vortex formation from an oscillating cylinder. *Journal of Fluids and Structures*, 10:527–541, 1996.

[11] M.M. Zdravkovich. *Flow around circular cylinders Vol 1: Fundamentals.* Oxford University Press, 1997.

[12] A. Roshko. On the wake and drag of bluff bodies. *Journal of Aeronautical Sciences*, 22:124–132, 1955.

[13] C.H.K. Williamson. Vortex dynamics in the cylinder wake. *Annu. Rev. Fluid. Mech.*, 328:345–407, 1996.

[14] C.H.K. Williamson. Three-dimensional wake transition. *Journal of Fluid Mechanics*, 190:513–529, 1996.

[15] D.F.L. Labbé and P.A. Wilson. A numerical investigation of the effects of the spanwise length on the 3-D wake of a circular cylinder. *Journal of Fluids and Structures*, 23:1168–1188, 2007.

[16] M.S. Bloor. The transition to turbulence in the wake of a circular cylinder. *Journal of Fluid Mechanics*, 19:290–304, 1964.

[17] M.F. Unal and D. Rockwell. On vortex formation from a cylinder: Part 1. The initial instability. *Journal of Fluid Mechanics*, 190:491–512, 1988.

[18] J. Wu, J. Sheridan, K. Hourigan, and J. Soria. Shear layer vortices and longitudinal vortices in the near wake of a circular cylinder. *Experimental Thermal and Fluid Science*, 12:169–174, 1996.

[19] Mark C. Thompson and Kerry Hourigan. The shear-layer instability of a circular cylinder wake. *Physics of Fluids*, 17:021702–1–021702–4, 2005.

[20] C. Norberg. LDV-measurements in the near wake of a circular cylinder. ASME Fluids Engineering Division, Washington D.C., Bluff Body Wakes and Vortex-Induced Vibration, P.42, 1998.

[21] T. Wei and C. R. Smith. Secondary vortices in the wake of circular cylinders. *Journal of Fluid Mechanics*, 169:513–533, 1986.

[22] C. Norberg. Effect of Reynolds number and a low-intensity freestream turbulence on the flow around a circular cylinder. Publ. 87/2, Department of Applied Thermodynamics and Fluid Mechanics, Chalmers Universityof Technology, 1987.

[23] C. Chyu, J.-C. Lin, J. Sheridan, and D Rockwell. Kármán vortex formation from a cylinder: Role of phase-locked kelvin-helmholtz vortices. Brief communications, Phys.Fluids 7(9), 1995.

[24] A. Prasad and C.H.K. Williamson. The instability of the separated shear layer from a bluff body. *Physics of Fluids*, 8:1347–1349, 1996.

[25] S. Rajagopalan and R.A. Antonia. Flow around a circular cylinder-structure of the near wake shear layer. *Experiments in Fluids*, 38:393–402, 2005.

[26] R.E.D. Bishop and A.Y. Hassan. The lift and drag forces in a circular cylinder in a flowing fluid. *Proceedings of the Royal Society of London*, 277:32–48, 1964.

[27] T. Sarpkaya. Fluid forces on oscillating cylinders. *ASCE Journal of Waterway, Port, Coastal, and Ocean Division*, 104:275–290, 1978.

[28] C.H.K. Williamson and A. Roshko. Vortex formation in the wake of an oscillating cylinder. *Journal of Fluids and Structures*, 2:355–381, 1988.

[29] A. Ongoren and D. Rockwell. Flow structure from an oscillating cylinder: Part 1. Mechanisms of phase shift and recovery in the near wake. *Journal of Fluid Mechanics*, 191:197–223, 1988.

[30] R. Gopalkrishnan. *Vortex-induced forces on oscillating bluff cylinders*. PhD thesis, Department of Ocean Engineering, MIT, Cambridge, MA, USA., 1993.

[31] J. Carberry, J. Sheridan, and D. Rockwell. Forces and wake modes of an oscillating cylinder. *Journal of Fluids and Structures*, 15:523–532, 2001.

[32] M. Breuer. Numerical and modeling influences on large eddy simulations for the flow past a circular cylinder. *International Journal of Heat and Fluid Flow*, 19: 512–521, 1998.

[33] P. Beaudan and P. Moin. Numerical experiments on the flow past a circular cylinder at sub-critical reynolds number. Report TF-62, Stanford University, USA, 1994.

[34] S. Mittal and P. Moin. Suitability of upwind-biased finite-difference schemes for large-eddy simulation of turbulent flows. *AIAA Journal*, 35:1415–1417, 1997.

[35] A.G. Kravchenko and P. Moin. Numerical studies of flow over a circular cylinder at Re=3900. *Physics of Fluids*, 12:403–417, 2000.

[36] S.A. Jordan. Investigation of the cylinder separated shear-layer physics by large-eddy simulaion. *International Journal of Heat and Fluid Flow*, 23:1–12, 2002.

[37] M. Breuer. A challenging test case for large eddy simulation: high Reynolds number circular cylinder flow. *International Journal of Heat and Fluid Flow*, 21:648–654, 2000.

[38] S. Wornom, H. Ouvrard, M.V. Salvetti, B. Koobus, and A. Dervieux. Variational multiscale large-eddy simulations of the flow past a circular cylinder: Reynolds number effects. *Computers & Fluids*, 47:44–50, 2011.

[39] E. Guilmineau and P. Queutey. A numerical simulation of vortex shedding from an oscillating circular cylinder. *Journal of Fluids and Structures*, 16:773–794, 2002.

[40] H.M. Blackburn and R.D. Henderson. A study of two-dimensional flow past an oscillating cylinder. *Journal of Fluid Mechanics*, 385:255–286, 1999.

[41] M. Tutar and A.E. Holdo. Large eddy simulation of a smooth circular cylinder oscillating normal to a uniform flow. *Jounrnal of Fluids Engineering*, 122:694–702, 2000.

[42] S. Dong and G.E. Karniadakis. DNS of flow past a stationary and oscillating cylinder at Re=10000. *Journal of Fluids and Structures*, 20:519–531, 2005.

[43] S. Atluri, V.K. Rao, and C. Dalton. A numerical investigation of the near-wake structure in the variable frequency forced oscillation of a circular cylinder. *Journal of Fluids and Structures*, 25:229–244, 2009.

[44] J.W. Deardorff. Stratocumulus-capped mixed layers derived from a three-dimensional model. *Boundary-Layer Meteorol*, 18:495–527, 1980.

[45] J.S. Smagorinsky. General circulation experiments with the primitive equations. *Monthly Weather Review*, 91:99–152, 1963.

[46] S. Menon and W.W. Kim. High Reynolds number flow simulations using the localized dynamic subgrid-scale model. 34th AIAA Aerospace Sciences Meeting and Exhibit, AIAA-1996-425, 1996.

[47] C. Fureby. On subgrid scale modeling in large eddy simulations of compressible fluid flow. *Physics of Fluids*, 8:1301–1311, 1996.

[48] A. Yoshizawa. Statistical theory for compressible shear flows with the application of subgrid modelling. *Physics of Fluids*, 29:2152–2163, 1986.

[49] C. Fureby, H. Tabor, H.G. Weller, and A.D. Gosman. A comparative study of subgrid scale models in homogeneous isotropic turbulence. *Physics of Fluids*, 9: 1416–1429, 1997.

[50] P.P. Sullivan, J.C. McWillams, and C. Moeng. A subgrid-scale model for large-eddy simulation of planetary boundary-layer flows. *Boundary-Layer Meteorology*, 71:247–276, 1994.

[51] E.R. Van Driest. On turbulent flow near a wall. *Journal of the Aeronautical Sciences*, 23:1007–1011, 1956.

[52] M. Germano, U. Piomelli, P. Moin, and W.H. Cabot. A dynamic subgrid scale eddy viscosity model. In Proceedings of the Summer Workshop, Stanford, CA., Center for Turbulence Research, 1990.

[53] U. Piomelli. Large-eddy simulation: Achievements and challenges. *Progress in Aerospace Sciences*, 35:335–362, 1999.

[54] D.K. Lilly. A proposed modification of the germano subgrid-scale closure method. *Physics of Fluids*, 4:633–635, 1992.

[55] H. Weller, G. Tabor, H. Jasak, and C. Fureby. A tensorial approach to CFD using object orientated techniques. *Computers in Physics*, 12:620–631, 1998.

[56] H. Jasak. *Error analysis and estimation for the finite volume method with application to fluid flows*. PhD thesis, Imperial College London, 1996.

[57] R.I. Issa. Solution of the implicitly discretized fluid flow equations by operator splitting. *Journal of Fluids and Structures*, 62:40–65, 1986.

[58] E. de Villiers. *The potential of large eddy simulation for the modelling of wall bounded flows.* PhD thesis, Imperial College London, 2006.

[59] H. Jasak and Ž Tuković. Automatic mesh motion for unstructured finite volume method. *Transactions of FAMENA*, 30:1–18, 2007.

[60] H. Al-Jamal, V.K. Rao, and C. Dalton. Vortex induced vibrations using large eddy simulation at a moderate Reynolds number. *Journal of Fluids and Structures*, 19: 73–92, 2004.

[61] A. Khalak and C.H.K. Williamson. Dynamics of a hydroelastic cylinder with very low mass and damping. *Journal of Fluids and Structures*, 10:455–472, 1996.

[62] C.J. Doolan. Large eddy simulation of the near wake of a circular cylinder at sub-critical Reynolds number. *Engineering Applications of Computational Fluid Mechanics*, 4:496–510, 2010.

[63] C. Norberg. An experimental investigation of the flow around a circular cylinder: Influence of aspect ratio. *Journal of Fluid Mechanics*, 258:287–316, 1994.

[64] U.O. Ünal and M Atlar. An experimental investigation into the effect of vortex generators on the near-wake flow of a circular cylinder. *Experiments in Fluids*, 48: 1059–1079, 2010.

[65] U.O. Ünal, M. Atlar, and Ö. Gören. Effect of turbulence modelling on the computation of the near-wake flow of a circular cylinder. *Ocean Engineering*, 37:387–399, 2010.

[66] U.O. Ünal and Ö. Gören. Effect of vortex generators on the flow around a circular cylinder: Computational investigation with two-equation turbulence models. *Engineering Applications of Computational Fluid Mechanics*, 5:99–116, 2011.

[67] R.N. Govardhan and C.H.K. Williamson. Modes of vortex formation and frequency response for a freely-vibrating cylinder. *Journal of Fluid Mechanics*, 420:85–130, 2000.

[68] H. Choi and P. Moin. Grid-point requirements for large eddy simulation: Chapman's estimates revisited. Annual Research Briefs, Center for Turbulence Research, 2011.

[69] S. Kim, P.A. Wilson, and Z. Chen. Effect of turbulence modelling on 3-D LES of transitional flow behind a circular cylinder. Ocean Engineering (Submitted), 2015.

[70] S. Kim, P.A. Wilson, and Z. Chen. Large-eddy simulation of the turbulent near wake behind a circular cylinder: Reynolds number effect. Applied Ocean Research (Submitted), 2015.

[71] S. Kim, P.A. Wilson, and Z. Chen. Numerial simulation of force and wake mode of an oscillating cylinder. *Journal of Fluids and Structures*, 44:216–225, 2014.

[72] S. Kim, P.A. Wilson, and Z. Chen. Controlled vibrations of a submerged cylinder. Journal of Fluids and Structures (Submitted), 2015.